Characterization of Antimicrobial and Bone Regenerative Activities of Porous Si-nHA Scaffolds Containing Vancomycin and rhBMP2

Suphannee Thanyaphoo

A Thesis Submitted in Partial Fulfillment of the Requirements for the Degree of

Doctor of Philosophy in Pharmaceutical Sciences

Prince of Songkla University

2015

Copyright of Prince of Songkla University

Thesis Title	Characterization of Antimicrobial and Bone Regenerative Activities of Porous Si-nHA Scaffolds Containing Vancomycin and rhBMP2
Author	Miss Suphannee Thanyaphoo
Major Program	Pharmaceutical Sciences

Major Advisor :

……...

(Assoc. Prof. Dr. Jasadee Kaewsrichan)

Co-advisor

……..…

(Assoc. Prof. Dr. Chua Kien Hui)

Examining Committee :

……..……..……..Chairperson

(Asst. Prof. Dr. Bhutorn Canyuk)

…..……..……

(Dr. Danai Tiwawech)

……

(Assoc. Prof. Dr. Jasadee Kaewsrichan)

…….…….....

(Assoc. Prof. Dr. Chua Kien Hui)

The Graduate School, Prince of Songkla University, has approved this thesis as partial fulfillment of the requirements for the Degree of Doctor of Philosophy in Pharmaceutical Sciences.

…….

(Assoc. Prof. Dr. Teerapol Srichana)

Dean of Graduate School

This is to certify that the work here submitted is the result of the candidate's own investigations. Due acknowledgement has been made of any assistance received.

…….. Signature

(Assoc. Prof. Dr. Jasadee Kaewsrichan)

Major Advisor

……...… Signature

(Miss Suphannee Thanyaphoo)

Candidate

ชื่อวิทยานิพนธ์ ศึกษาสมบัติการต้านจุลชีพและการสร้างกระดูกของโครงเลี้ยงเซลล์ชนิดมีรูพรุนที่เตรียมจากนาโนซิลิกอนไฮดรอกซิอะพาไทต์ซึ่งบรรจุยาแวนโคมัยซินและอาร์เอ็ชบีเอ็มพีทู

ผู้เขียน นางสาวสุพรรณี ธัญญะภู

สาขาวิชา เภสัชศาสตร์

ปีการศึกษา 2557

บทคัดย่อ

กระดูกติดเชื้อยังคงเป็นโรคที่มีข้อจำกัดทางการรักษา ยาที่ให้ทางปากหรือโดยการฉีดไม่สามารถเข้าถึงกระดูกที่เป็นโรคได้ เพราะกระดูกมีเส้นเลือดน้อยมาก หรือถูกทำลายไปเมื่อมีพยาธิสภาพเกิดขึ้น การพัฒนาวัสดุที่สามารถบรรจุยาปฏิชีวนะและโปรตีนที่กระตุ้นการสร้างกระดูกเพื่อฝังตรงบริเวณรอยโรคจึงเป็นแนวทางการรักษาที่น่าสนใจและเป็นไปได้

ไฮดรอกซิอะพาไทต์ที่มีธาตุซิลิกอนอยู่ในแลตทิสถูกเตรียมขึ้นโดยอาศัยปฏิกิริยาตกตะกอนทางเคมีแบบเปียก แคลเซียมไนเตรทและแอมโมเนียมไฮโดรเจนฟอสเฟตเป็นสารตั้งต้นสำหรับการเตรียมไฮดรอกซิอะพาไทต์ ซิลิกอนจากแคลเซียมซิลิเคตหลายๆอัตราส่วนโดยโมลต่อไฮดรอกซิอะพาไทต์ถูกเติมลงในปฏิกิริยาและทำให้เกิดการตกตะกอนร่วมอีกครั้ง เมื่อควบคุมสภาวะที่ใช้สังเคราะห์อย่างเคร่งครัดพบว่าวัสดุที่ได้มีขนาดอนุภาคระดับนาโนเมตร จากการศึกษาด้วยเทคนิค XRD, XRF และ FTIR พบการแทนที่ของซิลิกอนในแลตทิสของไฮดรอกซิอะพาไทต์ วัสดุมีสมบัติทางชีวภาพที่ดีซึ่งสัมพันธ์กับองค์ประกอบทางเคมีของพื้นผิววัสดุ โปรตีนสามารถดูดซับบนพื้นผิววัสดุได้ดี จึงเหนี่ยวนำให้เซลล์สร้างกระดูกยึดเกาะ เพิ่มจำนวนและเปลี่ยนแปลงเพื่อสะสมแร่ธาตุได้ดี การสร้างกระดูกใหม่จึงเกิดขึ้นได้ดีตามไปด้วย การแทนที่แลตทิสบางส่วนด้วยซิลิกอนทำให้เกิดความบกพร่องทางโครงสร้างของไฮดรอกซิอะพาไทต์ วัสดุชนิดใหม่นี้จึงละลายน้ำได้มากขึ้น

เตรียมโครงสร้างสามมิติให้ได้รูปทรงตามที่ต้องการ โดยผสมวัสดุดังกล่าวกับสารละลายไคโตซาน (ความเข้มข้น 1.5% ใน 3% กรดอะซิติก) จนได้ของผสมลักษณะข้นเหนียว บรรจุลงแม่พิมพ์และทิ้งให้แห้ง แช่ทั้งแม่พิมพ์ลงในสารละลายไตรโซเดียมพอลิฟอสเฟต (ความเข้มข้น 1% ในน้ำ) เป็นเวลา 1 คืนเพื่อให้ร่างแหของไคโตซานเชื่อมโยงกัน ล้างไตรโซเดียมพอลิฟอสเฟตออกให้หมด และทำให้แห้งด้วยเทคนิคการทำระเหิดแห้ง ผลจาก SEM พบรูพรุนขนาดเล็ก (< 100 นาโนเมตร) และขนาดใหญ่ (> 100 นาโนเมตร) กระจายอยู่ทั่วโครงสร้างสามมิติ รู

พรุนมีการเชื่อมต่อกัน โครงสร้างที่ได้มีประสิทธิภาพการบรรจุยาแวนโคมัยซินสูงกว่า 90% และปลดปล่อยยาได้ประมาณ 75-80% ในรูปแบบออกฤทธิ์เนิ่นนานกว่า 12 วัน ยาแวนโคมัยซินที่ปลดปล่อยจากโครงสร้างสามมิติมีความเข้มข้นสูงกว่าความเข้มข้นที่สามารถฆ่าเชื้อสตาฟิโลค็อกคัสถึง 20 เท่า จึงสามารถฆ่าเชื้อที่เป็นไบโอฟิล์มได้

อาร์เอ็ชบีเอ็มพีทูถูกตรึงไว้กับเฮพารินที่อยู่บนผิวโครงสร้างสามมิติโดยพันธะไอออนิกโดยที่เฮพารินถูกเชื่อมโยงเข้ากับไคโตซานก่อนด้วยปฏิกิริยาคาร์โบไดอิไมด์ (carbodiimide) เฮพารินที่ถูกตรึงไว้จะไม่ถูกชะออกเป็นเวลาอย่างน้อย 4 สัปดาห์ เมื่อฝังโครงสร้างสามมิติดังกล่าวลงใต้ผิวหนังส่วนหลังของหนูพบว่ามีกระดูกใหม่เกิดขึ้นภายใน 4 สัปดาห์ วิธีการตรึงอาร์เอ็ชบีเอ็มพีทูที่พัฒนาขึ้นใหม่นี้จึงมีประสิทธิภาพดีพอที่จะนำมาเตรียมโครงเลี้ยงเซลล์เพื่อศึกษาต่อไป

สามารถสร้างสัตว์ทดลองต้นแบบที่มีกระดูกติดเชื้อ (osteomyelitis) ได้โดยฉีดเชื้อสตาฟิโลค็อกคัสออเรียสเข้าไปในช่องว่างของกระดูกขาท่อนยาวของหนูผ่านทางหัวเข่า จากภาพถ่ายเอ็กซ์เรย์พบว่ามีการทำลายกระดูกเกิดขึ้นลักษณะเช่นเดียวกับโรคกระดูกติดเชื้อ และตรวจพบเชื้อแบคทีเรียที่ฉีดในเนื้อเยื่อบริเวณหัวเข่า โครงเลี้ยงเซลล์เส้นผ่าศูนย์กลาง 5 มิลลิเมตร ยาว 10 มิลลิเมตร ถูกเตรียมขึ้น ครึ่งหนึ่งบรรจุยาแวนโคมัยซิน อีกครึ่งหนึ่งตรึงอาร์เอ็ชบีเอ็มพีทูไว้ กระดูกขาท่อนยาวของหนูที่ติดเชื้อ ยาว 10 มิลลิเมตร ถูกตัดออก และแทนที่ด้วยโครงเลี้ยงเซลล์ดังกล่าว การวิเคราะห์ทางเนื้อเยื่อหลังจากนั้น 8 สัปดาห์พบว่าโครงเลี้ยงเซลล์ที่บรรจุยาแวนโคมัยซินและอาร์เอ็ชบีเอ็มพีทูกระตุ้นให้เกิดการสร้างกระดูกใหม่ได้ดีกว่าโครงเลี้ยงเซลล์ที่บรรจุอาร์เอ็ชบีเอ็มพีทูอย่างเดียว ตรวจพบเชื้อแบคทีเรียชนิดเดียวกับที่ใช้ฉีดในเนื้อเยื่อรอบบริเวณที่ฝังโครงเลี้ยงเซลล์ ปริมาณเชื้อที่ตรวจพบเท่ากับ 10 และ 10^4 CFU ต่อกรัมเนื้อเยื่อสำหรับโครงเลี้ยงเซลล์ที่มีและไม่มียาแวนโคมัยซินตามลำดับ ชี้ให้เห็นว่าการสร้างกระดูกใหม่จะเกิดขึ้นเมื่อเชื้อแบคทีเรียที่เป็นสาเหตุของโรคถูกกำจัดออกไปแล้ว ดังนั้น วัสดุที่สังเคราะห์ได้ในครั้งนี้จึงสามารถนำมาใช้เตรียมโครงเลี้ยงเซลล์เพื่อใช้เป็นระบบการนำส่งยาสำหรับรักษาโรคกระดูกอื่นๆได้ในอนาคตอันใกล้

Thesis Title Characterization of Antimicrobial and Bone Regenerative Activities of Porous Si-nHA Scaffolds Containing Vancomycin and rhBMP2

Author Miss Suphannee Thanyaphoo

Major Program Pharmaceutical Sciences

Academic Year 2014

ABSTRACT

Osteomyelitis (OM) remains an intractable problem for the present therapy. Drugs administered orally or systemically could not reach the site of infected bone, due to the scantiness of blood vessels and their destruction when having the pathology. The development of bone grafts containing antibiotics and osteogenic growth factors for local implantation are interesting and are potential for the treatment.

The particles of Si-substituted hydroxyapatite (Si-nHA) were prepared by the wet chemical precipitation reaction. Calcium nitrate ($Ca(NO_3)_2$) and ammonium hydrogen phosphate ($(NH_4)_2HPO_4$) were used as the reactants for preparing HA. Various mole ratios to HA of $CaSiO_3$ (the source of Si) were separately added to the reaction. When the synthesis conditions were strictly controlled, the particulate material of nano-sized ranges was obtained. According to the results of XRD, XRF and FTIR, the replacement of Si in HA lattices was detected. The material showed good bioactivity, associating with surface chemical compositions of the material. Protein adsorption ability was sufficient to induce the adhesion of osteoblast cells, followed by proliferation, differentiation, and mineralization, leading to the formation of new bone. The partial substitution of Si in lattices of the parent caused defective structure, providing the material which was more water soluble.

The 3D structure of scaffolds with desired shapes was prepared by mixing the materials with chitosan solution (1.5% w/v in 3% acetic acid) until obtaining smooth paste. The paste was packed into a mold and left air-dry. The packed mold was soaked in TPP solution (1% w/v in water) overnight in order that cross-linking of chitosan chains was taken place. Excess TPP was removed by washing with distilled water. The construct was subjected to freeze drying. Based on SEM results, the opened and interconnected pores of nano- (<100 nm) and micro- (>

100 nm) sizes were distributed over the structure. The loading efficiency for vancomycin (VCM) was more than 90%. The drug release was about 75-80%, displaying the sustained release pattern over a 12-day period. The released concentration was 20 times higher than the concentration able to kill *Staphylococcus aureus* growing as biofilms.

The immobilization of rhBMP2 on the 3D structure was achieved by ionically bonding with heparin, which was previously conjugated with chitosan by using carbodiimide reaction. The bound heparin did not leach from the so-called heparinized scaffold by at least 4 weeks of storage. Ectopic bone formation was observed within 4 weeks of implantation in rats. The recently developed method for heparin immobilization was efficient for preparing scaffolds to evaluate in further studies.

Rat model with osteomyelitis (OM) was successfully prepared by injecting *S. aureus* in epiphysis of tibial bone, followed by drilling the needle through cortical and spongy bone until accessing the cavity. X-ray photographs showed the bone destruction, displaying as OM after 4 weeks of the inoculation. The induced bacteria were detected in tissues surrounding the affected bone. A scaffold with 5 mm in diameter and 10 mm in length was prepared. A half of it was loaded with VCM, while another half was loaded with rhBMP2. The infected bone with 10 mm in length was removed and replaced by the prepared scaffolds. After 8 weeks of implantation, new bone formation was significantly observed for the scaffolds containing VCM and rhBMP2, compared to those containing rhBMP2 alone, as evaluated by histological analysis. The causing bacteria of 10 and 10^4 CFU/g tissue were examined for the implants with and without VCM, respectively. The result suggested that bone regeneration could occur only when the causing bacteria were nearly eliminated. In consequence, the material synthesized in this study can be used in preparing drug delivery system, focusing on curing of bone diseases in the near future.

CONTENTS

		Page
ABSTRACT (in Thai)		v
ABSTRACT (in English)		vii
ACKNOWLEDGEMENT		ix
CONTENTS		x
LIST OF TABLES		xvi
LIST OF FIGURES		xvii
LIST OF ABBREVIATIONS AND SYMBOLS		xxi
CHAPTER 1: INTRODUCTION		**1**
1.1 Background and general introduction		**1**
1.1.1	Bone structures	3
1.1.2	Cells of bone tissue	5
1.1.2.1	Osteoprogenitor cell	6
1.1.2.2	Osteoblast	6
1.1.2.3	Osteocyte	7
1.1.2.4	Bone-lining cells	7
1.1.2.5	Osteoclast	8
1.1.3	Composition of bone	8
1.1.4	Bone healing and repair	12
1.1.4.1	Intramembranous ossification	12
1.1.4.2	Endochondral Ossification	14
1.1.5	Morphology of fracture region in healing process	15
1.1.5.1	Hematoma and inflammatory phase	15
1.1.5.2	Soft callus formation	15
1.1.5.3	Hard callus formation	16
1.1.5.4	Remodeling	16

CONTENTS (continued)

1.1.6 The requirement of bone healing 18

1.1.6.1 Osteogenesis 18

1.1.6.2 Osteoconduction 19

1.1.6.3 Osteoinduction 19

1.1.6.4 Osteointegration 19

1.1.7 Osteomyelitis (OM) 19

1.1.7.1 *Staphylococcus aureus* 21

1.1.7.2 Methicillin-resistant *S. aureus* (MRSA) 22

1.1.7.3 Pathogenesis 22

1.1.7.4 Treatment of OM by antibiotics 25

1.1.7.5 Vancomycin 26

1.1.8 Biomaterials used as drug delivery system (DDS) in OM 27

1.1.8.1 Non-biodegradable materials 28

1.1.8.2 Biodegradable materials 28

1.1.9 Scaffolds design and processing 30

1.1.10 Nanoscale biomaterials as scaffolds 31

1.1.11 Calcium phosphate-based materials 31

1.1.11.1 Hydroxyapatite 31

1.1.12 Chitosan 33

1.1.13 Growth factor in bone tissue engineering 36

1.1.13.1 Bone morphogenetic proteins (BMPs) 37

1.1.13.1.1 Bone morphogenetic protein 2 (BMP2) 37

1.1.14 Heparin 38

1.1.15 Carbodiimide reaction 40

1.2 Rationale of the study 42

1.3 Objectives 44

1.4 Research expectation 45

CONTENTS (continued)

CHAPTER 2: MATERIALS AND METHODS **46**

2.1 Materials **48**

2.2 Part I: Preparation of Si–nHA powders **55**

2.2.1 Synthesis of Si–nHA powders 55

2.2.2 Induction of forming apatite layer on Si–nHA powders 58

2.3 Part II: Physical characterizations **59**

2.3.1 X-ray diffraction (XRD) 59

2.3.2 X-ray fluorescence (XRF) 59

2.3.3 Fourier transform infrared spectroscopy (FTIR) 59

2.3.4 Scanning electron microscopy (SEM) 60

2.3.5 Thermo-gravimetric analysis (TGA) 60

2.3.6 Zeta potential (ζ) 60

2.4 Part III: Preparation of drug-free scaffolds **61**

2.4.1 Fabrication of porous scaffolds 61

2.4.2 Evaluation of drug-free scaffolds *in vitro* 61

2.4.2.1 The release of Ca^{2+} ions 61

2.4.2.2 The release of PO_4^{3-} ions 62

2.4.2.3 *In vitro* biodegradation test 62

2.4.2.4 Protein adsorption on drug-free scaffolds 63

2.5 Part IV: Loading of VCM and rhBMP2 **63**

2.5.1 Vancomycin-containing Si–nHA scaffolds 63

2.5.1.1 Drug loading 63

2.5.1.2 The Entrapment Efficiency (%EE) 64

2.5.1.3 *In vitro* release 64

2.5.1.4 Antimicrobial activity of VCM-loaded scaffolds 64

2.5.1.5 Cytotoxicity of VCM-loaded scaffolds 66

CONTENTS (continued)

2.5.2 Loading of rhBMP2 into scaffolds 67

2.5.2.1 Preparation of heparinized scaffolds 67

2.5.2.2 Characterization of the heparinized scaffolds 67

2.5.2.2.1 Toluidine blue staining 67

2.5.2.2.2 Stability and blood compatibility 68

2.5.2.3 Loading of rhBMP2 onto the heparinized scaffolds 68

2.5.2.4 *In vivo* evaluation of rhBMP2 loaded scaffolds 69

2.5.2.4.1 Animals and surgical procedure 69

2.6 Part V: *In vivo* evaluation of VCM/rhBMP2 containing scaffolds 70

2.6.1 Preparation of VCM/rhBMP2 containing scaffolds 70

2.6.2 Osteomyelitis induction in rats 70

2.6.2.1 Preparation of bacterial cells 70

2.6.2.2 Bacterial inoculation in rats 71

2.6.3 Implantation of VCM/rhBMP2 loading scaffolds in osteomyelitis rats 71

2.6.4 Histological analysis 72

2.7 Statistical Analysis 73

CHAPTER 3: RESULTS 74

3.1 Part I: Preparation of Si–nHA powders 74

3.1.1 Synthesis of Si–nHA powders 74

3.1.2 Apatite formation on the surfaces of Si–nHA particles 75

3.2 Part II: Physical characterizations 76

3.2.1 X-ray diffraction analysis (XRD) 76

3.2.2 X-ray fluorescence spectroscopy (XRF) 78

3.2.3 Fourier transform infrared spectroscopy (FTIR) 79

3.2.4 Scanning electron microscopy (SEM) 84

3.2.5 Thermo-gravimetric analysis (TGA) 86

3.2.6 Zeta potential (ζ) 88

CONTENTS (continued)

3.3 Part III: Preparation of drug-free scaffolds **90**

3.3.1 Fabrication of scaffolds 90

3.3.2 Evaluation of drug-free scaffolds *in vitro* 91

3.3.2.1 The release of Ca^{2+} and PO_4^{3-} ions 91

3.3.2.2 Scaffold degradation 92

3.3.2.3 Protein adsorption on the fabricated scaffolds 93

3.4 Part IV: Loading of VCM and rhBMP2 **95**

3.4.1 Loading of VCM 95

3.4.1.1 *In vitro* VCM release 96

3.4.1.2 Antimicrobial activity of VCM-loaded scaffolds 98

3.4.1.3 Cytotoxicity of VCM-loaded Scaffolds 98

3.4.2 Loading of rhBMP2 100

3.4.2.1 Stability of the bound heparin: characterized by toluidine blue staining 100

3.4.2.1.1 Stability and blood compatibility 102

3.4.2.2 Loading of rhBMP2 onto the heparinized scaffolds 105

3.4.2.3 *In vivo* evaluation of rhBMP2 loaded scaffolds 105

3.5 Part V: *In vivo* evaluation of VCM/rhBMP2 loading scaffolds **107**

3.5.1 Implant design and fabrication 107

3.5.2 Osteomyelitis induction in rats 107

3.5.3 Implantation 108

3.5.4 Histological analysis 110

CHAPTER 4: DISCUSSIONS **112**

4.1. Part I: Preparation of Si–nHA powders **113**

4.2. Part II: Physical characterizations **113**

4.3. Part III: Fabrication and characterization of drug-free scaffolds **118**

4.4. Part IV: Drug loading and loading efficiency **121**

4.5. Part V: Evaluation of VCM/rhBMP2-loaded scaffolds *in vivo* **123**

CONTENTS (continued)

CHAPTER 5: CONCLUSION **125**

REFERENCES 128

APPENDIX A PREPARATION OF SOLUTIONS AND BUFFERS 151

APPENDIX B STATISTICAL ANALYSIS 159

VITAE 189

LIST OF TABLES

		Page
Table 1.1	The difference between compact and cancellous bones	4
Table 1.2	Components of bone	9
Table 1.3	Biological properties of chitosan	34
Table 2.1	List of chemicals and reagents, including the corresponding purchased company	48
Table 2.2	Equipments and the corresponding models and owners	52
Table 2.3	The groups of synthesized Si-nHA powders and the designed mole ratios of $CaSiO_3$ to HA	55
Table 2.4	Experimental design for the evolution of bone formation efficiency by subcutaneous implantation of scaffolds in rats	69
Table 2.5	Design of the experiment for studying in osteomyelitis model	72
Table 3.1	XRF results in different bioactive material including the theoretical and measured ratios of Ca/P and (Ca+P)/Si atomic	78
Table 3.2	Characteristic bands of FTIR spectra for Si-nHA powders	80
Table 3.3	Thermal behavior of the specified Si-nHA powders derived from TGA curves	87
Table 3.4	The zeta potenial ζ (mV) of the as-synthesized materials and those of after immersed in PBS for 14 day at pH 6, 7 and 8	88
Table 3.5	Entrapment Efficiency (%EE) of VCM in scaffolds containing different types of the ceramic materials	95
Table 3.6	Clotting appearances of blood by incubating with the rinsed solutions of the heparinized scaffolds	103

LIST OF FIGURES

		Page
Figure 1.1	Types of bones based on their shapes	2
Figure 1.2	The architectural form of long bone	3
Figure 1.3	Different cell types associated with bone	5
Figure 1.4	The hierarchical structure of bone	11
Figure 1.5	Processes of intramembranous ossification	13
Figure 1.6	Processes of endochondral ossification	14
Figure 1.7	Schematics of the healing for fractured bone	17
Figure 1.8	SEM image of *S. aureus* under a high magnification of 10,000x	21
Figure 1.9	Steps in the progressive development to OM of bone	23
Figure 1.10	VCM hydrochloride	26
Figure 1.11	Types of DDS for bone tissue engineering	27
Figure 1.12	Steps in bone tissue engineering using biodegradable 3D scaffolds	29
Figure 1.13	Chemical structure of chitosan	35
Figure 1.14	Chemical structure of TPP	35
Figure 1.15	Schematic presentation of TPP-chitosan crosslinking	36
Figure 1.16	Structure of heparin	38
Figure 1.17	Interaction between heparin negatively charged sulfate groups and the proteins' positively amino acid residues	39
Figure 1.18	Chemical structure of EDC	40
Figure 1.19	Chemical structure of NHS	40
Figure 1.20	The carbodiimide reaction using EDC/NHS	41
Figure 1.21	Concept of fabrication of double-layered scaffold for treating OM	43

LIST OF FIGURES (continued)

		Page
Figure 2.1	Five parts of the study, including synthesis of silicon (Si)-substituted nano-hydroxyapatite (Si-nHA) powders (I), the physical characterizations of the synthesized products (II), fabrication of scaffolds containing the Si-nHA particles (III), drug loading and loading efficiency determination (IV), and evaluation of drug-loaded scaffolds *in vivo* (V)	47
Figure 2.2	The procedures for preparing silicon-substituted nano-hydroxyapatite (Si-nHA) powders by the wet chemical precipitated method	57
Figure 2.3	Preparation of two-fold dilutions for test samples	65
Figure 2.4	Schematic diagram of 3D-structure and dimension for three types of the scaffolds containing VCM, rhBMP2, or VCM plus rhBMP2	70
Figure 3.1	SEM images of silicon substituted hydroxyapatite (Si-nHA) pariticles prepared by the wet chemical precipitation reaction	74
Figure 3.2	SEM images of apatite layer on the Si-nHA surfaces	75
Figure 3.3	XRD patterns of Si-nHA powders after the synthesis (0 day) and of the 14-day soaking in PBS	77
Figure 3.4	FTIR spectra of Si-nHA powders before (0 day) and after soaking in PBS for 14 days	81
Figure 3.5	FTIR spectra of 0.3 and 0.4Si–contHA powders before (0 day) and after immersed in PBS for 14 days	82
Figure 3.6	FTIR spectra of 0.3 and 0.4Si–synHA powders before (0 day) and after immersed in PBS for 14 days	83
Figure 3.7	SEM images of the Si-nHA powders	85
Figure 3.8	TGA curves for 0.3Si-contHA, 0.3Si-synHA, 0.4Si-contHA, and 0.4Si-synHA in the temperature range between 25 and 1350 °C	87
Figure 3.9	The ζ (mV) of the as-synthesized particles and those of after immersed in PBS for 14 day at pH 6, 7 and 8	89

LIST OF FIGURES (continued)

		Page
Figure 3.10	SEM image indicating porous structure of the scaffolds	90
Figure 3.11	The concentrations of Ca^{2+} and PO_4^{3-} released from four different types of the scaffolds within 30 days in PBS at 37 ºC	91
Figure 3.12	The percentage weight loss of the scaffolds prepared from 0.3Si-contHA, 0.3Si-synHA, 0.3Si-contHA, 0.3Si-synHA materials after immersed in PBS at 37 °C for 30 days	92
Figure 3.13	SEM micrographs of proteins adsorbed on scaffold surfaces after soaking in serum supplemented DMEM for 1 and 3 days	94
Figure 3.14	(a) The apparent amounts of VCM released from scaffolds and (b) the plot of the percentage drug release as a function of $time^{1/2}$ (h)	97
Figure 3.15	The viability of osteoblast-like cells cultured with different concentrations of the solutions extracted from VCM-loaded scaffolds consisting of 0.3Si–contHA, 0.3Si–synHA 0.4Si–contHA, or 0.4Si–synHA	99
Figure 3.16	The photographs of toluidine blue staining for scaffolds with different degrees of heparin immobilization	101
Figure 3.17	SEM images of platelets adhered on the scaffold consisting of 0.4Si-contHA or 0.4Si-synHA, previously heparinized by using 0, 0.5, 1.0, and 2.0 % w/v heparin, respectively	104
Figure 3.18	The hematoxylin/eosin (HE) and alizarin red S (ARS) staining of scaffold sections after subcutaneously implanted in rats for 4 weeks	106
Figure 3.19	The representative radiographs of (a), bone destruction at proximal epi-/metaphysic region of tibia (}); (b), the occurring bone space immediately after a 10-mm segment was removed; (c), the residual implants of V-group after 8 weeks post-implantation; (d and e), bridging between the implants and the remaining original bones of B- and VB-group, respectively, after 8 weeks post-implantation.	109

LIST OF FIGURES (continued)

		Page
Figure 3.20	Sections along the bone defects for the specimens of V-, B-, and VB-groups after 8 weeks post-implantation	111
Figure 4.1	Schematic drawing in structural lattices of pure nHA and of Si-nHA	114
Figure 4.2	Schematic drawing of mechanism of apatite formation on Si-nHA	117
Figure 4.3	Schematic representation for the fabrication of drug-free scaffolds	118

CHAPTER 1

INTRODUCTION

1.1 Background and general introduction

Bones differ from other tissues in that they have a unique capacity for regenerative growth, healing and remodeling themselves throughout the lifetime of an individual without forming a fibrous scar. However, these processes are often impaired especially for critical-sized defects. Bone tissue engineering (BTE) has been a potential alternative strategy to heal severe bone injuries, due to the limited supply of autographs. BTE is based on bone structure, bone mechanism, and tissue formation as it aims to induce new functional bone tissues. In other words, to successfully regenerate or repair bone, knowledge of bone biology and development is quite essential.

Bones in the human body can be divided into six main types, depending on their shapes, such as flat, sutural, long, irregular, sesamoid and short bones (Figure 1.1).

Bone is one of the most important organs of the body. It plays some roles that crucial for life, such as

(1) To shape bone structure giving a frame to shape the body.

(2) To support the body, keep your internal organs in their proper place, as well as give a framework of attachment for skeletal muscles and other tissues.

(3) To protect internal organs from damage or injury such as cranial bones, which protect the brain.

(4) To be involved in movement: the skeletal bones are held together by ligaments which enable body movements.

(5) To produce blood cells: the spongy tissue inside long bones is responsible for the production of blood cells.

(6) To be a storage bank: the skeletal bones function as storages for lipids and minerals.

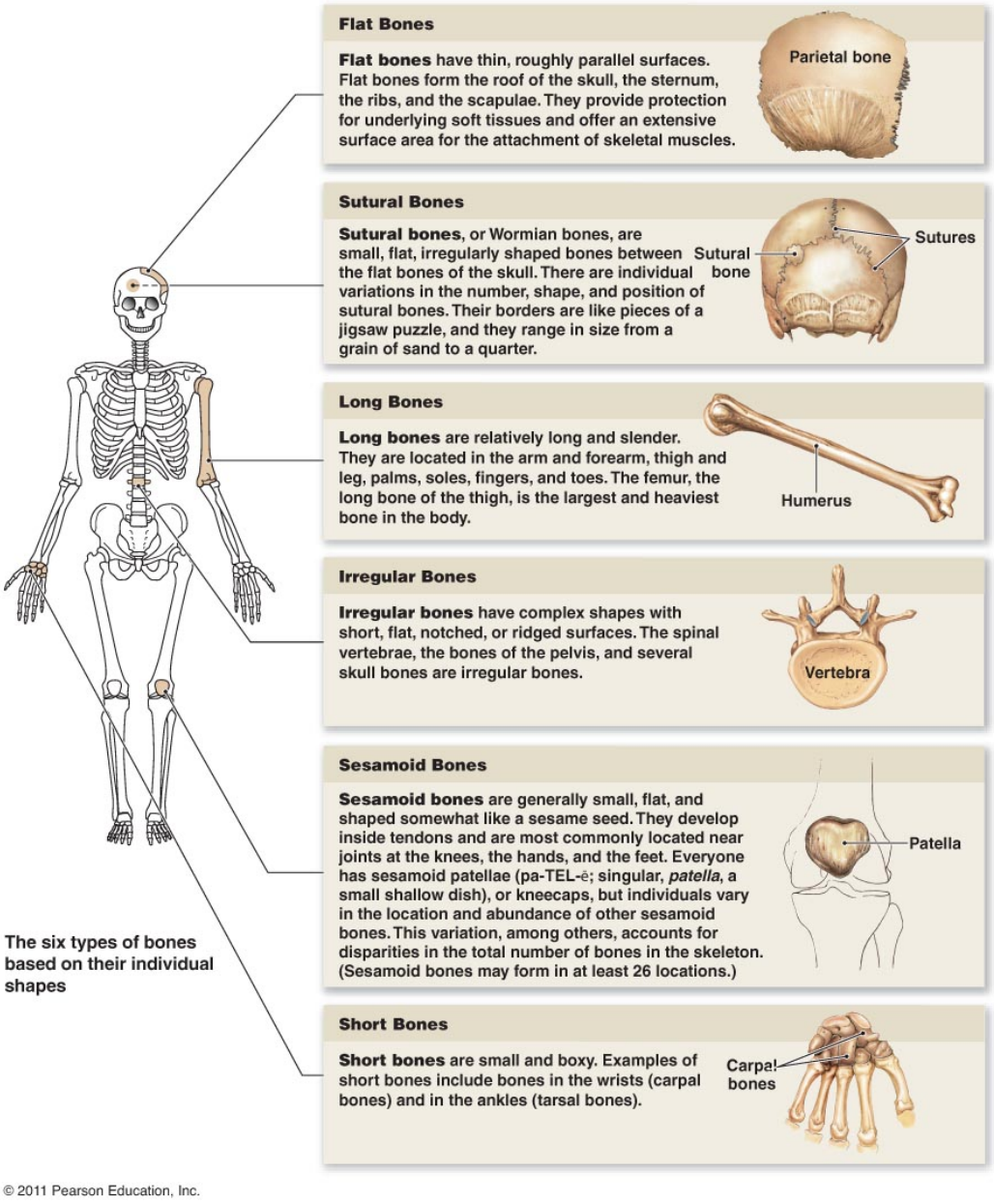

Figure 1.1 Types of bones based on their shapes [1]

1.1.1 Bone structures

Each bone in the adult skeleton has been classified as cancellous (also called trabecular or spongy) bone, and compact or cortical bone. Around 80% are compact bone. It usually presents the thick outer layer. The remaining 20% of total skeleton is cancellous bone. It is located in the core at the ends of bones [2, 3]. The compact bone is mostly solid, whereas the cancellous bone is full of opened sections called pores. The inside of the bone is filled with a soft tissue called bone marrow (Figure 1.2). The differences in structure between compact and cancellous bones are described in Table 1.1.

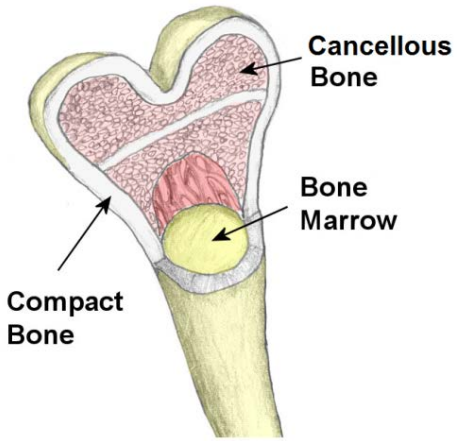

Figure 1.2 The architectural form of long bone [4]

Table 1.1 The difference between compact and cancellous bones [5]

Type of bone	Compact bone	Cancellous bone
Structure	It has elongated cylindrical form that forms the tough, provides a framework and strongly supports to the human body	It has a sponge-like form, similar to honeycomb of branching bar, plates and rod of various sizes
Weight	80%	20 %
Porosity	10%	50-90%
Bone Mass	High	Low
Calcium Content	Primary component and it is stored in the body lies	Very small
Shape	Cylindrical	Cuboidal
Location	Long bones (legs and arms etc.)	Short bones (ankles and wrists etc.) and the end of long bones

Cancellous and compact bones consist of several types of bone cells that are embedded in the bone matrix.

1.1.2 Cells of bone tissue

Five types of cells are resided in bone tissues; including osteoprogenitor cells, osteoblast, osteoclast, osteocyte, and bone-lining cells. These cells are responsible for bone growth, shaping, maintenance, elaboration and resorption. Each cell type has a unique function and found in different location in bones (Figure 1.3).

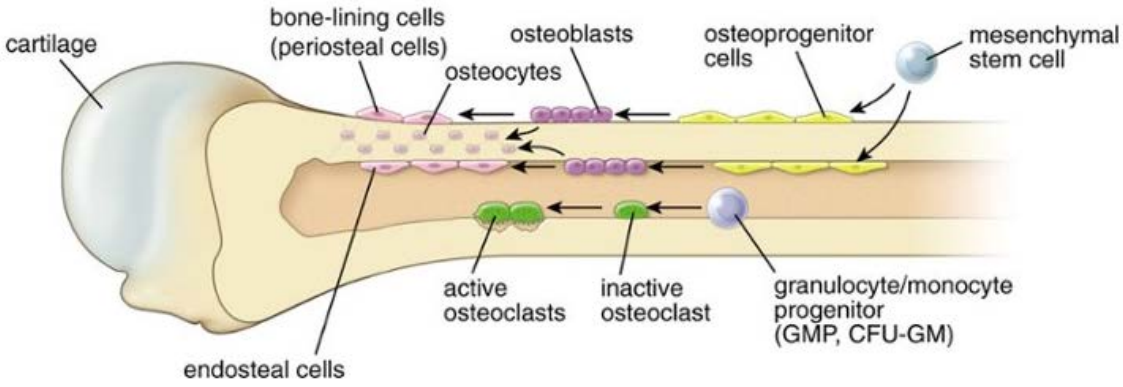

Figure 1.3 Different cell types associated with bone [6]

With the exception of the osteoclast, each of these cells may be regarded as a differentiated form of the same basic cell type. Each undergoes transformation from a less mature form to a more mature form in relation to functional activity (growth of bone). In contrast, the osteoclast originates from a different cell line and is responsible for bone resorption, an activity associated with bone remodeling. Further details in the characteristics and functions of these cells are described as follow.

1.1.2.1 Osteoprogenitor cell

The osteoprogenitor cell is derived from mesenchymal stem cells in the bone marrow. It is a resting cell that can differentiate into an osteoblast by mitosis and secrete bone matrix. Osteoprogenitor cells are found on the external and internal surfaces of bones and may also reside in the microvasculature supplying bone. Morphologically, they comprise the periosteal cells that form the innermost layer of the periosteum and the endosteal cells that line the marrow cavities, the osteonal (Haversian) canals, and the perforating (Volkmann's) canals. In growing bones, osteoprogenitor cells appear as flattened or squamous cells with lightly staining, elongate, or ovoid nuclei and inconspicuous acidophilic or slightly basophilic cytoplasm.

1.1.2.2 Osteoblast

The osteoblast is the differentiated bone-forming cell that secretes bone matrix. The osteoblast is a mononucleate bone-forming cell which derived from mesenchymal stem cell. The osteoblast is a versatile secretory cell that retains the ability to divide. It is a connective tissue cell found at the surface of bone. It is responsible for bone matrix synthesis. It secretes both type I collagen (which constitutes 90% of the protein in bone) and bone matrix proteins, which constitute the initial unmineralized bone, or osteoid. The bone matrix proteins produced by the osteoblast include calcium-binding proteins such as osteocalcin and osteonectin; multiadhesive glycoproteins such as bone sialoproteins I and II, osteopontin, and thrombospondin, various proteoglycans and their aggregates, and alkaline phosphatase (ALP). Circulating levels of ALP and osteocalcin are used clinically as markers of osteoblast activity. The osteoblast is also responsible for the calcification of bone matrix. When the area surrounding osteoblasts is calcified, they get trapped and deposit with in the calcified matrix that are able to mineralize. Subsequently, they can be stimulated to proliferate and differentiate their structure and function changing into osteocytes, the most common and mature type of bone cells, whose main functions are the regulation of the blood-calcium level and the functional adaptation of bones [7]. They are found in growing portions of bone, including periosteum which is the external surface of most bones. Mature osteoblasts are cuboidal cells responsible for the production of

matrix constituents (collagen and ground substance) and subsequent mineralization. The calcification process appears to be initiated by the osteoblast through the secretion into the matrix of small, 50- to 250-nm, membrane-limited matrix vesicles. The vesicles are rich in ALP and are actively secreted only during the period in which the cell produces the bone matrix.

1.1.2.3 Osteocyte

The osteocyte is the mature bone cell enclosed by bone matrix secreted by an osteoblast. It is derived from a proportion of osteoblast which is embedded in lacunae to build up the newly osteon. The osteons are placed in parallel to the long dimension of the bone [7-9]. Osteocytes probably function as mechanosensor and chemosensor regulating the response of bone maintenance and remodeling [10-12]. When completely surrounded by osteoid or bone matrix, the osteoblast is referred to as an osteocyte. Such activities help to maintain calcium homeostasis. The death of osteocytes through trauma (e.g., a fracture), cell senescence, or apoptosis results in resorption of the bone matrix by osteoclast activity, followed by repair or remodeling of the bone tissue by osteoblast activity.

1.1.2.4 Bone-lining cells

Bone-lining cells are derived from osteoblasts and cover bone that is not remodeling. In sites where remodeling does not occur, the bone surface is covered by a layer of flat cells with attenuated cytoplasm and a paucity of organelles beyond the perinuclear region. These cells are designated simply as bone-lining cells. Bone-lining cells on external bone surfaces are called periosteal cells, and those lining internal bone surfaces are often called endosteal cells. Gap junctions are presented where the bone-lining cells contact one another. The cells are thought to function in the maintenance, support of the osteocytes embedded in the underlying bone matrix, and regulate the movement of calcium and phosphate into and out of the bone. In these respects, bone-lining cells are somewhat comparable to osteocytes.

1.1.2.5 Osteoclast

Osteoclasts are derived from the fusion of mononuclear hemopoietic progenitor cells, namely, granulocyte/ macrophage progenitor cells (GMP, CFU-GM) that give rise to granulocyte and monocyte cell lineages. In contrast to what dose one think, osteoclasts are not related to osteoblasts. Osteoclasts are multinucleated and responsible for bone resorption (or resorbing matrix). They are found in bone surfaces and at sites of old, injured, or unneeded bone. They are able to degrade the mineralized bone matrix. By attachment to the bone surface, they generate a local acidic microenvironment for the dissolution of bone mineral phase. In addition, they secrete proteolytic enzyme into the resorption lacunae for the degradation of extracellular matrix. Afterward, osteoblast will fill with new bone matrix [13]. The ongoing balance between osteoblasts (which generate new bone) and osteoclasts (which break down bone) is responsible for the constant reshaping of bone.

1.1.3 Composition of bone

Bone is a specialized connective tissue which is a multi-phase composite material. The composition of bone differs with age, skeletal location, nutritional status, state of maturation and turnover, diet, and health. It generally consists of 60-70% inorganic mineral phrase, 10-20% organic matrix and cells, 9-20% water, and small quantities of other organic materials, such as polysaccharides proteins and lipids [14, 15]. The organic phase composes of collagen type I (90%) and non-collagenous protein (10%). The inorganic (or mineral) phase mainly consists of tiny crystals of hydroxyapatite $Ca_{10}(PO_4)_6(OH)_2$, which accounts for the hardness and compression resistance of bone. These crystals enclose the collagen fibrils to form a composite material. Water plays an important role in the bio-mineralization process and serves as a plasticizer, enhancing the toughness of bone. All of the components are arranged into a complex hierarchical structure, which makes bone with the required properties of stiffness, flexibility and strength [2, 3, 16, 17]. For better understanding, the components of bone are summarized in Table 1.2

Table 1.2 Components of bone [18]

Constituent	Type	Function and properties
Inorganic mineral phrase		
Hydroxyapatite		Provides compressive strength
Organic matrix		
Collagen	Type I	Provides framework for skeleton structure; matrix calcification, and the deposition of bone mineral
	Type III, V	Regulate collagen fibril diameter
	Type X	Found in hypertrophic cartilage
[a]SIBLING proteins	Osteopontin	Inhibits mineralization and remodeling
	Bone sialoprotein	Initiates mineralization
Serum proteins in bone matrix albumin		Decreases hydroxyapatite crystal growth
Glycoprotein	Osteonectin	Regulates collagen fibril diameter
	Alkaline phosphatase	Hydrolyzes mineral deposition inhibitors
	Proteins with [b]RGD	
	- Fibonectin	Binds to cells
	- Fibrillin	Regulates elastic fiber formation
	- Osteocalcin	Regulates osteoclasts; inhibits mineralization
	- Thrombospondin	Regulates angiogenesis and mineral deposition
	- Tetranectin	Deposits minerals
	- Vitronectin	Attaches cells

[a]SIBLING proteins: Small Integrin-Binding Ligand, N-glycosylated proteins

[b]RGD: Proteins that contain the Arg-Gly-Asp (RGD) attachment site

Table 1.2 (continued)

Constituent	Type	Function and properties
Proteoglycans	Aggrecan	Organizes matrix and retains calcium/phosphorus
	Biglycan	Binds collagen; binds TGF-β; genetic determinant of peak bone mass
	Decorin	Regulates collagen fibril diameter; binds TGF-β
	Hyaluronan	Defines space destined to become bone
	Versican	Defines space destined to become bone
Gla proteins	Matrix Gla protein	Inhibits calcification
	Osteocalcin	Regulates osteoclasts; inhibits mineralization
Lipid		Forms bone, metabolizes and mineralizes bone
Growth factor	Transforming Growth Factor-β(TGF-β)	Stimulates undifferentiated mesenchymal cell proliferation
	Insulin-like Growth Factor (IGF)	Promotes proliferation and differentiation of osteoprogenitor cells
	Bone Morphogenetic Proteins, (BMPs)	Promotes differentiation of mesenchymal cells into chondrocytes and osteoblasts Promotes differentiation of osteoprogenitors into osteoblasts, influences skeletal pattern formation

Additionally, bone tissues can be observed multi-level structure hierarchy (Figure 1.4). It is important to understand the structural relation between these levels in order to fulfill their biological and mechanical functions [19, 20].

At macro level, bone is divided into cancellous and compact bone, whereas at micro level, bone is built up by the basic building blocks of osteons embedded in the lamellae formed by collagen fibers, which are mineralized by hydroxyapatite crystals (Figure 1.4).

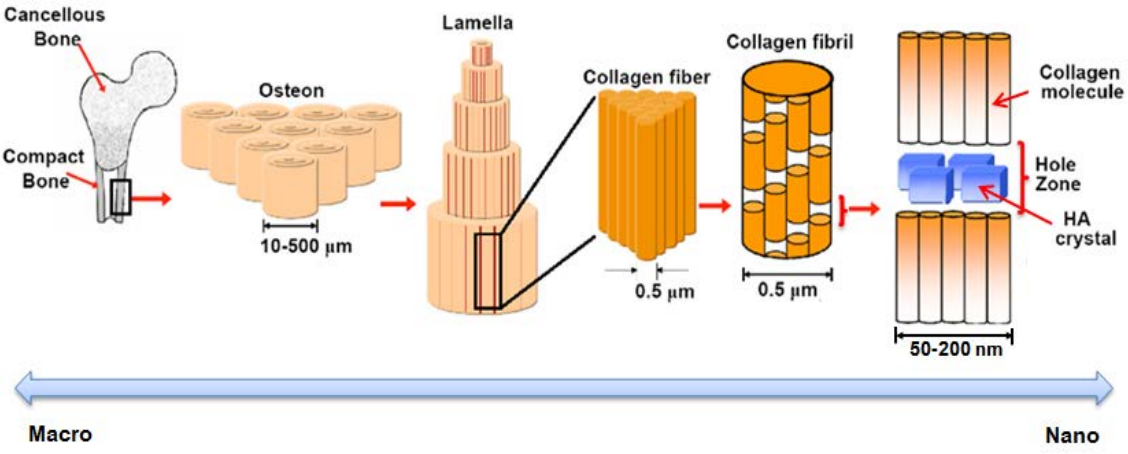

Figure 1.4 The hierarchical structure of bone [21]

Understanding bone processes such as bone formation, healing, repair, remodeling, and regeneration are the basis for creating therapeutic tools of bone tissue engineering.

1.1.4 Bone healing and repair

In general, the common ability of natural bone healing is intensely dependent on the size of defects. The healing process is the combination of intramembraneous and endochondral ossifications.

1.1.4.1 Intramembranous ossification

In intramembranous ossification, bones develop between sheets of fibrous connective tissue. Here, cells derived from connective tissue differentiate into osteoblasts located in ossification centers (Figure 1.5a). The osteoblasts begin to secrete the organic matrix of bone, called osteoid, within the fibrous tissue and the osteoid is mineralized within a few days. Trapped osteoblasts become osteocytes (Figure 1.5b). Accumulated osteoid is laid down between embryonic blood vessels, which form a random network. The result is a network (instead of lamellae) of trabeculae. Vascularized mesenchyme condenses on the external face of the woven and becomes the periosteum (Figure 1.5c). Bone collar of compact bone forms and red marrow appears. Spony bone (diploe), consisting of distinct trabeculae, persists internally and its vascular tissue becomes red marrow (Figure 1.5d).

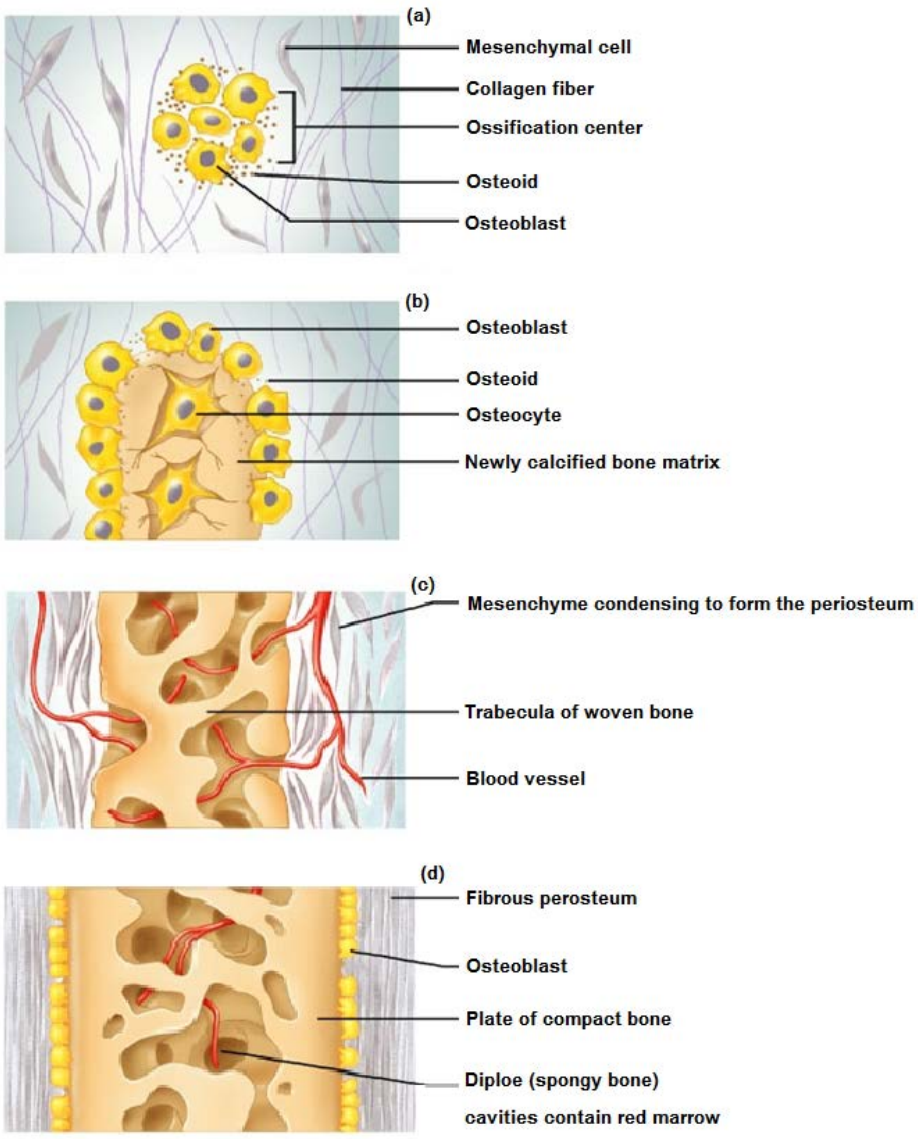

Figure 1.5 Processes of intramembranous ossification [22]

1.1.4.2 Endochondral Ossification

In endochondral ossification, bone replaces the cartilaginous models of the bones. The cartilage is gradually replaced by the calcified bone matrix that makes these bones capable of bearing weight. Bone collar around hyaline cartilage model is form. Chondrocytes at the center of the growing cartilage model enlarge and then die as the matrix calcifies (Figure 1.6a). Newly derived osteoblasts cover the shaft of the cartilage in a thin layer of bone (Figure 1.6b). Blood vessels penetrate the cartilage and the internal cavities are invaded by the periosteal bud and spongy bone formation. New osteoblasts form a primary ossification center (Figure 1.6c). The bone of the shaft thickens, and the cartilage near each epiphysis is replaced by shafts of bone. Blood vessels invade the epiphyses and osteoblasts form secondary centers of ossification (Figure 1.6d). The formation of the medullary cavity as ossification centers begins in the epiphyses in preparation for ossification of the epiphyses. When completed, hyaline cartilage remains only on the epiphyseal plates and articular cartilages (Figure 1.6e).

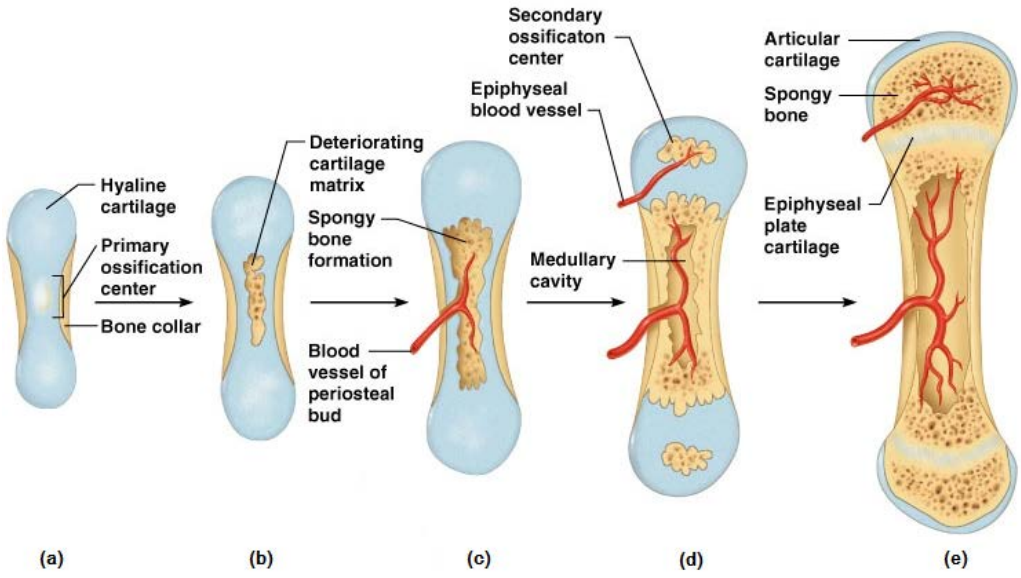

Figure 1.6 Processes of endochondral ossification [22]

1.1.5 Morphology of fracture region in healing process

Within the fracture healing process, there are four main spatial zones in consecutive phases. The defined steps in bone healing consist of overlapping phrase of regenerative activity as follow.

1.1.5.1 Hematoma and inflammatory phase

After the bone tissue has fracture, the hematoma and inflammatory phase is the immediate reaction (Figure 1.7a). Bleeding occurs at the bone and the surrounding soft tissue. Blood escapes from ruptured blood vessels and forms a hematoma to close the wound in the space between the defect bones. The microvascular disruption leads to hypoxia and causes ischemic necrosis of the affected bone. The hematoma coagulates around the bone extremities and within the medulla, forming a template for callus formation. The defect hematoma releases inflammatory mediators (cytokines) entering in the defect location and initiates the inflammatory responses such as increasing blood flow, blood vessel permeability and cell migration. At the same time, macrophages remove the debris and osteoclasts are activated to resorb bone debris. This hematoma forms within 6 to 8 hours and completes after 7 days.

1.1.5.2 Soft callus formation

Tissue repair begins, soft bridging of bone is forms, and a soft callus fills the space between the ends of the broken bone (Figure 1.7b). During this process, the progenitor cells differentiate into chondrocytes and build up a cartilaginous matrix mainly consisting of collagen type II, and containing a lot of other functional non-collagenous proteins. These are replaced by an osteoid matrix rich in type I collagen and then the ossified cartilage is replaced progressively by woven bone. This phase occurs over 3-4 weeks**.**

1.1.5.3 Hard callus formation

In this phase, hard bridging of bone is formed. Osteoblasts produce trabeculae of spongy bone and convert the soft callus to hard callus that joins the broken bones together (Figure 1.7c). The bone development of the cartilage template starts to mineralize. The inner layer of periosteum is rich in osteoblasts which synthesize a matrix rich type I collagen, generating calcified tissue. The hard callus formation occurs over 3-4 months.

1.1.5.4 Remodeling

In bone remodeling, it is the process resulting in a balance between the resorption of hard callus by osteoclasts and bone deposition by osteoblasts in which the new woven is slowly replaced by lamella bone (Figure 1.7d). The full union takes place within 3-6 months.

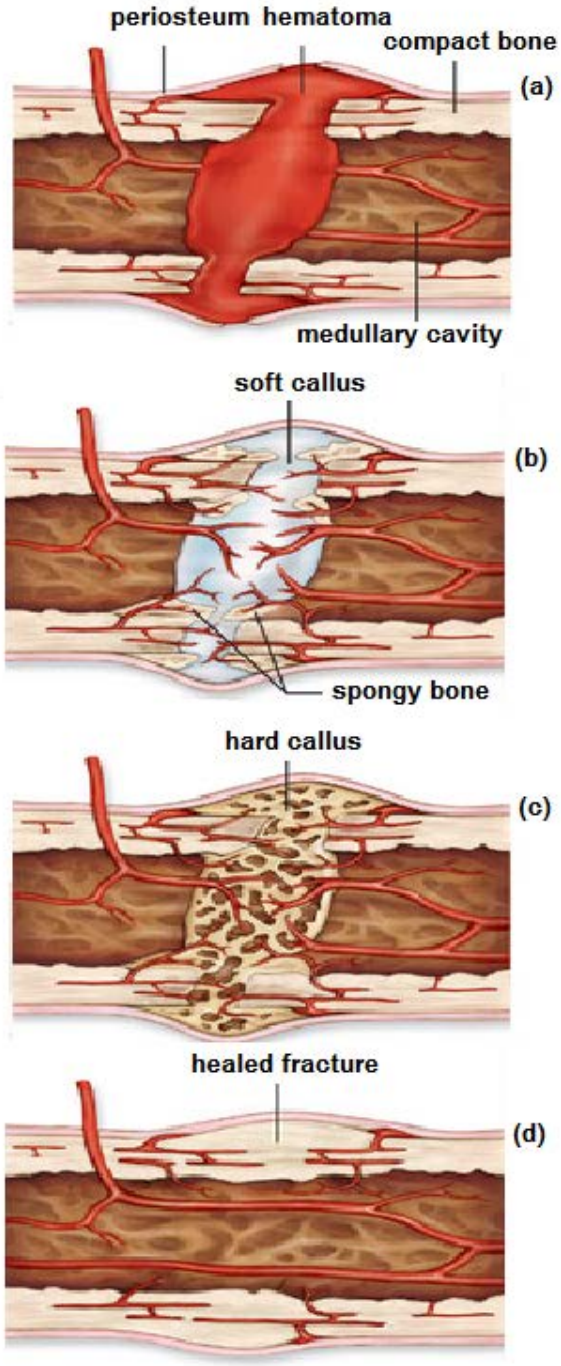

Figure 1.7 Schematics of the healing for fractured bone including hematoma phase (a), soft callus formation (b), hard callus formation (c) and remodeling phase (e) [23]

Bones can be self-healing, which do not regenerate spontaneously, if the critical size defect (CDS) injury is exceeded [24, 25]. This condition generally occurs when the size of the defect is 2 to 3 times the diameter of the involved bone. During healing of critical-sized defect, fibrous nonunion can form though a combination of fibrous and bony healing that does not return bony continuity and function. Additionally, CSD reveals some factors, including: (1) an uneven gradient of soluble osseous growth factors in the wound, which fail to reach the center of the defect and uniformly promote osteogenesis; (2) uneven biomechanical stress and loading, especially toward the center of defect, which reduces uniform bone cell migration, adhesion, and subsequent osteoid and bone matrix formation; and/or (3) the differential and more rapid migration of fibroblasts (compared to osteoblasts) into the would site during healing, which results in a higher prevalence of fibrous tissue in the center of defect [25-28]. In consequence, CSDs represent major clinical problems in reconstructive orthopedic surgery. Several investigations have evaluated to overcome the problem in the healing of CSDs or large defect bones. Biomaterials used in combination with bone tissue engineering offer to restore the function and/or replace the damaged or diseased bony tissue of CSDs thorough the principles of osteogenesis, osteoconduction, osteoinduction, and osteointegration [29-31].

1.1.6 The requirement of bone healing

In large bone defects, the bone healing by using biomaterials involves the major essential processes are osteogenesis, osteoconduction, osteoinduction and osteointegration.

1.1.6.1 Osteogenesis

Osteogenesis is defined as the capacity of new bone formation by osteogenic cell. This process depends on the presence of the osteogenic cells, which are preserved by diffusion from the surrounding host tissues. A material is referred to as osteogenic when it supports osteoblasts in producing minerals for the calcification of a collagenous matrix [32].

1.1.6.2 Osteoconduction

Osteoconduction means the process of living cells grown on a surface, which results in new bone formation. This process is to serve as a barrier to prevent the penetration of foreign tissue into the defect site. This phenomenon is frequently realized in the case of bone implants. Additional properties like the favoring of cell attachment, proliferation and migration in the implant structure and the capacity for mass transfer and vascularization are factored into this term as well [13, 32-35].

1.1.6.3 Osteoinduction

Osteoinduction is the process of stimulation of mesenchymal stem cells or other osteogenic cells to differentiate and develop towards the bone-forming cell lineage. It is directly related to the application of growth factors. Additionally, it is a phenomenon regularly seen in any type of bone healing situation [13, 32-35].

1.1.6.4 Osteointegration

Osteointegration (also called osseointegration) is a living process, which refers to a direct attachment of bone-to-metal interface without intervening connective tissue [36]. Osteointegration is used for an implant which is tolerated inside the body and incorporated into the tissue with direct contact to the living bone [13, 33].

1.1.7 Osteomyelitis (OM)

Osteomyelitis (OM) refers to bone and marrow cavity infection, always caused by microorganisms. OM is a difficult-to-treat bone infection characterized by progressive inflammatory destruction of the bone, bone necrosis, and new bone formation. In adults, OM is usually a complication of open wounds involving the bone, from fractures, surgery, or both. In

addition, several conditions of bone injuries such as trauma, ischemia, and foreign bodies can predispose to OM. The risk and severity of infection can be enhanced by the presence of a foreign body (metallic or prosthetic devices). It is reported that 0.4% to 7% of trauma and orthopedic operations are complicated by OM. This infection can also develop in a noninjured bone after bacteremia, mostly in prepubertal children and elderly patients, when the infection involves the axial skeleton. Despite appropriate combined medical and surgical therapies, up to 30% of OM become chronic, causing major economic losses and personal morbidity and mortality. Much attention has been dedicated to improve the surgical and medical treatment of OM, but little progress has been made toward understanding its pathogenesis. When the bone becomes infected, blood vessels in the marrow may be reduced or cut off. There are pus spreads affecting both the medullary and periosteal blood supplies, thereby impairing blood flow. Decreased vascular function likely decreases the amount of oxygen available to tissues at and around the fracture site, impairing the exchange of nutrients, and potentially leads to problems during the recruitment of cells to the injury site. These events, alone or in combination, lead to the formation of sequester or necrotic bone, which is considered the hallmark of chronic disease and may contribute to delay healing of any segmental defect. Furthermore, drug molecules cannot reach such infected areas when administered by systemic route. The symptoms of OM are variable. In the typical form, fever, pain, motor limitations and local inflammation or septicemia, are found, as usually as any infectious diseases. Bone infection leads to tissue destruction, which can result in the functional loss of the involved bone and the surrounding soft tissues. Ultimately, the disease can be the cause of death. Normally, bone is highly resistant to infection, and is a very forgiving tissue. It can generate itself into a healthy bone, by building new osteons when the native structure of the bone is injured. However, infected bone can occur after large bacterial inoculums, trauma or the presence of foreign bodies [37, 38]. Generally, microorganisms infect bone through one or more of basic method: haematogenous spread from other sources of infection, from the skin or other external contaminants through open fracture or trauma or following placement of internal fixation devices. Certain major causing pathogen of the infection is *Staphylococcus aureus* [39].

1.1.7.1 *Staphylococcus aureus*

Staphylococcus aureus is found as parts of the normal flora of skin and nasal passages. It is a spherical Gram-positive bacterium and is apparent in pairs or in irregular, short chains or bunched, or grape-like clusters under microscopic examination (Figure 1.8). The term *Staphylococcus* is derived from the Greek term *staphyle,* meaning "a bunch of grapes." Staphylococci are nonmotile, non–spore-forming, and catalase-positive bacteria. The cell wall contains peptidoglycan and teichoic acid. The organisms are resistant to temperatures of as high as 50°C, to high salt concentrations, and to drying. The colonies are usually large (6-8 mm in diameter), smooth, and translucent. Most strains are pigmented, ranging from cream-yellow to orange. The bacterium can cause infections if it enters the body and has developed resistance to beta-lactam antibiotics, including methicillin and other more common antibiotics such as oxacillin, penicillin, amoxicillin and oxacillin. A more dangerous form of *S. aureus* is known as methicillin-resistant *S. aureus* or MRSA.

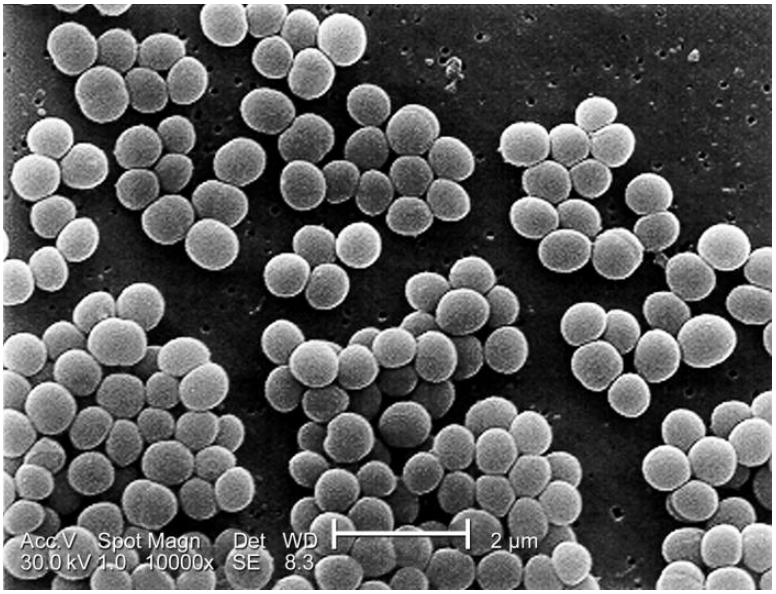

Figure 1.8 SEM image of *S. aureus* under a high magnification of 10,000x [40]

1.1.7.2 Methicillin-resistant *S. aureus* (MRSA)

MRSA is a type of bacteria that is resistant to a number of widely used antibiotics. This means that it can be more difficult to treat than the others. MRSA infections are more common in people who are in hospital or nursing homes. It is known as community-associated MRSA (or CA-MRSA). The bacterium is also common in crowded environments where there is frequent skin-to-skin contact and hygiene is poor, such as homeless shelters or army bases.

1.1.7.3 Pathogenesis

The initial occurrence is the expression of a large number of cell surface proteins named microbial surface components recognizing adhesive matrix molecules (MSCRAMMs) that mediate adherence to host tissues and begin colonization leading to an infection [41]. The proteins adhere to the bacterial extracellular matrix (ECM), called bacterial adhesins. Each adhesin specifically interacts with one of host protein components, e.g. fibrinogen, fibronectin, collagen, vitronectin, laminin, thrombospondin, bone sialoprotein, elastin, or von Willebrand factor. Then, *S. aureus* promotes invasion or tissue penetration by specifically attacking host cells (exotoxins) or degrading components of extracellular matrix (various hydrolases). The ability of *S.aureus* to invade cells may explain its capacity to colonise tissues and to persist after bacteraemia. *S. aureus* can also promote its endocytic uptake by epithelial or endothelial cells, and can form biofilms, leading to the difficulty to treat with antimicrobial agents. The inherent resistance of biofilms to antimicrobial factors seems to be mediated by several factors including low metabolic rates, adaptive stress responses, and down regulated rates of cell division of the deeply embedded microbes. The progressive development of OM at defect site is displayed in Figure 1.9

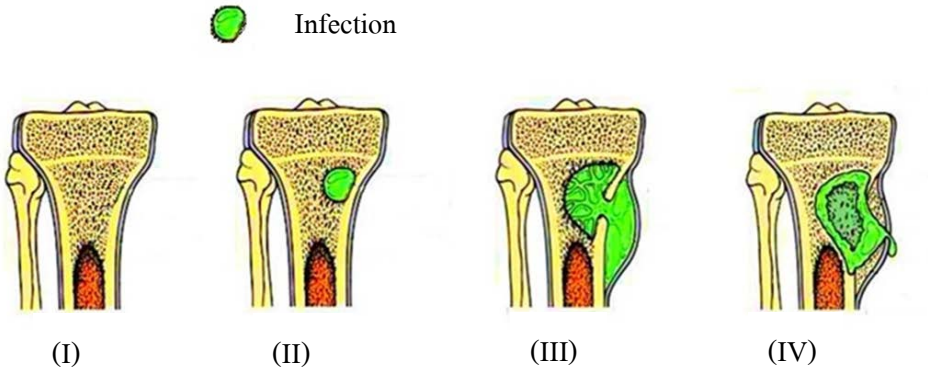

Figure 1.9 Steps in the progressive development to OM of bone: normal bone (I), bacteria adhere to the bone and form biofilm (II), when they reach the metaphysis, OM can be developed, resulting in blood supply blockage, abscess formation, and finally bone destruction. Additionally, there is an area of devascularised dead bone, and progression of infection towards an intracapsular location. Inside the infected bone cavity, the pus spreads thought the haversian canels of the compact bone to the outside (III), extension of sequestrum and necrotic through cortical bone create fistula, sinuses and ultimately breaks. These sinuses traverse the bone and persist there for long time. The slow bone healing process and tissue inflammation can thus be observed (IV) [38]

The goal of treatment is to eliminate infected bacteria, and to prevent the development of chronic infection. Early antibiotic treatment, before extensive destruction of bone or necrosis, produces the best results and must be administered parentally for at least four weeks but usually six weeks to achieve an acceptable curing rate. OM in avascular zones prevents the delivery of drugs from conventional routes of administration. Current treatment strategies involve surgical curettage of infected bone, followed by parenteral administration of high doses of antimicrobials for 4–6 weeks [42, 43], as causative organisms are known to produce large amount of glycocalyx material and necrotic bones providing a surface suitable for the development of biofilm [44]. Prolonged hospitalization for parenteral administration makes the therapy further costly and inconvenient. Moreover, other treatment forms of OM can be surgical debridement, soft tissue coverage, hyperbaric oxygen, and for locally administrating of antibiotics. Systemic antimicrobial treatments give rise to the need of high serum concentration of the drugs for extended periods and thereby causing drawbacks such as higher incidence of side effects, cost and low patient compliance. Local antibiotic treatment seems to be an ideal method by providing better patient compliance and avoiding adverse effects such as ototoxicity and nephrotoxicity. Furthermore, local delivery system offers several advantages including high concentrations of therapeutic agent available at the target site, releasing drug locally for prolonged periods and at concentrations generally higher than those achieved by multidose parenterals [45]. The delivery system is viewed as alternative choice for treating OM [42, 46]. However, drug diffusion can be an important limitation in that the diffused drugs provide systemic side effect as well. To improve the effectiveness of local delivery system, drug molecules should be incorporated in suitable carriers, and the carriers should have properties matching the properties of bones to be implanted. Moreover, the controlled release systems may be necessary for improving bioavailability. The carriers should be designed to deliver therapeutic molecules at a specific rate for a specific period of time at the desired site.

1.1.7.4 Treatment of OM by antibiotics

Since the most common cause of chronic OM is *S. aureus* which can develop resistance to the more dangerous form of MRSA, the most widely acceptable agents in local delivery systems are able to reduce the toxicity of individual agents, to prevent and the emergence of resistance and to treat mixed infections involved in OM, which have the following characteristics:

(1) be active against the most common bacterial pathogens involved in chronic OM

(2) be locally released at concentrations exceeding several times (usually 10 times) the minimum inhibitory concentration (MIC) for the concerned pathogen

(3) be unable to enter in the systemic circulation

(4) be not exist any adverse effects

(5) be stable at body temperature and water soluble to ensure diffusion from the carrier

(6) be not produce supra infection

Vancomycin is the drug of choice for treating OM [47-52]. The antibiotic has been reported not affecting the growth of skeletal cells and osteoblasts, thus suitable to be loaded into scaffolds for potential use in treatment of severe cases of OM.

1.1.7.5 Vancomycin

Vancomycin (VCM) remains a strandard treatment for MRSA infection during the past decades [53]. It is a potent tricyclic glycopeptide antibiotic (Figure 1.10) that inhibits the cell wall synthesis of susceptible organisms. The drug has been recognized as an effective therapeutic agent for treatment of serious infections caused by gram-positive bacteria, especially in recalcitrant staphylococcal infections. Different strategies have been developed for the delivery of VCM from polymers, such as poly(trimethylene carbonate)-based surface-eroding delivery systems [54] and nanoparticles presenting VCM on the surface [55]. Ideally, the delivery system should deliver VCM well above the effective antibacterial concentration in a sustainable manner [56]. Since OM has the sheltered environment provided by necrotic bone and the quiescent state of bacteria in sequestra, it has been suggested that the administration of VCM requires a long therapeutic course to provide a sufficient concentration level in the bone, and the release of antibiotic at concentrations exceeding the MIC for 6–8 weeks is desirable [57]. Thus, one purpose of the present study is to fabricate biodegradable scaffolds containing VCM as local carrier system for sustainable release with tunable kinetics, where the release of biologically active VCM is extended to 6–8 weeks so that the processes of angiogenesis and new bone formation can proceed unimpeded by the infection.

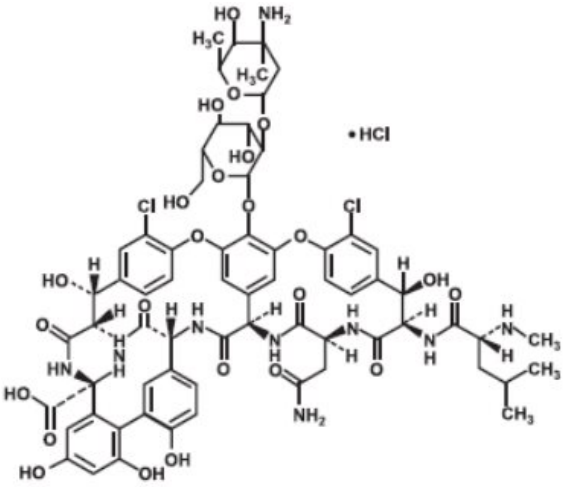

Figure 1.10 VCM hydrochloride [58]

1.1.8 Biomaterials used as drug delivery system (DDS) in OM

A variety of biomaterials have been used as DDS for repair and replacement of damaged or traumatized bone tissues, which can be divided into 2 types: non-biodegradable and biodegradable materials (Figure 1.11). Advantages and limitations of these materials are described below.

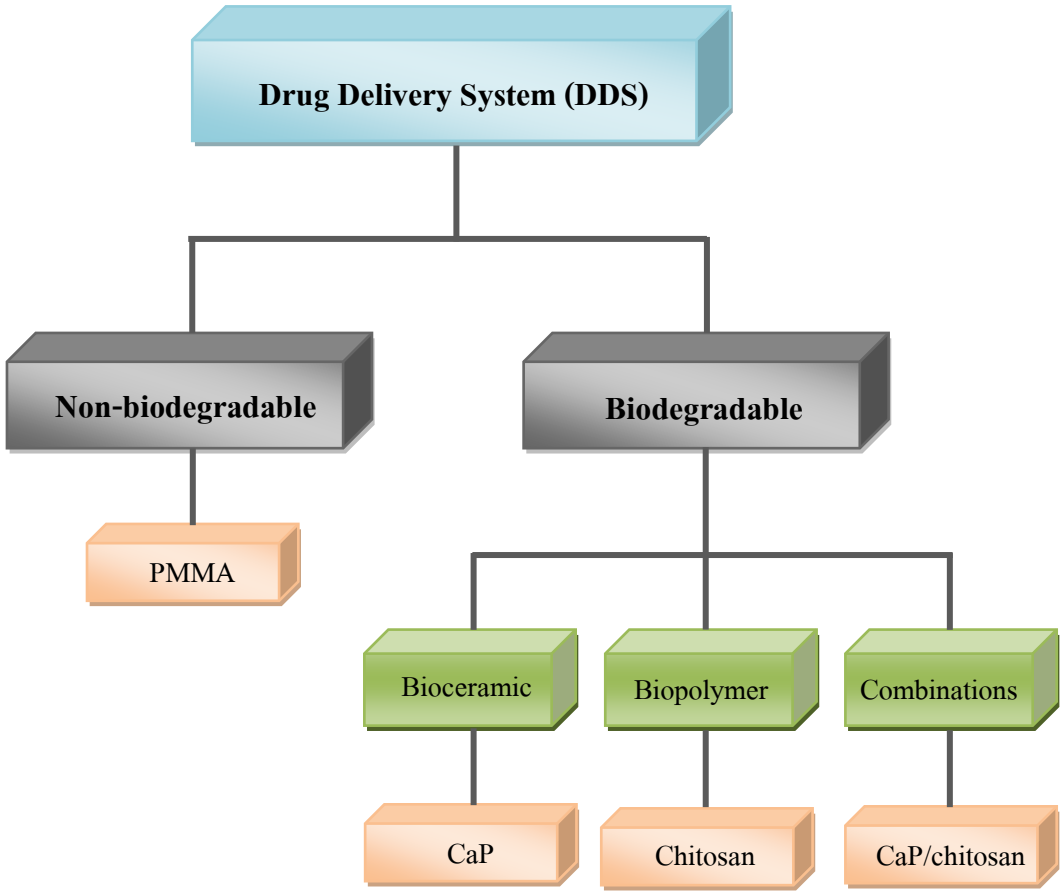

Figure 1.11 Types of DDS for bone tissue engineering

1.1.8.1 Non-biodegradable materials

The most extensively and commercially available biomaterial for non-biodegradable DDS is poly (methyl methacrylate) or PMMA. However, its use is associated with several drawbacks. For example, during mixing and curing of PMMA, an exothermic reaction occurs, and the temperature may increase up to 100 ºC, which decreases the effectiveness of some antibiotics [59]. Another drawback includes the requirement for surgical removal after treatment. The surgery to remove the implanted material is usually more difficult than implantation because of localized scarring and adhesion and may impart additional risk for postoperative infection depending on the condition of the patient. Additionally, a significant proportion of antibiotics may be retained within the cement (less than 10% of the entrapped drug is eventually released), potentially generating resistant bacteria on the carrier surface during later stages of low-level antibiotic release [56, 60-63]. Fortunately, all the described problems can be solved by using biodegradable drug delivery system.

1.1.8.2 Biodegradable materials

The biodegradable materials have the obvious advantage in eliminating the need for additional surgery to remove the drug carrier. The biodegradable materials may result in high release. They are gradually replaced by ingrowing tissue [64, 65]. Furthermore, secondary release of the antibiotic may occur during the degradation phase of the carrier, this could increase the antimicrobial efficacy compared to non-biodegradable carriers [66]. In addition, the drug carrier does not prevent the formation of new bone due to its degradation in the implanted area. Various biodegradable devices made from natural or synthetic polymers have been investigated as local antibiotic delivery systems. The degradation properties of these polymers can be tailored for the controlled release of antibiotics for long periods and eliminate the need for surgical removal of the implant. The three main biodegradable materials include bioceramics, polymer and composites of ceramics and polymers. An example of biodegradable-ceramics is calcium phosphate based ceramics, such as hydroxyapatite ($Ca_{10}(PO_4)_6(OH)_2$, HA). The material has been used in a range of medical applications including coatings for hip replacements and bone grafting

materials [67-69]. An example of natural biopolymers is chitosan. It is a deacetylated derivative of chitin, which commonly found in the shells of marine crustaceans and cell walls of some fungi.

The principles of using biodegradable DDS are in the following (Figure 1.12). There is a large gap at the defect site, which will be implanted with optimal scaffolds, designed for controlled degradation and drug release, and having mechanical properties matching to the site of implantation. The rates of scaffold degradation and bone formation should match to each other. The new bone tissue can form and integrate with native surrounding tissue, resulting in complete healing.

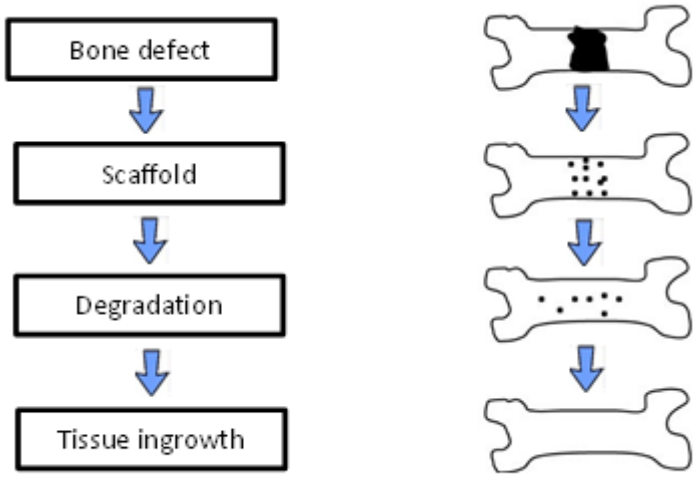

Figure 1.12 Steps in bone tissue engineering using biodegradable 3D scaffolds. Under the optimal controlled manner, the generation of complete new bone tissue is achieved.

There are 4 steps necessary to concern in developing DDS for treatment of bone infection as detailed:

(1) Fabrication of drug carriers or scaffolds having physicochemical properties advantageous for improved bone healing

(2) Drug entrapment/encapsulation with release profiles of the loaded drug being tailored for obtaining optimal treatment

(3) Implantation of the obtained scaffolds being evaluated for curing efficiency *in vivo*

(4) Bone healing/regeneration being assessed clinically

1.1.9 Scaffolds design and processing

The design and processing of a porous, biodegradable 3D structure called a scaffold is a key component for bone regeneration. Scaffolds serve as a matrix for cell interactions and the formation of bone-extracellular matrix providing structural support of the newly formed tissue [70]. More importantly, scaffolds should meet certain criteria of mechanical property, biocompatibility and biodegradability, as well as bone morphology, structure and function in order to maximize integration into surrounding tissue [71].

The major problem of infected areas with critical size bone defects is that cells cannot skip from one edge of the bone defect to another. These cells need a solid platform to build bone and unite the fracture. The materials should also interact with biological environment around the fracture site to enhance biological response and tissue/surface bonding. In addition, it should have the ability to undergo progressive degradation whilst new tissue regenerates and heals. All aspects of cell response including cell adhesion, migration, proliferation and differentiation should be operated in the scaffolds. So, there must be the correct balance between architectural features of scaffolds and the cell functions [72, 73]. In addition, the implant itself should be osteoinductive, which is the ability of biomaterials to induce *de novo* bone formation [13]. Researches have shown that cells can attach and organize on the nanometer-scale materials better than micro-scale scaffold [74].

Many studies have composed biodegradable polymer with bioactive ceramics for improving the resorbability, bioactivity and mechanical properties of scaffolds [75, 76]. Some calcium phosphate (CaP) ceramics used clinically as bone substitutes has been in a porous form [71, 74].

1.1.10 Nanoscale biomaterials as scaffolds

The research trends of biomaterials as scaffolds are focused on the formation of nano-size ranged bioceramics. There are to overcome the biomaterial limitations, since conventional HA shows a low surface area and has strong crystal-to-crystal bond. The wet chemical precipitation method has been reported for the synthesis of nanometer-sized hydroxyapatite [77, 78].

1.1.11 Calcium phosphate-based materials

In biomedical application, calcium phosphates including hydroxyapatite (HA) and tricalcium phosphate (TCP) are primarily used as bone substitutes because there are biocompatibility, low density, chemical stability and their compositional similarity to the mineral phase of bone [79]. The conventional HA has been used in the forms of thin film, powder, dense or porous blocks [80]. Due to its highly stable and less bioresorbable, these can impede the rate of bone regeneration when solely used as a bone substitute [81]. Instead, their resorbability can be enhanced by improving degree of crystallinity to be similar to biological materials when the grain sizes are reduced to nano-scale range [82, 83].

1.1.11.1 Hydroxyapatite

Hydroxyapatite (HA) with the chemical formula $Ca_{10}(PO_4)_6(OH)_2$ is defined as basic composition of the bone mineral component. Bone apatite crystals containing divalent cations and anions such as Mg, carbonate, and acid phosphate are very small. This phase can occupy sites in the apatite matrix and thereby create an irregular crystal lattice. The results are

that the apatite is more readily solubilized, and this property permits the mineral phase to participate in the homeostatic process as a virtually unlimited source of Ca, Mg, and PO_4 is supplied.

The ceramic is known for its excellent biocompatibility not only with hard tissues e.g. bone and teeth, but also with soft tissues e.g. skin, gum and muscle. Therefore, it is an ideal candidate for components of implants [84]. However, HA does not degrade significantly and shows limited ability to promote the development of new bone tissue [85, 86]. Biological apatites contain various amounts of anionic (e.g., F^-, Cl^-, SiO_4^{4-} and CO_3^{2-}) and/or cationic (e.g., Na^+, Mg^{2+}, K^+, Sr^{2+}, Zn^{2+}, Ba^{2+}, Al^{3+}) substitutions [87, 88]. The role of silicon (Si) in bone has been investigated since the early 1970s by Carlisle [89], as being relevance on bone formation and calcification. In biomaterial science, there are ways to enhance properties of synthetic HA by introducing various ionic substitutions into its apatite structure [90]. One of the most interesting substitutions is the incorporation of Si that found to considerably improve bioactivity of the synthetic apatite [91]. The rate of bone apposition has been significantly greater at the surface of Si-substituted HA (Si-HA) than of the HA ceramic [92]. More rapid remodeling of bone surrounding the Si-HA has been observed [93]. The former material has shown enhanced apatite formation *in vitro*, increased cell proliferation *in vitro*, and enhanced new bone formation *in vivo* [94-102]. Indeed, lack of Si has been the cause of various bone diseases [103-105]. As believed, the positive biological effects of Si play important roles in bone repair. These findings have supported the use of Si-HA, and several methods for Si substitution into HA crystals has been developed [94-96, 99, 106-117]. However, it seems that the previously documented methods have been impractical [118, 119]. For examples, Ruys prepared Si-HA by using sol-gel approach, resulting in materials containing Si-HA and other phases such as calcium silicophosphate [118]. Other shortcomings of the sol-gel approach that have been reported include high cost of alkoxide-based starting materials, the complicated steps in order to complete the dissolution of the starting materials [120]. Boyer et al. prepared Si-HA by solid-state reaction. However, the incorporation

of other secondary ions, like La^{+} or SO_4^{2-}, has been detected, resulting in materials that are not Si-HA [119]. Tian et al. used mechanochemical method for the synthesis of Si-HA in which conventional milling equipment and aqueous phase has been essential [112], leading to the method limitation [112]. Tanizawa and Suzuki used hydrothermal method. The acquired materials had a Ca/(P+Si) ratio higher than that of using pure calcium HA, and were not stable above 145°C [121]. Gibson et al. synthesized Si-HA by using wet chemical method. The *in vitro* bioactivity study gave good results [98]. The last mentioned method is widely used for preparing Si-HA [93, 95, 122-125], due to its simplicity, low cost, and low processing temperature [126], and had been suggested as a valuable method for Si-HA synthesis in industrial scales [127-134].

1.1.12 Chitosan

Chitosan is a linear deacetylated polysaccharide composed of glucosamine and *N*-acetyl-D-glucosamine (GAG) monomer as shown in Figure 1.13 [135, 136]. The glucosamine/N-acetyl glucosamine ratio is referred to as the degree of deacetylation that is depended on sources and preparation procedures. Its molecular weight may range from 300 to over 1000 kDa with the degree of deacetylation ranging from 30-95% (DDA). Chitosan is soluble in dilute acetic acid when the DDA is >40%, and displays interesting biological properties as summarized in Table 1.3

Table 1.3 Biological properties of chitosan [137]

Advantages	**Limitations**
Non-toxicity	Poor mechanical property
Biocompatibility	
Biodegradability and enzymatic hydrolysis	
Hemostatic activity	
Anticoagulant activity	
Anti-inflammatory action	
Angiogenesis stimulation	
Mucoadhesive property	
Suitability for cell ingrowth and osteoconduction	
Antimicrobial activity	
Wound healing acceleration	
Cell binding activity	

Moreover, the degradation products of chitosan are nontoxic, nonimmunogenic, and noncarcinogenic, supporting the material for tissue engineering applications as scaffolds. Several researches have indicated that chitosan can reduce the infection rate of experimentally *S. aureus* induced OM in rabbits [138]. In bone tissue engineering, chitosan has been shown to promote growth and mineral rich matrix deposition by osteoblasts in culture [139]. It is described to have inhibitory effect on fibroblasts while stimulating osteoblast activity [140]. Therefore, it is not only osteogenic, osteoconductive or osteoinductive, but also be of some cartilage-specific glucosaminoglycans (GAGs) which makes it an ideal polymer for bone tissue engineering [140-143]. Besides, chitosan has haemostatic and antimicrobial features which is the important advantages for the implantation into damaged tissue [143]. The polycationic nature of chitosan facilitates cell adhesion and electrostatic interactions with anionic compounds like GAGs or several proteins [143]. The extent of chitosan biodegradation can be regulated by the use of materials differing in the degree of degradability [143, 144]. Several studies have focused for this purpose by using composites of chitosan–CaP [145] or chitosan-HA [146].

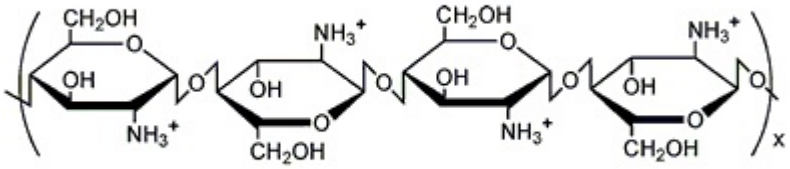

Figure 1.13 Chemical structure of chitosan [147]

The cationic of chitosan is responsible for its use in drug delivery systems. The incorporation of multivalent inorganic anions such as tripolyphosphate (TPP) (Figure 1.14**)** can be used to achieve a sustained delivery system by forming stable complexes from which the drug is released over a more prolonged time period [148]. The crosslinking between chitosan and TPP is shown in Figure 1.15

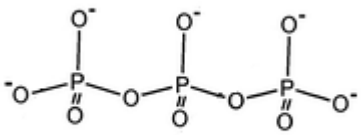

Figure 1.14 Chemical structure of TPP [147]

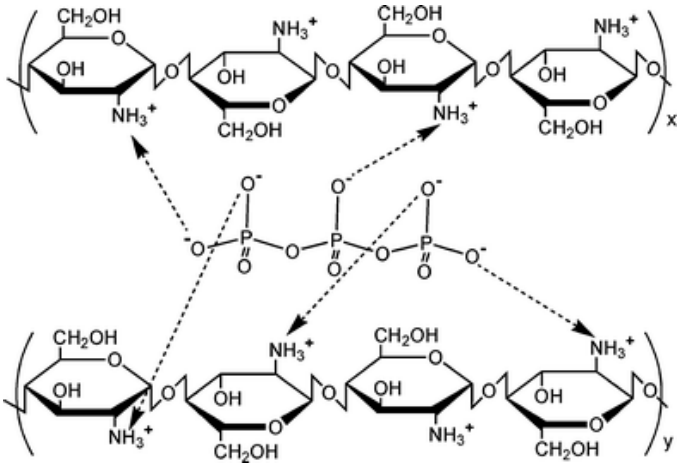

Figure 1.15 Schematic presentation of TPP-chitosan crosslinking [147]

1.1.13 Growth factor in bone tissue engineering

Growth factors are proteins secreted by many cell types that act on the appropriate target cell or mediator cells to carry out a specific action [149]. They are as signaling molecules that promote and/or prevent cell adhesion, proliferation, migration and differentiation by up-regulating or down-regulating the synthesis of proteins, growth factors and receptors. These molecules are essential for tissue formation and play an important role in tissue engineering. Growth factors are expressed during different phases of fracture-healing. It has been thought that they may serve as potential therapeutic agents to enhance bone repair, including acceleration of fracture-healing, or treatment of established nonunions. The major players in skeletal tissue engineering are the members of transforming growth factor β (TGF-β) superfamily notably the bone morphogenetic proteins (BMPs) [150].

1.1.13.1 Bone morphogenetic proteins (BMPs)

Bone morphogenetic proteins (BMPs) are a family of osteoinductive proteins, playing important roles in skeletal development and bone formation [151-154]. Twenty different BMPs have been identified with varying degrees of cartilage and/or bone inductive properties [154]. Numerous studies have confirmed the osteoinductive potential of recombinant human BMP2 (rhBMP2) and rhBMP7, leading to the U.S. FDA approval as biologic agents used in regenerative medicine for treatment of severe orthopedic conditions [155].

1.1.13.1.1 Bone morphogenetic protein 2 (BMP2)

BMP2 is a glycoprotein with low molecular weight in the TGF-ß family. Native bone contains approximately 1-2 micrograms of BMP per kilogram of cortical bone [156, 157]. The dimeric conformation of BMP2 is critical to the bioactivity, and is very sensitive to environmental conditions [158]. BMP2 is most soluble at pH < 5; however, the solubility at pH > 6 (i.e. physiologic pH = 7.4) is greatly increased in solvents such as heparin solutions [159]. It has been proven as a strong osteoinductive factor for treatments of bone fractures and defects [160, 161], by increasing proliferation and the synthesis of ECM, but decreasing ECM degradation [162]. BMP2 expression is extremely high at the early stages in order to initiate and direct migration of progenitor cells for bone formation, which is critical to the proper healing of damaged tissue [163-166]. The protein has gained U.S. FDA approval for curing bony defect injury such as open tibial fractures [167]. However, delivery of BMP2 alone is minimally effective and not reasonable for clinical use due to the extremely high doses needed, leading to higher cost, faster degradation or denaturation [168]. To overcome these drawbacks, many methods have been designed for the delivery of BMP2. However, these delivery methods are still problems in controlling release rate, and often resulting in a high initial burst release [169]. Therefore, it would be ideal to develop a system for the sustained delivery of BMP2 over an extended time period, to promote osteoinductivity of scaffolds into the bony defect site and enhance functional repair of the defect site. To protect the protein structure from proteolytic degradation, some literatures have reported this by immobilizing into an ECM-like matrix [170,

171], using the unique binding property of the growth factor that naturally occurs. Molecules such as heparin has been adsorbed onto or covalently linked to scaffold surfaces to sequester growth factors such as bFGF, TGF-β2, BMP2 and NGF [172-179]. In consequence, the attachment of heparin to biomaterials may result in an appropriate matrix for binding and controlling sustained release of BMP2. Such binding also protects them from proteolytic degradation [180].

1.1.14 Heparin

Heparin has been shown to improve BMP2 activity by protecting the protein from degradation and blocking antogonist suppression [181]. Heparin (Figure 1.16) is an anionic glycosaminoglycan, and has inherent capacity to bind various growth factors via electrostatic interaction (Figure 1.17). This ability is profitable in that release of the bound proteins can be sustained. In this study, conjugation of heparin onto scaffolds was firstly developed. BMP2 was subsequently bound to heparin-conjugated scaffold for delivery purpose and being studied for its *in vivo* efficacy.

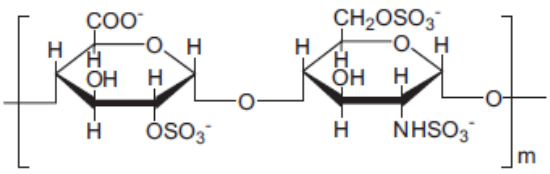

Figure 1.16 Structure of heparin [182]

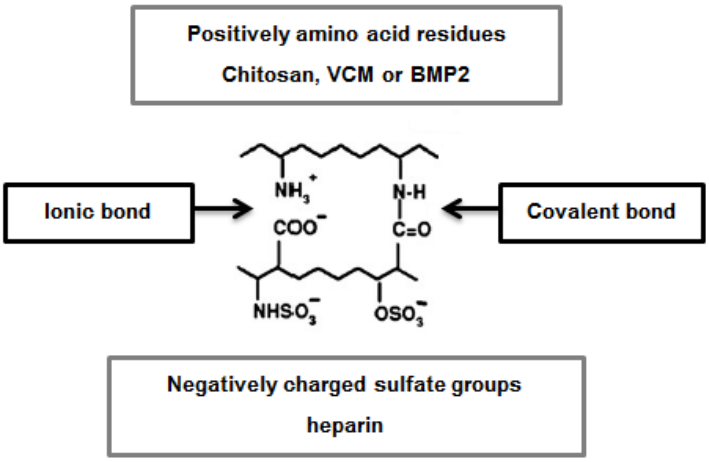

Figure 1.17 Interaction between heparin negatively charged sulfate groups and the proteins' positively amino acid residues [183]

1.1.15 Carbodiimide reaction

Carbodiimides provide the most popular, and are often used for immobilizing growth factors into surface biomaterial. The reagents are not parts of the crosslink, and not possibly cytotoxic, because their by-products are water soluble that can be easily removed. The reaction between carbodiimide groups (N=C=N) and carboxylic groups (COOH) has been suggested to occur at room temperature. The most common used carbodiimide is EDC or 1-ethyl-3-(-3-dimethylaminopropyl) carbodiimide hydrochloride (Figure 1.18), since it is water soluble. Low toxicity of the carbodiimide reaction has been estimated, since EDC is transformed into the nontoxic urea derivative in the coupling reaction [184, 185]. *N*-hydroxysuccinimide (NHS) (Figure 1.19) is often included in the reaction to improve efficiency of EDC coupling and crosslink primary amines to carboxyl-coated surfaces at physiologic pH more efficiently [186]. The carbodiimide reaction is shown in Figure 1.20

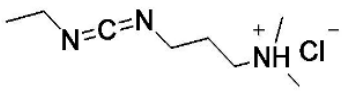

Figure 1.18 Chemical structure of EDC

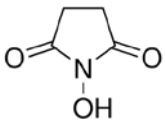

Figure 1.19 Chemical structure of NHS

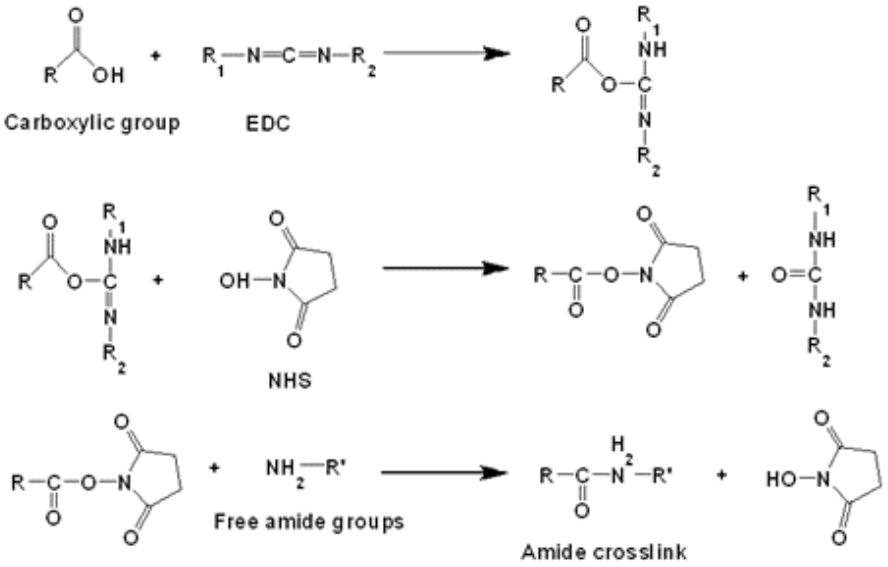

Figure 1.20 The carbodiimide reaction using EDC/NHS [187]

1.2 Rationale of the study

Nowadays, the regeneration of contaminated bony tissue defects, including OM remains an intractable problem of treatment. An ideal approach for curing the disease is the ability to decrease bacterial infection and repair the defect bone simultaneously. A drug administration by oral or systemic route may not reach therapeutic level at the infected areas due to scant numbers of blood vessels in the mineralized tissues. Furthermore, systemic antimicrobial treatments give rise to the need of high serum concentration of the drugs for extended periods and thereby causing drawbacks such as higher incidence of side effects, cost, and low patient compliance. Local antibiotic treatment seems to be an ideal method by providing better patient compliance and avoiding adverse effects such as ototoxicity and nephrotoxicity.

At present, there are no publications reporting in the modification of hydroxyapatite lattices by *in situ* chemical reaction. Therefore, the aims of this study are to find the most suitable condition for synthesis of Si-substituted HA to establish a new generation of biomaterials. All obtained products will be fabricated as delivery systems for administration of VCM and rhBMP2 to treat OM. The efficacy of the prepared delivery scaffolds will be evaluated *in vitro* and *in vivo*. Nanoparticles of hydroxyapatite containing Si in its structural lattices will be generated by the wet precipitation method. The physical characterization techniques including X-ray diffraction (XRD), X-ray fluorescence (XRF), Fourier transform infrared spectroscopy (FTIR), Scanning electron microscopy (SEM), Thermo-gravimetric analysis (TGA), and Measurement of zeta potential (ζ) will be performed. Three-dimensional (3D) structure of scaffolds will be stabilized by tri-sodium polyphosphate (TPP)–chitosan cross-linking. Vancomycin (VCM) will be adsorbed by the ceramic particles, prior to be used in fabricating scaffolds. A simple and fast method for heparin-mediated-rhBMP2 binding will be developed. The rhBMP2-loaded scaffolds will be evaluated for osteoinductive effect by subcutaneous implantation in rats to rule out periosteal bone formation, which can disturb the inducible effect of the protein [188]. Finally, VCM and/or rhBMP2-loaded Si-nHA scaffolds will be tested for the

antibacterial activity and bone regeneration capacity. The implant was designed as double-layered scaffold which was composed of 2 sections of VCM-loaded scaffold in the upper layer and rhBMP-loaded scaffold in the lower layer. All methods were planned with simple techniques in order to avoid the degradation and detachment of the bioactive molecule during preparation and surgical implantation. Double-layered scaffold was the fabricated scaffolds by combining two layers. These layers were obtained using two different drug loading (VCM and rhBMP2). The schematic design of this scaffold was shown in Figure 1.21. The outcomes are estimated in providing basis for further selection as lead biomimetic materials.

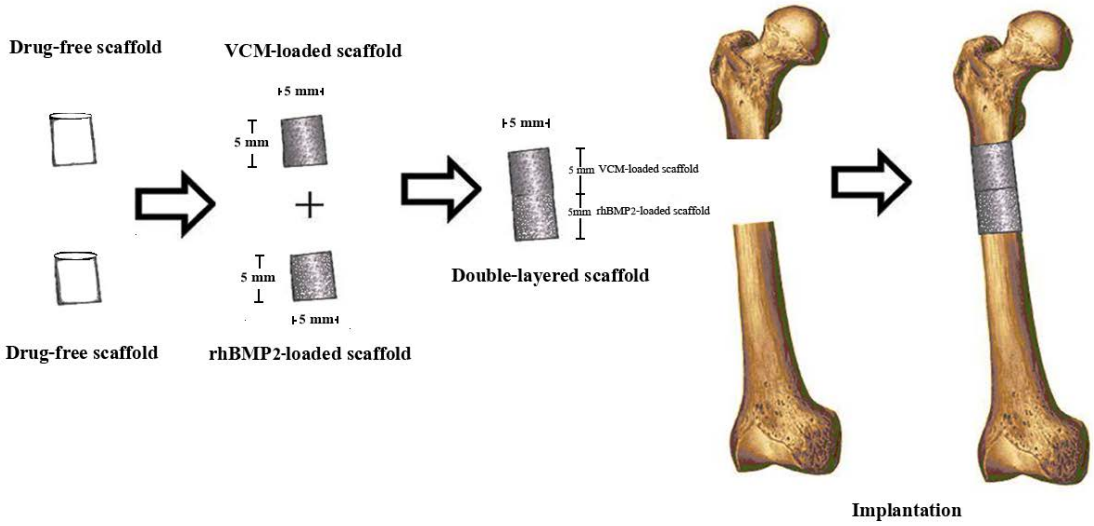

Figure 1.21 Concept of fabrication of double-layered scaffold for treating OM

1.3 Objectives

(1) To prepare silicon-substituted nano-hydroxyapatite (Si–nHA) powders that contain trace amount of silicon in its structural lattices, using commercial HA (Fluka) for the control group and $Ca(NO_3)_2$ and $(NH_4)_2HPO_4$ as starting substances of the tested group

(2) To generate apatite layer on the material surfaces

(3) To physically characterize the obtained powders by techniques including X-ray diffraction (XRD), X-ray fluorescence (XRF), Fourier transform infrared spectroscopy (FTIR), Scanning electron microscopy (SEM), Thermo-gravimetric analysis (TGA), and Measurement of zeta potential (ζ)

(4) To load vancomycin (VCM) onto the surfaces of the synthesized materials

(5) To study the release of calcium and phosphate from the synthesized materials

(6) To determine loading efficiency and drug release *in vitro*

(7) To assess the biocompatibility of VCM-loaded scaffolds

(8) To evaluated bone regenerative capacity of rhBMP2-loaded scaffolds *in vivo*

(9) To develop heparin immobilized scaffolds

(10) To find out the appropriate rhBMP2 concentration for loading onto the scaffolds

(11) To estimate *in vivo* efficacy of the rhBMP2-loaded scaffolds

(12) To induce OM in rat model

(13) To fabricate double-layered scaffold containing VCM and rhBMP2

(14) To evaluate the antimicrobial activity and osteogenic response for the developed drug carrier in OM animal

1.4 Research expectation

(1) Improved bioactive property of Si-nHA by using the simple method of wet chemical precipitation

(2) Obtaining the new double-layered scaffolds containing VCM and rhBMP2 for further applications in bone repair

CHAPTER 2

MATERIALS AND METHODS

This study was divided into 5 parts as detailed and summarized in Figure 2.1.

Part I: Synthesis of silicon (Si)-substituted nano-hydroxyapatite (Si–nHA) powders

Part II: The physical characterizations of the synthesized products, using techniques of X-ray diffraction (XRD), X-ray fluorescence (XRF), Fourier transform infrared spectroscopy (FTIR), Scanning electron microscopy (SEM), Thermo-gravimetric analysis (TGA), and zeta potential (ζ)

Part III: Fabrication of scaffolds containing the Si–nHA particles

Part IV: Drug loading and loading efficiency determination

Part V: Evaluation of drug-loaded scaffolds *in vivo*

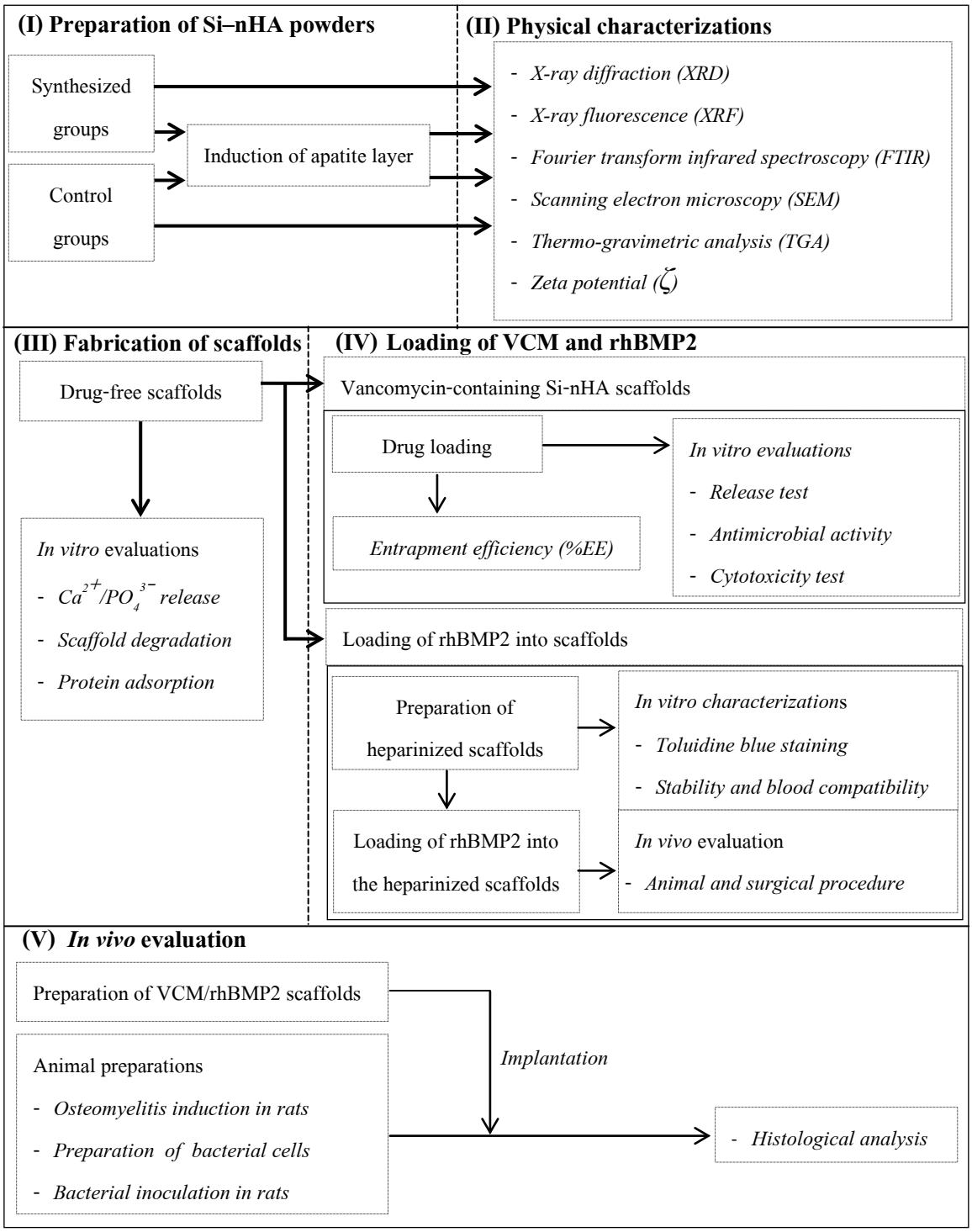

Figure 2.1 Five parts of the study, including synthesis of silicon (Si)-substituted nano-hydroxyapatite (Si–nHA) powders (I), the physical characterizations of the synthesized products (II), fabrication of scaffolds containing the Si–nHA particles (III), drug loading and loading efficiency determination (IV), and evaluation of drug-loaded scaffolds *in vivo* (V)

2.1 Materials

Chemicals/reagents and instruments used in this study as summarized in Table 2.1 and 2.2, respectively.

Table 2.1 List of chemicals and reagents, including the corresponding purchased company

Name of chemicals/reagents	Company
2-amino-2-methyl-1-propanol (AMP)	Sigma Aldrich (Switzerland)
2-morpholinoethane sulfonic acid (MES)	Sigma (Chicago, Illinois)
3-(4, 5-dimethylthiazol- 2-yl)-2, 5-diphenyltetrazolium bromide (MTT)	Sigma (Chicago, Illinois)
8-hydroxyquinoline	Sigma-Aldrich Corporation (St. Louis, MO, USA)
Acetic Acid (AA)	Sigma-Aldrich Corporation (St. Louis, MO, USA)
Acetone	RCI Labscan Limited (Bangkok, Thailand)
Alizarin red S (ARS)	Sigma-Aldrich Corporation (St. Louis, MO, USA)
Ammonia solution (25%)	Loba Chemie Pvt. Ltd. (India)
Ammonium molybdate	Sigma-Aldrich Corporation (St. Louis, MO, USA)
Antibiotic-antimycotic (penicillin/streptomycin/amphotericin B) solution (100X)	Gibco™ Invitrogen Corporation (Grand Island, NY, USA)
Ascorbic acid	Sigma-Aldrich Corporation (St. Louis, MO, USA)
Bacteriological agar	HiMedia Laboratories Pvt. Ltd. (Mumbai, India)
Boric acid	Sigma-Aldrich Corporation (St. Louis, MO, USA)
Calcium nitrate tetrahydrate ($Ca(NO_3)_2.4H_2O$)	Sigma-Aldrich Corporation (St. Louis, MO, USA)
Calcium silicate ($CaSiO_3$)	Sigma-Aldrich Corporation (St. Louis, MO, USA)

Table 2.1 (continued)

Name of chemicals/reagents	Company
Calcium standard stock solution 1000 ppm	Merck (Darmstadt, Germany)
Chitosan from crab shells	Sigma-Aldrich Corporation (St. Louis, MO, USA)
Di-ammonium hydrogen phosphate ($(NH_4)_2HPO_4$)	Sigma-Aldrich Corporation (St. Louis, MO, USA)
Di-sodium hydrogen phosphate (Na_2HPO_4)	Sigma-Aldrich Corporation (St. Louis, MO, USA)
Dimethyl sulfoxide (DMSO)	Sigma-Aldrich Corporation (St. Louis, MO, USA)
Dulbecco's Modified Eagle's Medium (DMEM)	Gibco™ Invitrogen Corporation (Grand Island, NY, USA)
Dulbecco's modified Eagle's medium-F12 (DMEM/F12)	Gibco™ Invitrogen Corporation (Grand Island, NY, USA)
Dulbecco's phosphate buffer saline (DPBS)	Gibco™ Invitrogen Corporation (Grand Island, NY, USA)
Ethylenediamine tetra-acetic acid (EDTA)	Ajax Finechem Pty. Ltd. (Australia)
Eosin Y solution	Sigma-Aldrich Corporation (St. Louis, MO, USA)
Ethanol	Merck (Darmstadt, Germany)
Fetal bovine serum (FBS)	Gibco (Karsruhe, Germany)
Formalin	Sigma-Aldrich Corporation (St. Louis, MO, USA)
Glutaraldehyde (25%)	Sigma-Aldrich Corporation (St. Louis, MO, USA)
Hydroxyapatite (HA)	Fluka (Buchs, Switzerland)
Heparin	Sigma-Aldrich Corporation (St. Louis, MO, USA)
Hydrochloric acid (HCl)	Merck (Darmstadt, Germany)
Mayer's hematoxylin solution	Sigma-Aldrich Corporation (St. Louis, MO, USA)
Methicillin-resistant *Staphylococcus aureus* BAA 1680	American Type Culture Collection (Manassas, VA, USA)

Table 2.1 (continued)

Name of chemicals/reagents	Company
N-(3-dimethylaminopropyl)-*N*/-ethylcarbodiimide hydrochloride (EDC)	Sigma (Chicago, Illinois)
N-hydroxysuccinimide (NHS)	Sigma (Chicago, Illinois)
Nitric acid (HNO_3)	Jt Barker (USA)
O-cresolphthalein complexone	Sigma-Aldrich Corporation (St. Louis, MO, USA)
Paraformaldehyde	Sigma-Aldrich corporation (St. Louis, MO, USA)
Potassium bromide (KBr)	Sigma-Aldrich Corporation (St. Louis, MO, USA)
Potassium dihydrogen phosphate (KH_2PO)	Merck (Darmstadt, Germany)
Potassium choride (KCl)	Sigma-Aldrich corporation (St. Louis, MO, USA)
Recombinant human bone morphogenetic protein 2 (rhBMP2)	BioVision (Milpitas, CA, USA)
Sodium bicarbonate ($NaHCO_3$)	Sigma-Aldrich Corporation (St. Louis, MO, USA)
Sodium carbonate (Na_2CO_3)	Sigma-Aldrich Corporation (St. Louis, MO, USA)
Sodium chloride (NaCl)	Lab-Scan Co., Ltd. (Bangkok, Thailand)
Sodium sulphate (Na_2SO_4)	Sigma-Aldrich Corporation (St. Louis, MO, USA)
Sodium tripolyphosphate (TPP)	Sigma-Aldrich Corporation (St. Louis, MO, USA)
Sulfuric acid (H_2SO_4)	Merck (Darmstadt, Germany)
Toluidine blue O	Sigma-Aldrich Corporation (St. Louis, MO, USA)
Tri-sodium citrate dihydrate	Sigma-Aldrich Corporation (St. Louis, MO, USA)
Trypsin-EDTA (10X)	Gibco™ Invitrogen Corporation (Grand Island, NY, USA)
Tryptone soy broth (TSB)	Oxoid Ltd. (Basingstoke, Hampshire, England)

Table 2.1 (continued)

Name of chemicals/reagents	Company
Vancomycin	Injectable vancomycin, Alkem Laboratories Ltd. (India); Vancomycin hydrochloride standard (Toku-E, Bellingham, WA)
Xylazine	Thai Nakorn Patana (Nonthaburi, Thailand)
Xylene	RCI Labscan Limited (Bangkok, Thailand)
Zinc chloride	Sigma-Aldrich Corporation (St. Louis, MO, USA)
Zoletil	Virbac Pty Limited (Australia)

Table 2.2 Equipments and the corresponding models and owners

Equipment/Instrument	**Model/Company**
Analytical balances	300A (max 350 g, min 0.01 g), Precisa (Switzerland); T-203 (max 200 g, min 0.001 g), Denver Instrument (Germany)
Aspirator	Flask-trap Aspirator FTA-1, Biosan (Latvia)
Autoclave	SA-300VF-F-A500, Sturdy (Taiwan)
Ball mill machine	HSM 100H, HERZOG (Germany)
Centrifuges	Allergra® X-15R, Beckman Coulter (CA, USA); Z383K, Hermle (Germany); Universal 16R, Hettich Lab Technology (Germamy); VS-15000N, Vision (Korea); Centrifuge CF-5, Daihan Scientific (Korea)
CO_2 incubator	2323-2, Shel Lab (OR, USA); 3111, Thermoscientific (MA, USA)
Fluorescent Microscope	BX61 Motorized System Microscope, Olympus (Japan)
Fourier Transform Infrared Spectrophotometer (FTIR)	Perkin-Elmer, Massachusetts (USA)
Freeze Dryer	FD8-5503, OPERON (Gyneonggi-do, Korea)
Furnace	Abb Furnace Co., Ltd (Thailand)
Hot air oven	Schutzart DIN 40050-IP20, Memmert (Germany)
Hot plate and magnetic stirrer	C-MAG HS7, IKA® (Malaysia)
Laminar air flow cabinet	Ultrasafe 48, Faster S.r.l (Italy); Aristream class II BSC, Esco Technologies, Inc (PA, USA)
Light Microscope	CK2, Olympus (Japan)
Macropipette	Acura® Manual 835 1-10 ml, Socorex (Switzerland)

Table 2.2 (continued)

Equipment/Instrument	Model/Company
Micropipettes	Labnet: 0.1-2.5 µl, and 0.5-10 µl (NY, USA)
	Biohit: 0.5-10 µl, 5-50 µl, and 10-100 µl (Finland)
	Pipet-Lite XLS 100-1,000 µl, Rainin (OH, USA)
Microplate Reader	PowerWaveX, BIOTEK instruments Inc (USA);
	DTX 880 Multimode Detector, Beckman Coulter (Austria)
Microwave oven	NN-NX21WX, Panasonic (Thailand)
Orbital shaker	Mini Shaker PSU-2T, Biosan (Latvia)
pH meter	Mettler Toledo (Switzerland)
Pipette Motorized Controller	PipetteBoy Pro, Integra (Switzerland);
	Pipet-aid, Drummond (PA, USA)
Power supply	EC 105 LVD, E-C Apparatus Corporation (CT, USA)
Refrigerator	Tiara (4 °C and -20 °C), Mitsubishi (Thailand);
	Low Temperature Freezer (-40°C), Haier (Thailand);
	SCL510 Scanlaf UTL Freezer (-80 °C), Labogene (Denmark)
Scanning electron microscope (SEM)	JSM-5800LV, JEOL (Japan);
	Quanta400, FEI (Brno, Czech Republic)
Shaker	Rocker platform, Bellco Biotechnology (NJ, USA)
Shacking incubator	VS-8480S, Vision Scientific CO., LTD (Korea)
Spectrophotometer	Diode Array Spectrophotometer 8452A, Hewlett Packard (CA, USA)
Thermogravimetric analyzer (TGA)	Perkin Elmer TGA7, Cooperate Headquarters (MS, USA)
X-ray diffractometer (XRD)	XRD, PHILIPS X'Pert MPD (Almelo, The Netherlands)

Table 2.2 (continued)

Equipment/Instrument	**Model/Company**
X-ray fluorescence spectrometer (XRF)	PW 2400, PHILIPS PANalytical (Almelo, The Netherlands)
Vortex	Vortex-Genie 2 G-560E, Scientific Industries (NY, USA)
Zeta Potential Analyzer	Zetasizer, Nano ZS, Malvern Instruments (Herrenberg, Germany)

2.2 Part I: Preparation of Si−nHA powders

2.2.1 Synthesis of Si−nHA powders

Silicon-substituted nano-hydroxyapatite (Si−nHA) powders were synthesized by using the wet chemical precipitation method. Two different groups of the materials were prepared, called the control HA and the synthesized HA group, respectively. Five mole ratios between the mole of $CaSiO_3$ and that of HA were designed for the preparation, as detailed in Table 2.3.

Table 2.3 The groups of synthesized Si−nHA powders and the designed mole ratios of $CaSiO_3$ to HA

Sample name	**Starting materials**		
	$(Ca(NO_3)_2.4H_2O/(NH_4)_2HPO_4$ (10:6, Mole Ratio)	**HA (Fluka) 1 mol**	**$CaSiO_3$ Mole Ratio to nHA**
Synthesized group			
0.1Si–synHA	+	–	0.1
0.2Si–synHA	+	–	0.2
0.3Si–synHA	+	–	0.3
0.4Si–synHA	+	–	0.4
0.5Si–synHA	+	–	0.5
Control group			
0.1Si–contHA	–	+	0.1
0.2Si–contHA	–	+	0.2
0.3Si–contHA	–	+	0.3
0.4Si–contHA	–	+	0.4
0.5Si–contHA	–	+	0.5

Symbol: +; used and –; non-used as starting material

To obtain silicon-substituted nano-hydroxyapatite (Si–nHA) powders, the wet chemical method was applied by modifying from Swain 2002 [189] as follow. In the synthesized group, a 100 mL of $(NH_4)_2HPO_4$ solution (0.6 M) and a 100 mL of $Ca(NO_3)_2.4H_2O$ (1.0 M) were prepared in distilled water. The solution of $Ca(NO_3)_2.4H_2O$ was transferred to a reaction flask under constant stirring at 65 °C. The $(NH_4)_2HPO_4$ solution was gradually added drop-wise into the $Ca(NO_3)_2.4H_2O$ solution. The chemical reaction was further stirred and maintained at 65 °C for 1 hour. The resulting turbid suspension of 1 mole nHA was acquired. After that $CaSiO_3$ powders at a different mole ratio ranging between 0.1 and 0.5 was added into the suspension, and continuously agitated at room temperature for 1 hour. Subsequently, the concentrated nitric acid (Jt Barker, USA) was gradually added until a clear solution was apparent. To generate Si–nHA particles, the pH of solution was adjusted to 10.4 by the addition of 25% ammonia solution (Loba Chemie Pvt. Ltd., India). The Si–nHA suspension was agitated further for overnight, and then washed with distilled water until the flow through was neutral. The white precipitation of Si−nHA was collected by vacuum filtration using Buchner funnel, filtered and dried in an oven at 60 °C for 3 days. The dried powder was calcinated at 1250 °C for 2 hours. In the control group, the commercial HA powder (Fluka, Buchs, Switzerland) was used instead of $Ca(NO_3)_2.4H_2O$ and $(NH_4)_2HPO_4$ for the first precipitation reaction. The following procedures were done in similar ways to those described above. Summation of the synthesis procedures was schematically shown in Figure 2.2.

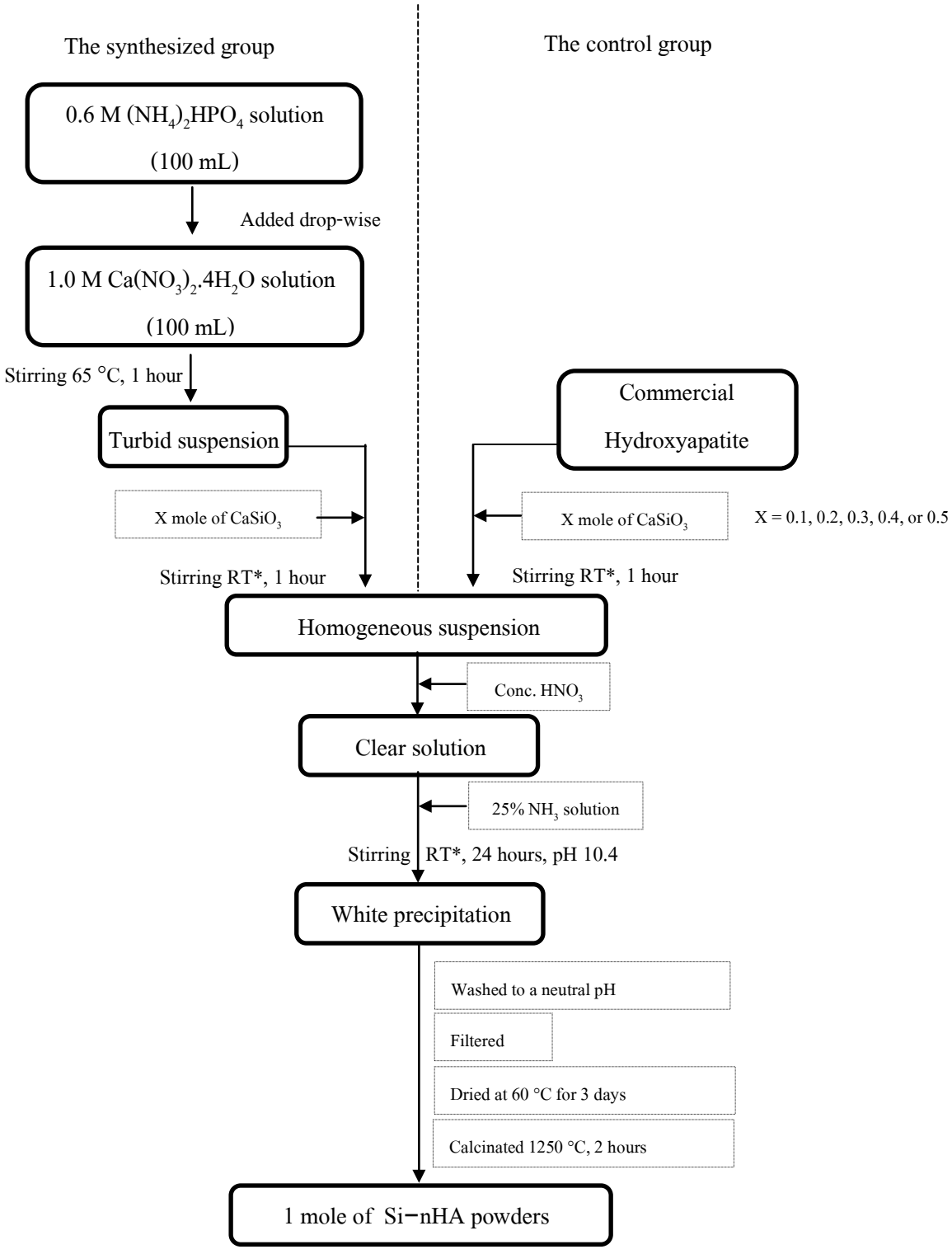

*RT: room temperature

Figure 2.2 The procedures for preparing silicon–substituted nano–hydroxyapatite (Si–nHA) powders by the wet chemical precipitated method

The chemical reaction:

$$10Ca(NO_3)_2\,4H_2O + 6(NH_4)_2HPO_4 + 8NH_4OH \longrightarrow Ca_{10}(PO_4)_6(OH)_2 + 20NH_4NO_3 + 20H_2O$$

The possible substitution reaction of Si into HA lattice:

$$Ca_{10}(PO_4)_6(OH)_2 + xSiO_4^{4-} \longrightarrow Ca_{10}(PO_4)_{6-x}(SiO_4)_x(OH)_{2-x} + xPO_4^{3-} + xOH^-$$

Where x was the numbers of the mole of silicate species introduced into HA structure.

2.2.2 Induction of forming apatite layer on Si–nHA powders

Apatite layer was inducted to form by immersing 5 g of Si–nHA powders in 20 mL of phosphate buffered saline (PBS) solution for 14 days. After that, the soaked powders were washed 5 times with distilled water and dried in an oven at 60 °C for 3 days. The obtained powders were ground to produce a fine particulate product using a ball mill machine (HSM 100H, HERZOG, Germany). The ground materials were used for further experiments.

2.3 Part II: Physical characterizations

2.3.1 X-ray diffraction (XRD)

The as-prepared Si-nHA powders were evaluated by X-ray diffractometer (XRD, PHILIPS X'Pert MPD; Almelo, The Netherlands) for crystallinity and phrase identification under exposure to CuKα radiation. A diffraction-2θ range from 5.0–90.0° was scanned with incident angle of 0.2° at an increasing rate of 2.4° per minute. The resulting diffraction patterns were identified by comparing with JCPDS reference files.

2.3.2 X-ray fluorescence (XRF)

The content of calcium, phosphorus, and silicon ions in Si–nHA powders were determined by X-ray fluorescence (XRF) spectrometric technique using an analytical Philips PW2400 X-ray spectrometer (PANalytical; Almelo, The Netherlands) equipped with a Rhodium anode X-ray tube. The elemental analysis was performed by using X-rays to excite fluorescent radiation from the sample at regular incidence with the unfiltered, uncollimated radiation operated at 3 kW. The emission angle was operated at the angle's measurement range from 0 to 100 mrad (0-6°) by means of rotatable sample-holders. Semi-quantitative experiments were evaluated in a vacuum chamber of approximately 1 Pa to prevent artifacts from X-ray absorption of longer wavelengths by air.

2.3.3 Fourier transform infrared spectroscopy (FTIR)

Both the synthesized and the control Si–nHA powders were subjected to do FTIR (Perkin-Elmer, Massachusetts, USA) using transmittance mode. All samples were mixed and ground with potassium bromide (KBr) to prepare a simple disc. A polystyrene filter was used for calibrating the spectrometer. The spectra range from 450 to 4400 cm^{-1} of the sample was recorded at resolution of 4 cm^{-1} and 16 times scans.

2.3.4 Scanning electron microscopy (SEM)

The micro-morphology of the synthesized and the control Si-nHA samples were observed using scanning electron microscopy system (SEM; Quanta 400; FEI, Brno, Czech Republic). The sample was mold on the metal stubs using a double-sided adhesive tape and then the surface of samples was sputtered using the direct current sputtering techniques with a gold thin film and observed by SEM with the accelerated voltage of 15 kV.

2.3.5 Thermo-gravimetric analysis (TGA)

Thermo-gravimetric analysis was used to monitor weight loss and thermal behavior of the as-prepared materials. All samples were investigated by a Perkin Elmer TGA7 (Cooperate Headquarters, MS, USA). Ten milligrams of a sample were performed in each measurement in the balance system and heated from ambient temperature to 1350 °C. The increasing rate was 10 °C per minute with a nitrogen flow to avoid thermo-oxidative reactions.

2.3.6 Zeta potential (ζ)

The zeta potential measurement (ζ) was performed at 25±0.5 °C with a Zetasizer (Nano ZS, Malvern Instruments; Herrenberg, Germany). The Si-nHA powders (2 g) before and after immersing in PBS for 14 days were suspended in 10 mL of 0.05 M carbonate buffer at different pH (6, 7 and 8) to obtained colloids of nano-particles. After centrifugation (2000 rpm, 5 minutes) the supernatant medium was collected. The ζ was estimated from the electrophoretic mobility by using Helmholtz-Smoluchowski equation [190].

2.4 Part III: Preparation of drug–free scaffolds

2.4.1 Fabrication of porous scaffolds

To generate porous Si–nHA scaffolds, 1 mL of chitosan solution (1.5% w/v in 3% acetic acid) was blended with 5 g of Si–nHA powders. The resulting smooth paste was obtained and then packed in a tube with 5 mm diameter and 5 mm height. The packed tube was allowed to rigidify at ambient temperature for 30 minutes, and submerged into the solution of sodium tripolyphosphate (TPP, 1% w/v) overnight. The harden scaffolds were extensively rinsed with distilled water to remove any excessive TPP. Finally, the scaffolds were dried by freeze-drying and stored at –20 °C until use.

2.4.2 Evaluation of drug–free scaffolds *in vitro*

2.4.2.1 The release of Ca^{2+} ions

Ortho-Cresolphthalein Complexone (OCPC) procedure was used for colorimetric estimation of calcium released from scaffold sample. The method is based on calcium ions (Ca^{2+}) reacting with o-cresolphthalein complexone in an alkaline medium to form a purple-colored complex. Furthermore, 8-Hydroxyquinoline (HQ) is added to remove interference by other ions. The absorbance of the Ca^{2+}–OCPC complex is measured spectroscopically at 570 nm. The resulting increase in the absorbance is directly proportional to the calcium concentration in the sample. Accordingly, 80 µL of color reagent (0.11 mM o-cresolphthalein complexone (OCPC), and 17.0 mM hydroxyquinoline (HQ) in water) and 80 µL of buffer solution pH 10.7 (0.98 M 2-amino-2-methyl-1-propanol (AMP) in water) were mixed in a well of a 96-well plate and allowed to stand for 20 minutes at room temperature before use. Then, the test solutions (40 µL each) were separately added to the respective wells of the mixed reagent with agitation. The absorbance of Ca^{2+}–OCPC complexes was then measured at 570 nm.

2.4.2.2 The release of PO_4^{3-} ions

To determinate phosphate ions (PO_4^{3-}) concentration released from scaffolds, a colorimetric assay method was carried out with some modifications. Briefly, the freshly prepared solutions of 2.5% w/v ammonium molybdate, 10% w/v ascorbic acid, and 3 M sulfuric acid in water were mixed with the respective volume ratio of 1:1:1 in 2 volumes of water for obtaining the complete reagent. At each sampling time period (4, 8, 16, 24, 32, 48 hours and 3, 5, 8, 12, 15, 20, 25 and 30 days (n=3), a 100-µL aliquot of the elution medium was analyzed by mixing with an equal volume of the reagent. After incubation for 1.5 hours at 37±0.5 °C, the absorbance at a wavelength of 820 nm was measured, using a microplate reader (PowerWaveX, BIOTEX instruments Inc, USA). The experiment was done in triplicate. To draw a standard curve, the solutions of known concentrations of PO_4^{3-} that range between 1 and 200 µM were performed in parallel. The measured data were calculated for the PO_4^{3-} concentrations by comparing with the standard curve.

2.4.2.3 *In vitro* biodegradation test

In *in vitro* biodegradation study, scaffolds were immersed in PBS for different time periods of 4, 8, 16, 24, 32, 48 hours and 3, 5, 8, 12, 15, 20, 25 and 30 days (n=3). The immersed samples were washed with distilled water and then dried in an oven at 60±0.5 °C before weighing. The percentage of weight loss was calculated by the equation below:

$$\text{Weight loss (\%)} = \{(W_O - W_t)/W_O\} \times 100$$

Where W_O was the initial mass of the scaffold and W_t was the mass of the dried scaffolds after immersion at time t.

2.4.2.4 Protein adsorption on drug–free scaffolds

The adsorption of proteins onto the scaffold surfaces was assessed by SEM (Quanta 400; FEI, Brno, Czech Republic). Dulbecco's Modified Eagle's Medium (DMEM) (Gibco, Grand Island, NY, USA) containing 6% v/v fetal bovine serum (Gibco) was used as the complex protein solution for protein adsorption test. Scaffolds were sterilized by soaking in ethanol (70%) for 24 hours, washed several times with serum-free medium (SFM), and equilibrated in SFM for 30 minutes before use. Subsequently, the sterilized scaffolds were incubated with the protein solution for 1 and 3 days. After washing twice with PBS, the tested scaffold were fixed using serially diluted ethanol solutions, i.e., 30, 50, 70, and 95%, each for 10 minutes. The fixed samples were microscopically observed using SEM (Quanta 400; FEI, Brno, Czech Republic)

2.5 Part IV: Loading of VCM and rhBMP2

2.5.1 Vancomycin–containing Si–nHA scaffolds

2.5.1.1 Drug loading

Injectable vancomycin (VCM) hydrochloride (0.5 g/vial; Alkem Laboratories Ltd; India) was used for loading into scaffolds. VCM solutions of two different concentrations (5, and 100 mg/mL) were prepared using water as the solvent. Drug-free scaffolds were separately immersed in a VCM solution at 4 °C for 24 hours. The ratio between solid and liquid phases was set at 1 g/mL. After that the soaked scaffolds were removed and rapidly washed with 1 mL distilled water to remove the unattached drug. The amount of drug loaded in the scaffolds was carried out by determining the concentration of VCM remaining in the solution after the immersion.

2.5.1.2 The Entrapment Efficiency (%EE)

VCM loading capacity was calculated by measuring the amount of drug in the solution before and after the immersion at 280 nm using spectrophotometer. The experiment was done in triplicate and the %EE was calculated according to the equation below:

$$\%EE = (A_O - A_S)/(A_S) \times 100$$

Where A_O was the initial amount of VCM in the solution, and A_S was the amount of VCM remaining in the solution after the immersion.

2.5.1.3 *In vitro* release

To determine the amount of VCM released from the scaffolds, each of them (approximately 200 mg/scaffold) was incubated in a vial containing 1 mL of PBS (pH 7.4 at 37±0.5 °C). The ratio between solid and liquid phases was fixed at 200 mg per 1 mL. At a designed time period (4, 8, 16, 24, 32, and 48 hours and 3, 5, 8, or 12 days), the supernatant was withdrawn for quantifying VCM released by measuring the optical density at 280 nm using a UV–visible spectrophotometer (Hewlett Packard, Massachusetts, USA). VCM standard solutions at concentrations ranging between 0.2 and 15 μg/mL were performed to create the corresponding calibration curve. The supernatant of drug-free scaffolds was used as the blank to minimize any potential interference from Ca^{2+} and PO_4^{3-} ions in preparing the calibration baselines.

2.5.1.4 Antimicrobial activity of VCM−loaded scaffolds

The broth dilution technique was used to determine antimicrobial activity of VCM–loaded scaffolds, as follows. Methicillin resistant *Staphylococcus aureus* (MRSA) strain BAA–1680 from American Type Culture Collection (Manassas, VA, USA) frozen culture was rapidly thawed and cultivated on a tryptone soy agar plate at 37±0.5 °C overnight. The colonies of

the bacterium were separately suspended in 5 mL tryptone soy broth and grown overnight at 37 °C. The test bacterial suspension was manipulated by diluting the overnight culture in the broth medium to obtain turbidity of 0.5 McFarland, which corresponded roughly to $1–2\times10^{8}$ CFU/mL, before use.

The assay was in according to the guidelines of the National Committee for Clinical Laboratory Standards. Briefly, a 100 µL volume of the drug solution was pipetted into the first well. A 50 µL from the first well was taken and added into the second well that contained 50 µL of the culture medium. This two-fold dilution procedure was performed as indicated in Figure 2.3.

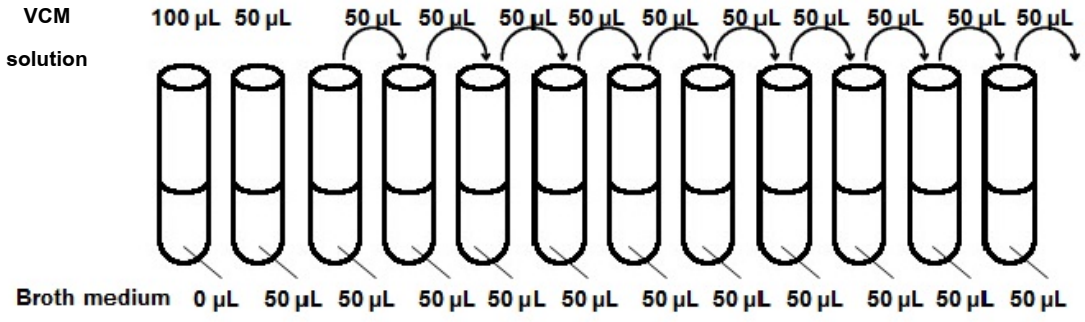

Figure 2.3 Preparation of two-fold dilutions for test samples

Fifty µL of the test bacterial suspension were inoculated into each well of the two-fold serially diluted test solutions. After incubated overnight at 37±0.5 °C, the turbidity of the growing bacterial suspension was measured at 590 nm using a microplate reader (PowerWaveX, BIOTEX instruments Inc, USA). The experiments using standard VCM solutions were carried out in parallel. The half maximal effective concentration (EC_{50}), which is the concentration of the drug showing growth inhibition of the test bacterium by 50%, was evaluated. Each experiment was done in triplicate, and the antibacterial activity of the drug–loaded scaffolds was calculated as the percentage inhibition using following formula.

$$\% \text{ inhibition} = \{1 - (A_t - A_b)/ A_c - A_b)\} \times 100$$

Where A_t, A_b and A_c were the turbidity values of the test sample, the blank and the control, respectively.

2.5.1.5 Cytotoxicity of VCM−loaded scaffolds

To evaluate cytotoxicity of VCM-loaded scaffolds, the scaffold samples were incubated in PBS for 12 days at 37±0.5 °C with the fixed ratio between the solid and liquid phases of 200 mg/mL. The collected supernatant was sterilized by filtering through a sterile 0.22 μm membrane and diluted to 50% and 25% (v/v) by adding serum-free medium (SFM). This diluted supernatant was supplemented with 6% fetal bovine serum (FBS) before employed for assessing cytotoxicity. Rat osteoblast-like cells (ROBs) obtained from Miss Paweena Wongwitwichot at Prince of Songkla University were routinely cultured in Dulbecco's modified Eagle's medium-F12 (DMEM/F12) containing 6% FBS, 100 units penicillin G sodium, 100 mg streptomycin sulfate, 2% amphotericin B, and 2% L-glutamine, in a humidified atmosphere of 5% CO_2 at 37±0.5 °C. After confluence, the cells were harvested, counted and resuspended to a density of 1×10^5 cells/mL. A 100 μL cell suspension was seeded onto a well of 96-well plate, and incubated overnight at 37±0.5 °C to allow cell attachment. Then, the culture medium was carefully removed, and 100 μL of the prepared samples was separately placed to the well. Fresh culture medium was used as the blank control. The plate was incubated further for 24 hours in a CO_2 incubator at 37±0.5 °C, and evaluated for the cell viability using MTT assay. In brief, 100 μL of MTT (5 mg/mL) solution were separately added to each well after the medium was withdrawn and incubated further for 4 hours in a CO_2 incubator at 37±0.5 °C. At the end of the incubation, the excess reagent was carefully removed, and a 200 μL dimethylsulfoxide (DMSO) was added to each well to dissolve the purple formazan crystals. Optical densities of the formazan solutions were measured at a wavelength of 570 nm using a microplate reader (PowerWaveX, BIOTEX instruments Inc, USA).

2.5.2 Loading of rhBMP2 into scaffolds

2.5.2.1 Preparation of heparinized scaffolds

Chemicals used in the heparin conjugation process, including *N*-(3-dimethylaminopropyl)-*N*/-ethylcarbodiimide hydrochloride (EDC), *N*-hydroxysuccinimide (NHS), and 2-morpholinoethane sulfonic acid (MES) were purchased from Sigma (Chicago, Illinois). MES buffer was prepared by dissolving 0.433 g of EDC and 0.157 g of NHS in 188.3 mL water, and adjusted to pH 5.4. Heparin solutions were prepared by dissolving different amounts of heparin (Sigma) in MES buffer to a concentration of 0.5, 1, or 2% w/v. Scaffolds were activated by incubating in MES buffer for 30 minutes. The activated scaffolds were then immersed in the heparin solution and the mixture was evacuated at 200 Pa for approximately 30 seconds to remove air bubble. The conjugation reaction was carried out for 4 hours at 37±0.5 °C. After that the conjugated scaffolds were respectively washed with sodium chloride solutions of different concentrations, e.g., 2 M, 6 times for 4 hours; 4 M, 4 times for 6 hours, followed by with distilled water (3 times for 8 hours). Finally, the modified scaffolds were frozen at –40 °C overnight, lyophilized for 8 hours, and kept at 4 °C until use.

2.5.2.2 Characterization of the heparinized scaffolds

2.5.2.2.1 Toluidine blue staining

The amount of heparin cross-linked onto the scaffold surfaces was qualitatively determined using toluidine blue method with some modifications. In brief, a 0.4 mg/mL toluidine blue solution was prepared by dissolving 40 mg of toluidine blue zinc chloride double salt in 100 mL of 0.1 M hydrochloric acid containing 0.2% w/v NaCl. Subsequently, 2 g of the heparinized scaffold were added into 1 mL of the staining solution, and gently agitated with a vortex mixer for 4 hours at room temperature. The excess dye solution was removed by using a filter paper. This was followed by washing the scaffold with distilled water (two times for 5

minutes) and air dried. The intensity of dye stained onto the surface was investigated using a camera.

2.5.2.2.2 Stability and blood compatibility

In vitro tests for stability and blood compatibility were carried out by investigating the aggregation of platelets. Platelet-rich plasma (PRP) was prepared by mixing 1 volume of native whole blood from normal healthy pig in a plastic tube containing 9 volumes of 3.8% w/v tri-sodium citrate solution. After centrifugation, the jelly complex was collected to gain PRP. The heparinized scaffold was rinsed with PBS and submerged in PRP for 3 hours at 37 °C, allowing interactions between PRP and the scaffold to take place. Subsequently, the scaffold was repeatedly washed with PBS to remove the un-adhered platelets, and then fixed with 2.5% v/v glutaraldehyde in PBS for 2 hours. The fixed scaffold was washed again in PBS and dehydrated using a series of ethanol-water mixtures (30, 40, 50, 60, 70, 80, 90, and 100% v/v). After drying in vacuum at 25 °C for 24 hours, the scaffold was examined using SEM. At the first time of rinsing the scaffold in PBS, the rinsed solution was collected for clotting assay by incubating it with PRP for 30 minutes at 37±0.5 °C under static conditions. The clotting appearance was observed by eyes and recorded as + or – for clotted or un-clotted status of the PRP, respectively.

2.5.2.3 Loading of rhBMP2 onto the heparinized scaffolds

Purified recombinant human BMP 2 (rhBMP2) was purchased from BioVision (Milpitas, CA, USA). One day before implantation, five grams of the heparinized scaffolds were immersed in 100 µL of diluted rhBMP2 solution (5 or 10 µg/mL), and incubated for 24 hours at 4 °C. The excess rhBMP2 solution was removed by placing them on a sterilized filter paper before using in animal experiments.

2.5.2.4 *In vivo* evaluation of rhBMP2 loaded scaffolds

2.5.2.4.1 Animals and surgical procedure

Two male 8-week-old Wistra rats (weight 220–250g) were used for subcutaneous implantation, according to an approved protocol by local animal care and use committee at Prince of Songkla University. Prior to surgery, the rats were anesthetized by intramuscular injection of the mixture of 25 mg/mL xylazine and 12.5 mg/mL zoletil at a 1:1 volume ratio with a 100-μL volume per 100 g body weight. After shaving and disinfecting, seven small pockets were created subcutaneously in the lumbar area. Each specimen measuring of 5 mm diameter and 3 mm thickness was inserted in the pocket. Due to the difference of the used concentrations for heparin (% w/v) and rhBMP2 (μg/mL), seven groups of the implant samples were classified (Table 2.4). Following implantation, the wounds were closed with 4-0 silk sutures. Topical antibiotic was given postoperatively to the rats for 1 week. They were sacrificed after 4 weeks to evaluate bone formation using histological analysis.

Table 2.4 Experimental design for the evolution of bone formation efficiency by subcutaneous implantation of scaffolds in rats

Group No. (n=2)	Scaffold sample	
	heparin (% w/v)	rhBMP2 (μg/mL)
1	0	0
2	0.5	0
3	0.5	5
4	0.5	10
5	1	0
6	1	5
7	1	10

2.6 Part V: *In vivo* evaluation of VCM/rhBMP2 containing scaffolds

2.6.1 Preparation of VCM/rhBMP2 containing scaffolds

Three groups of the scaffolds were designed (Figure 2.4). VCM and rhBMP2 at the respective concentrations of 100 mg/mL and 5 µg/mL were separately loaded onto a half of each scaffold by applying the previously established methods. The prepared implants were stored at 4 °C until use.

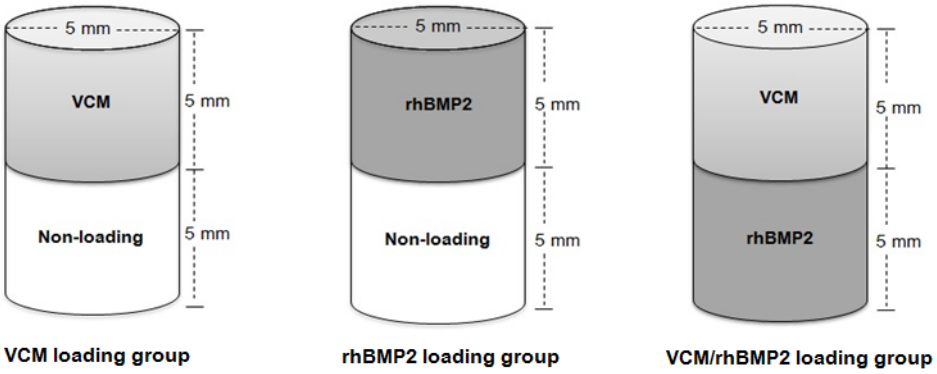

Figure 2.4 Schematic diagram of 3D-structure and dimension for three types of the scaffolds containing VCM, rhBMP2, or VCM plus rhBMP2

2.6.2 Osteomyelitis induction in rats

2.6.2.1 Preparation of bacterial cells

Methicillin-resistant *S. aureus* BAA 1680 strain was purchased from American Type Culture Collection (Manassas, VA, USA). From an overnight culture of a single colony in 5 mL tryptone soy broth (TSB; Oxoid Ltd., Basingstoke, Hampshire, England), portions of 100 µL were transferred into sterile tubes containing 3 mL of TSB and incubated for 3 hours at 37±0.5 °C to approach log-phase growth. After centrifugation (3000 rpm, 10 minutes), the supernatant was discarded and the bacterial cell pellet was washed twice with PBS. After that PBS

was added to the cell pellet until a McFarland standard of 0.5 was obtained. The bacterial suspension was continually diluted to the density of 10^5 CFU/mL, as confirmed by several plate counts.

2.6.2.2 Bacterial inoculation in rats

The ethics committee for animal studies of Prince of Songkla University had previously approved the animal experiment. Twenty healthy male Wistar rats weighing about 250-280 g were anesthetized intramuscularly with a 100-µL volume per 100 g body weight of the mixture containing a 1:1 volume ratio of xylazine (25 mg/mL) and zoletil (12.5 mg/mL). Their right hind legs were shaven and disinfected. A 100-µL bacterial suspension was loaded into the medullary cavity of tibia by injecting at epiphysis, followed by drilling the needle (gauge 23) through cortical and spongy bone until accessing the cavity [191]. The animals were kept in individual cages and followed up for clinical signs of infection, such as swelling and reddening of the right hind legs, and loss of passive motion in knee and ankle joints. After 4 and 12 weeks of inoculation, bacterial culture and X-ray method were performed to examine osteomyelitis appearance.

2.6.3 Implantation of VCM/rhBMP2 loading scaffolds in osteomyelitis rats

Rats which developed osteomyelitis after 4 weeks of inoculation were considered for this study. The 16 rats were randomly divided into 4 groups, the details of which were given in Table 2.5. Using aseptic technique, a 10-mm bone defect was created on the right tibia and replaced by individual implants without bone bridge installation. The animals were sacrificed 8 weeks post-implantation. Tissues from sites of osteomyelitis were excised for bacterial culture [192, 193]. All of the right tibias were extracted for X-ray examination, and then fixed in 10% v/v formaldehyde in PBS for 24 hours, decalcified in 3 M HCl, and paraffin imbedded. The paraffin blocks were sliced into 5-µm sections along the bone defects and stained with hematoxylin/eosin (HE) and alizarin red S (ARS) for light microscopic investigation.

Table 2.5 Design of the experiment for studying in osteomyelitis model

Groups	No. of animals	Implant	Experiment
Control	4	not given	Four rats were sacrificed for microbiological, radiographic and histological examinations to confirm the development of osteomyelitis.
V-group	4	Implants containing VCM	Four rats were sacrificed for histological and microbiological examinations.
B-group	4	Implants containing rhBMP2	Four rats were sacrificed for histological and microbiological examinations.
VB-group	4	Implants containing VCM and rhBMP2	Four rats were sacrificed for histological and microbiological examinations.

2.6.4 Histological analysis

The implants were excised and fixed with 10% v/v formaldehyde in PBS for 24 hours. Subsequently, the samples were decalcified for 2 days in 1.0 M HCl saturated with EDTA, and paraffin embedded. Histological sections of 5-μm thickness were stained with hematoxylin/eosin (HE) or alizarin red S (ARS) and observed under light microscope. Three different section levels and two histological sections for each level were analyzed for each sample.

2.7 Statistical Analysis

All quantitative data obtained in this study were presented as mean ± standard deviation (SD) using Statistics Package for Social Science (SPSS) software, ver. 19.0 (SPSS Inc., Chicago, USA). For *in vitro* experiments (n=3) and *in vivo* tibia bone experiments (n=4), the presence of significant differences between groups were indicated by using ANOVA (analysis of variance) and a Tukey HSD test for pairwise comparisons. A difference between groups was considered to be statistically significant as either *, $p < 0.05$ or **, $p < 0.01$. All histological measurements were made independently by two blinded observers.

CHAPTER 3

RESULTS

3.1 Part I: Preparation of Si–nHA powders

3.1.1 Synthesis of Si–nHA powders

In this experiment, the silicon substituted hydroxyapatite (Si–nHA) particles were successfully formed by using $Ca(NO_3)_2$ and $(NH_4)_2HPO_4$ as the starting materials. Trace amount of silicate ion was incorporated into the lattices of HA during the wet chemical precipitation reaction. The particles were taken to calcination at 1250 °C for 2 hours, and ground to obtain fine powders of nano-sized ranges (Figure 3.1). The uniformly distributed particles were demonstrated for Si–synHA (Figure 3.1b), whereas aggregates of fine particles with irregular shape and size were apparent for Si–contHA (Figure 3.1a).

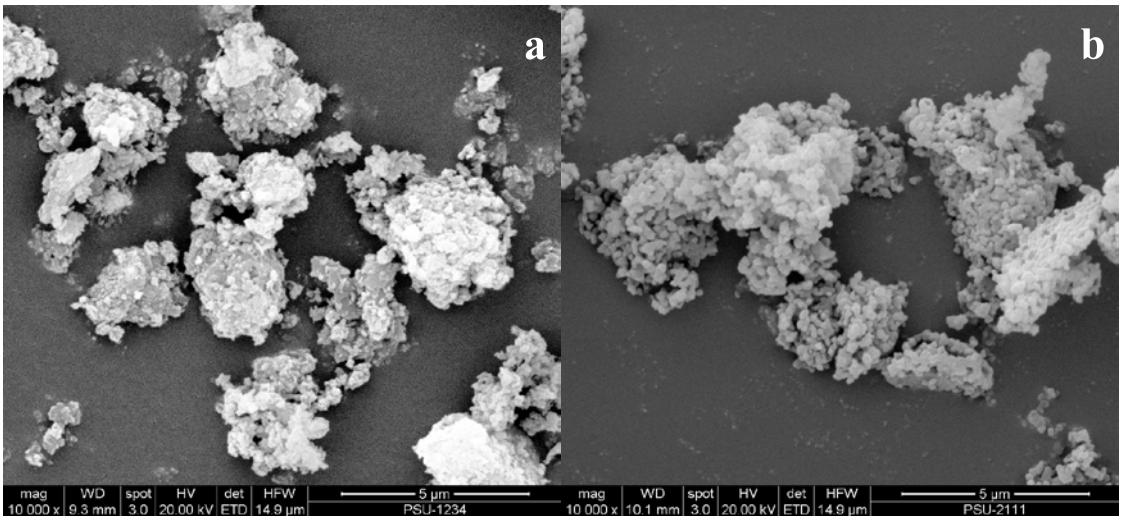

Figure 3.1 SEM images of silicon substituted hydroxyapatite (Si–nHA) pariticles prepared by the wet chemical precipitation reaction using (a) commercialized HA (Fluka), and (b) $Ca(NO_3)_2$ and $(NH_4)_2HPO_4$ as the starting materials in the first chemical reaction (see 2.2.1)

3.1.2 Apatite formation on the surfaces of Si–nHA particles

The as-synthesized Si–nHA powders were immersed in PBS pH 7.4 at 37 °C for 14 days to induce apatite formation. Apatite layers could be detected on the immersed surfaces (Figure 3.2). The amounts of apatite formed were greater for 0.3Si–nHA and 0.4Si–nHA particles (Figure 3.2b and c), compared to those incorporated by calcium silicate of $<$0.3 or $>$0.4 mole ratios (data not shown).

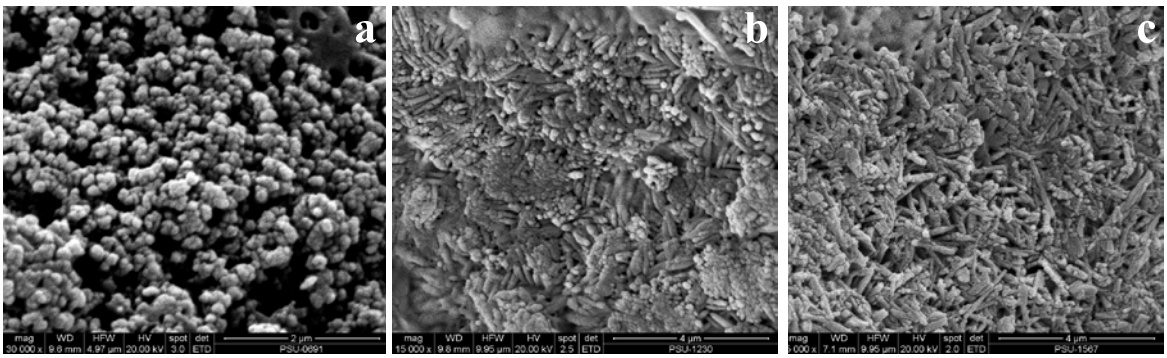

Figure 3.2 SEM images of apatite layer on the Si–nHA surfaces: a, Si–nHA before immersion; b and c, 0.3Si–nHA and 0.4Si–nHA after immersion in PBS pH 7.4 at 37 °C for 14 days, respectively

3.2 Part II: Physical characterizations

The techniques of X–ray diffraction analysis (XRD), X–ray fluorescence spectroscopy (XRF), Fourier transform infrared spectroscopy (FTIR), Scanning electron microscopy (SEM), Thermo-gravimetric analysis (TGA) and zeta potential (ζ) were used for physical characterizations of the prepared materials, as fallows.

3.2.1 X-ray diffraction analysis (XRD)

According to the results of apatite formation on the materials (Figure 3.2), the particles prepared by using 0.3 and 0.4 mole ratio of $CaSiO_3$ were chosen for XRD analysis. The XRD patterns were displayed in Figure 3.3. By comparing with the diffractograms of JCPDS reference, the phases of HA (09-0432), α– and β–TCP (09-0348 and 09-0169, respectively), OCP (26-1056), DCPD (01-072-0713), CaO (04-0777), and amorphous CaP were detected. After calcination at 1250 °C for 2 hours, the major phases of HA, α– and β–TCP were dominately appearent. In addition, the undesirable phase of calcium oxide (CaO) was formed upon the thermal treatment. The peaks' intensity of the control samples was changed significantly compared to those of the synthesized Si–nHA powders. The α–TCP characterized peaks gradually decreased as the immersion time in PBS increased, whereas those of β–TCP characterized peaks remained unchanged. The intensity of HA-characterized peaks increased evidently after 14 days of the immersion. Besides, the appearance of several extra peaks identified as dicalcium phosphatedehydrate (DCPD), octacalcium phosphate (OCP) and amorphous CaP forms were observed. All bioactive samples had the characteristic peaks which were broaden and weaker in intensities than those of the inactive ones (not immersed in PBS).

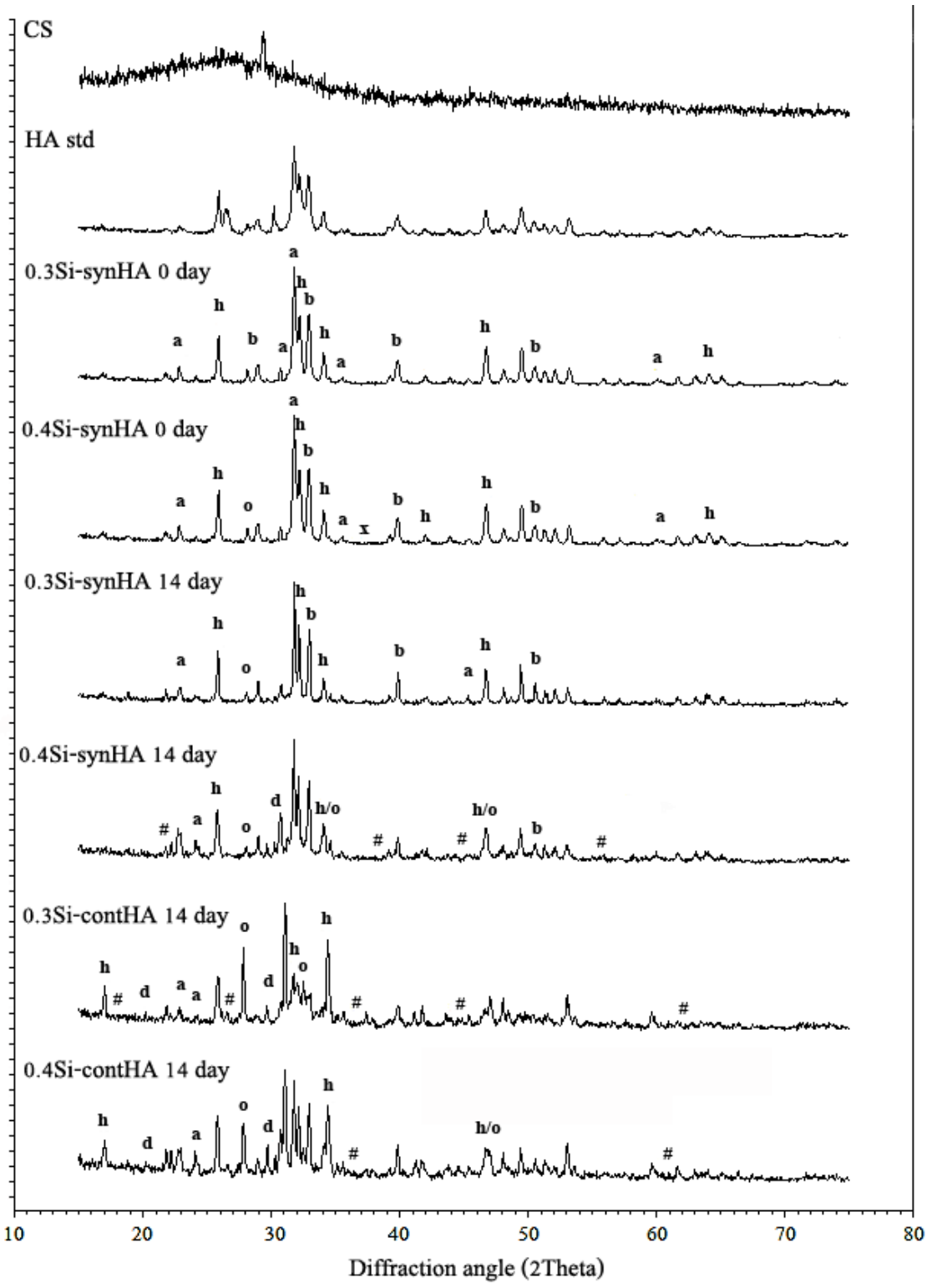

Figure 3.3 XRD patterns of Si–nHA powders after the synthesis (0 day) and of the 14–day soaking in PBS: Symbol: a, α–TCP; b, β–TCP; h, HA; o, OCP; d, DCPD; x, CaO and #, amorphus CaP

3.2.2 X-ray fluorescence spectroscopy (XRF)

XRF was used to investigate the Ca/P and Ca+P/Si stoichiometry, when 0.3 and 0.4 mole of $CaSiO_3$ was used for the synthesis. The results were summarized in Table 3.1. Before soaking in PBS, the Ca/P ratio for the Si–contHA particles was significantly higher than the theoretical ratio. Those of 0.3 and 0.4 substituted Si-nHA were much significantly highly than those mentioned previously. After the immersion in PBS, such the ratio for the control was not changed. In contract, the lowered Ca/P ratio was revealed for Si–synHA samples. For the (Ca+P)/Si ratio, it was increased following immersed in PBS.

Table 3.1 XRF results in different bioactive material including the theoretical and measured ratios of Ca/P and (Ca+P)/Si atomic

Material	**Theoretical ratio**		**Observed molar ratio in the prepared powders**			
			Before		**After**	
	Ca/P	(Ca+P)/Si	Ca/P	(Ca+P)/Si	Ca/P	(Ca+P)/Si
Cont nHA	1.67	–	2.45±0.02	–	2.44±0.03	–
Syn nHA	1.67	–	2.67±0.04	–	2.67±0.04	–
0.3Si-synHA	1.67	53.3	3.79±0.03	119.38±0.10	2.42±0.05	136.36±0.20
0.4Si-synHA	1.67	40.0	3.98±0.04	105.10±0.15	2.58±0.06	143.31±0.28

3.2.3 Fourier transform infrared spectroscopy (FTIR)

The FTIR spectra recorded between 4000 and 450 cm^{-1} were shown in Figure 3.4. The results of characteristic bands exhibited by the samples were summarized in Table 3.2. The sharp band at 3572 cm^{-1} was associated with O—H stretching of hydroxyl groups. Two broad bands at 3400 cm^{-1} and 1650 cm^{-1} were corresponded to the bands of absorbed moisture attributed to the presence of water. The small frizzy band around 2020 cm^{-1} was corresponded to OH stretching of O—P—OH bands. A broad band around 1000 cm^{-1} was assigned to asymmetric stretching (ν_3) of Si—O bonds. Expansion of this band was observed by increasing the mole fraction of calcium silicate in the chemical reaction (Figure 3.5). The IR spectra of 0.3 and 0.4Si–synHA samples indicated a triply degenerated P—O stretching band between 644 and 567 cm^{-1}, while both of 0.3 and 0.4Si–contHA powders represented a doublet of degenerated Si—O—P bending vibration at 604 and 546 cm^{-1}. Moreover, the band appearing at 470 cm^{-1} was assigned to Si—O—Si bending modes of SiO_4^{4-} groups. After soaking in PBS, the broad band of Si—O vibration gradually was disappeared, while the additional bonds at 1093 and 964 cm^{-1} belonging to P—O stretching bands became apparent (Figure 3.5 and Figure 3.6). Furthermore, the difficulty in detection of the bands relating to silicon substitution could be due to vibrational modes overlapping with the phosphate groups, which noted to occur in cases such as 470 cm^{-1} (Si—O—Si band) and 472 cm^{-1} (P—O—P). The bands in the region between 1650 and 1300 cm^{-1} were related to the occurrence of ν_3 vibration mode of CO_3^{2-} ions, which separated into two bands at 1649 and 1470 cm^{-1}.

Table 3.2 Characteristic bands of FTIR spectra for Si–nHA powders

IR frequency (cm^{-1})	**Assignments**	**References**
	Mode of OH^- group	
3572	ν_S, asymmetric stretching of OH groups	[110, 194]
2020	OH stretching of O=P—OH bonds	[195, 196]
	Mode of PO_4^{3-} group	
1093	ν_3, asymmetric stretching of P—O bonds	[194, 196]
964	ν_1, asymmetric stretching of P—O bonds	[110, 198]
~644-567	P—O stretching bonds	[110, 198, 199]
	Mode of CO_3^{2-} group	
1649, 1470	B-type CO_3^{2-} stretching	[110, 198]
	Mode of SiO_4^{4-} group	
1000	ν_3, asymmetric stretching Si—O bonds	[200, 201]
~800	Si—O vibration	[110, 202]
470	Si—O—Si bending	[202]
~604-546	Si—O—P bending vibration	[200, 201]

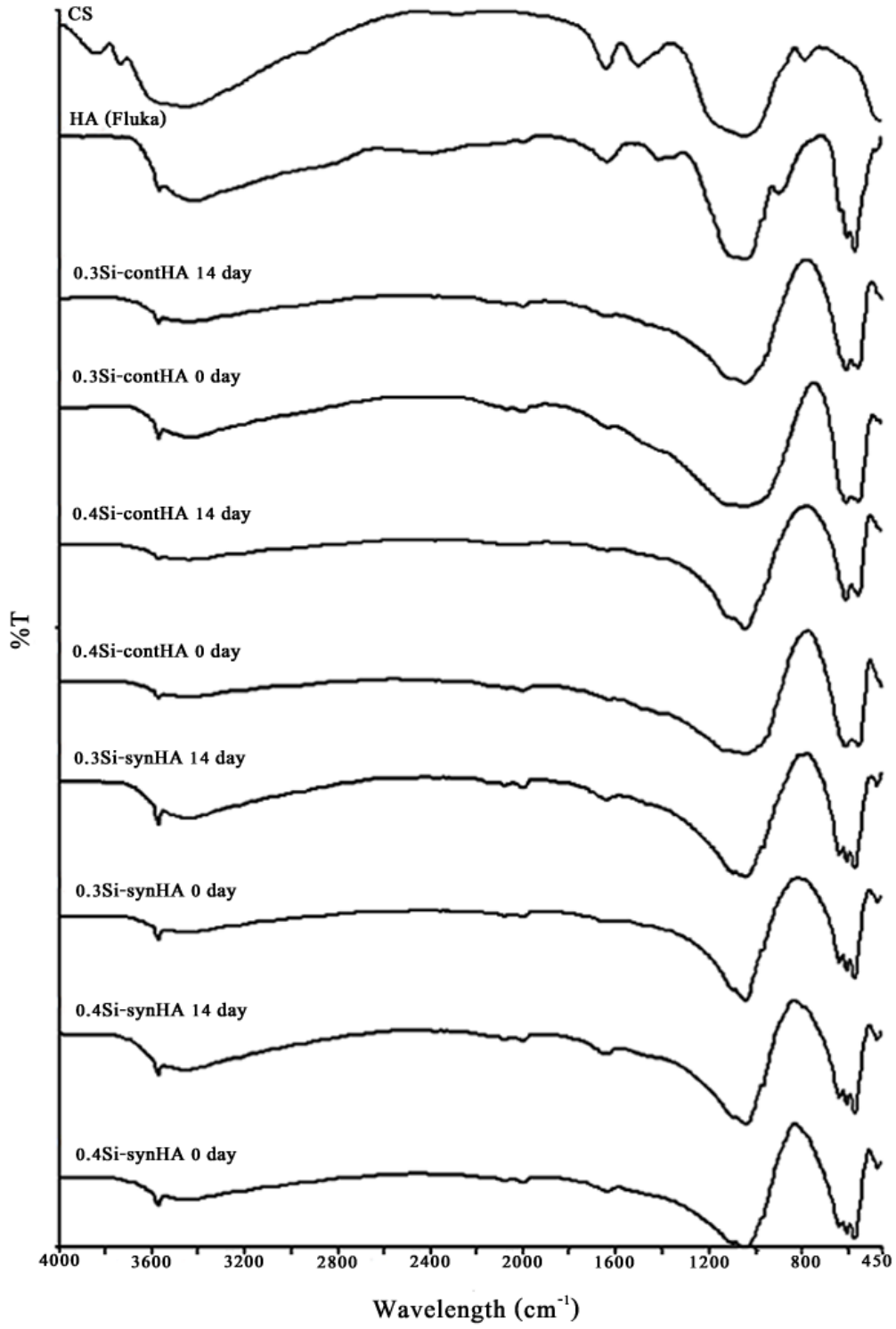

Figure 3.4 FTIR spectra of Si–nHA powders before (0 day) and after soaking in PBS for 14 days

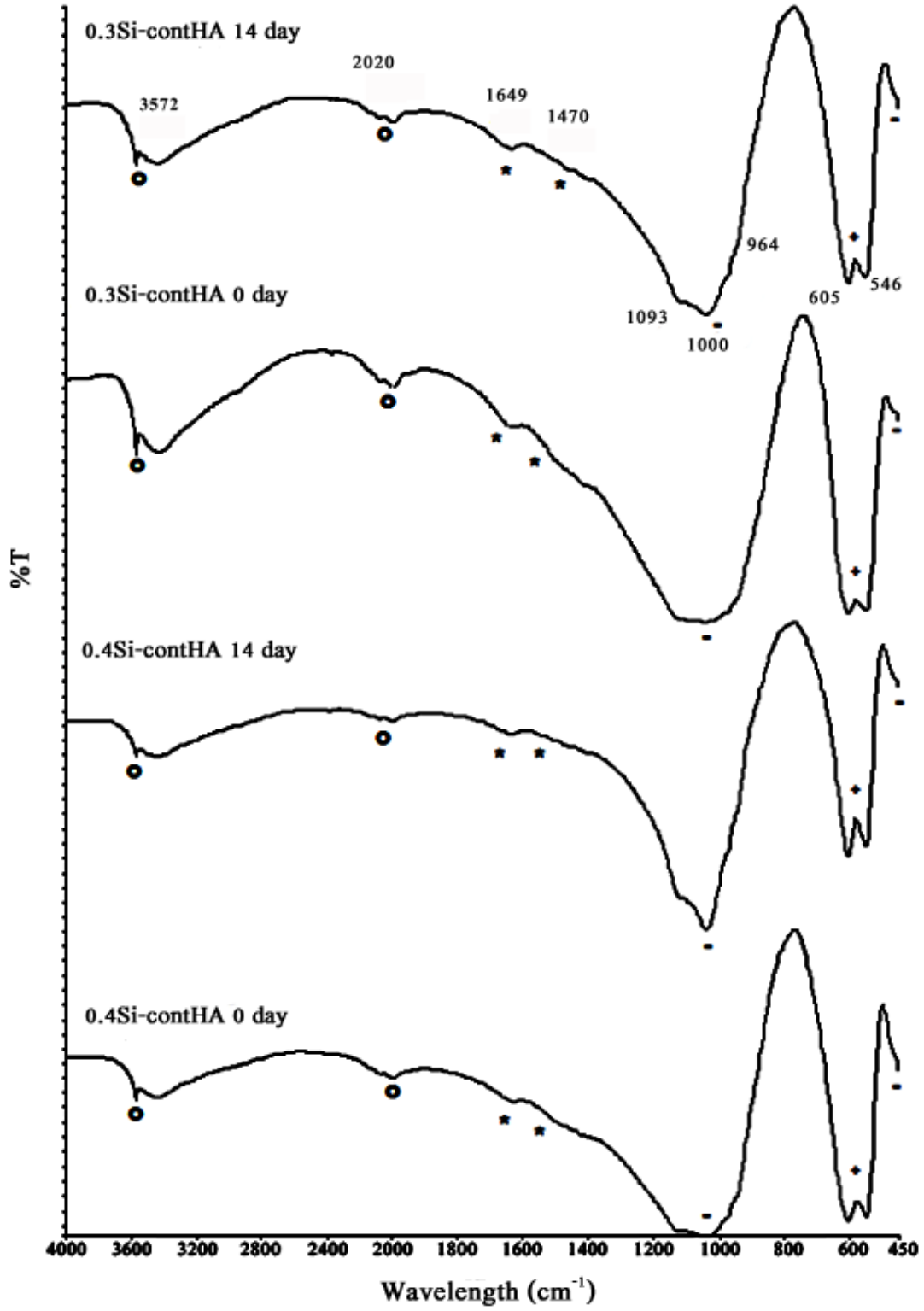

Figure 3.5 FTIR spectra of 0.3 and 0.4Si–contHA powders before (0 day) and after immersed in PBS for 14 days: Symbol: O = OH^- groups, * = CO_3^{2-} groups, + = PO_4^{3-} groups, ─ = SiO_4^{4-} groups

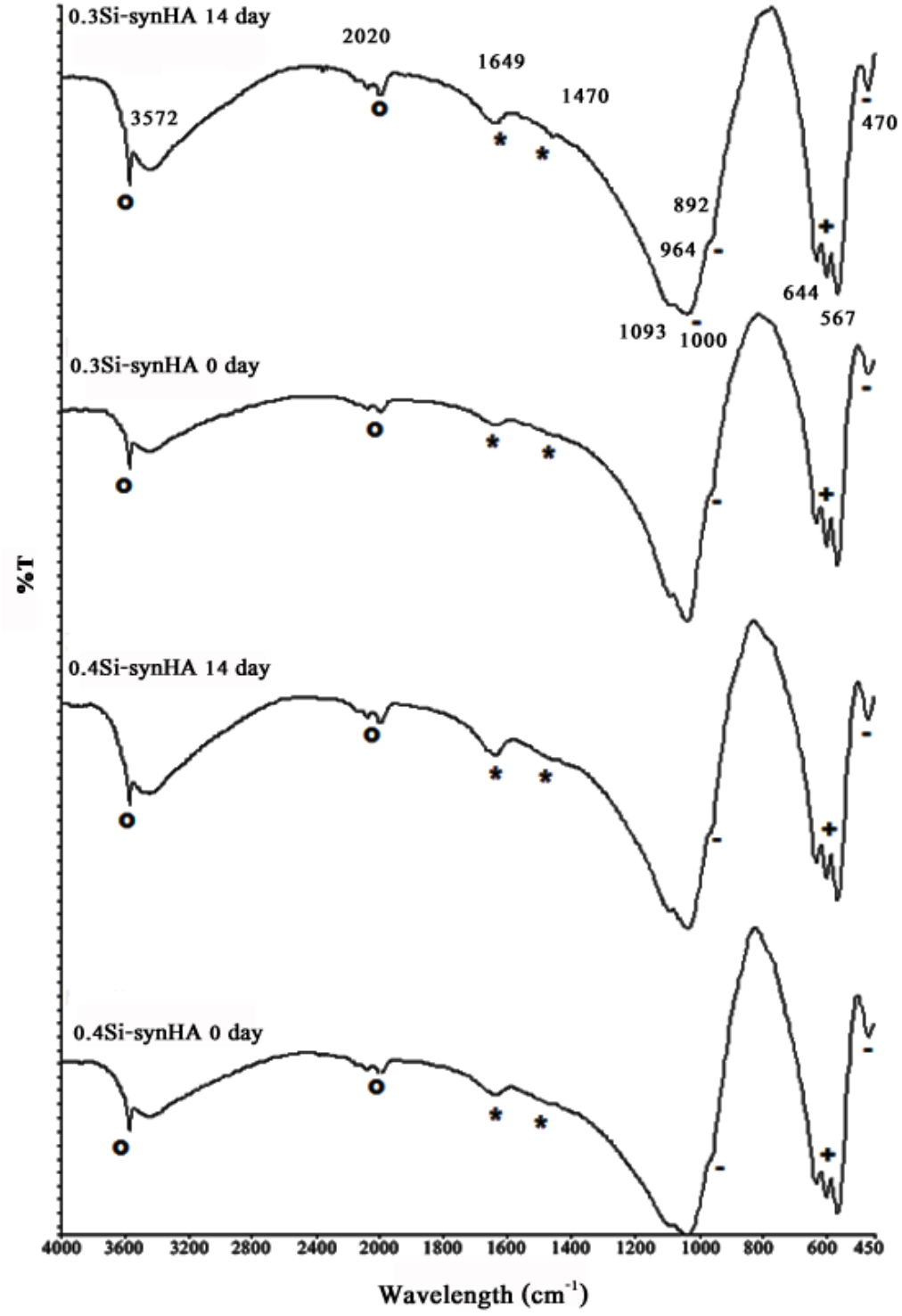

Figure 3.6 FTIR spectra of 0.3 and 0.4Si–synHA powders before (0 day) and after immersed in PBS for 14 days: Symbol: O = OH^- groups, * = CO_3^{2-} groups, + = PO_4^{3-} groups, ─ = SiO_4^{4-} groups

3.2.4 Scanning electron microscopy (SEM)

The SEM images of Si–nHA powders before and after immersed in PBS for 14 days were showed in Figure 3.7. Before the immersion, the Si-nHA powders were apperent as the fine particles of nano size ranges with irregular shape (Figure 3.7a). After the immersion, the apatite nucleation on the surface of Si–nHA particles were observed (Figure 3.7b-e). The change of their surfaces confirmed the deposition of apatite, apparing as the mat-like apatite layer on 0.3Si–nHA and 0.4Si–nHA surfaces. In contrast, Si–nHA powders of the before and the after immersion in PBS displayed distinct surface morphology.

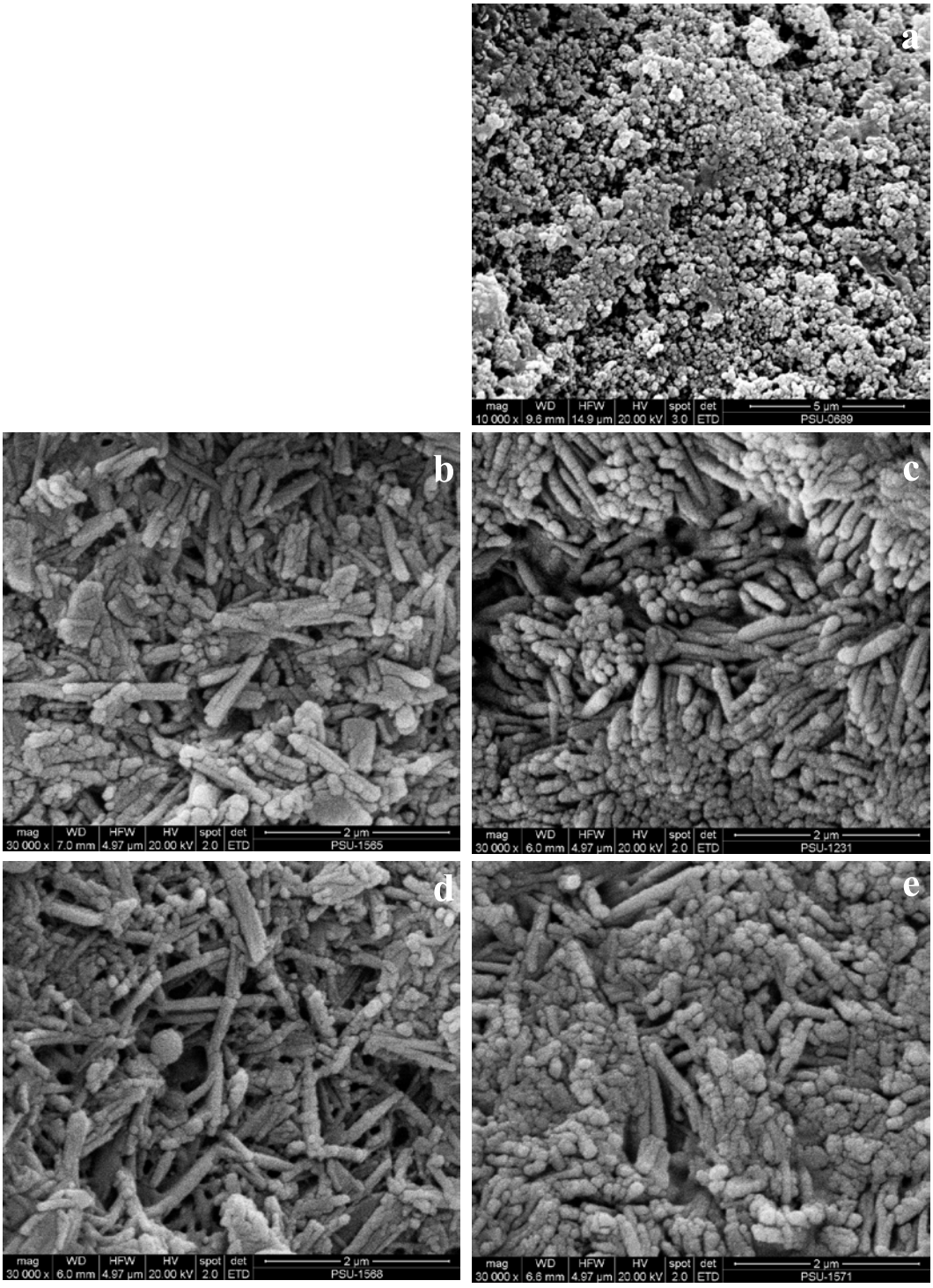

Figure 3.7 SEM images of the Si–nHA powders: (a); Si–nHA before immersion, (b); 0.3Si–synHA, (c); 0.4Si–synHA, (d); 0.3Si–contHA, and (e); 0.4Si–contHA after immersed in PBS for 14 days

3.2.5 Thermo-gravimetric analysis (TGA)

The materials produced by using 0.3 and 0.4 mole of calcium silicate as the Si source were chosen for TGA analysis to assess thermal behavior between 25 and 1300 °C. The TGA curves were displayed in Figure 3.8 and summarized for percentages of weight loss in Table 3.3. The 0.3 and 0.4Si–contHA powders showed the similar thermal behaviors. The 0.3 and 0.4Si–synHA also displayed the same thermal phenomena. There were 3 temperature ranges revealing weight loss, including 25-500 °C, 500-1000 °C and 1000-1300 °C. At temperature lower than 500 °C, approximately 1.05%, 0.78%, 1.06 and 2.25% weight loss were indicated for 0.3Si–contHA, 0.4Si–contHA, and 0.3Si–synHA and 0.4Si–synHA powders, respectively. Between 500-1000 °C, little weight loss was observed for the former three samples (∼1.3%) and the fourth material exhibited 2.54% weight loss. At temperature between 1000 and 1300 °C, a little change in the weight was apparent for 0.3 and 0.4Si–contHA. However, the Si–synHA materials displayed the second weight loss when raising the temperature to 1300 °C. In addition, thermal stability of the Si–contHA products was higher than that of the Si–synHA substrates. These powders had thermal stability in an increasing order of 0.4Si–contHA ≈ 0.3Si–contHA > 0.3Si–synHA >> 0.4Si–synHA.

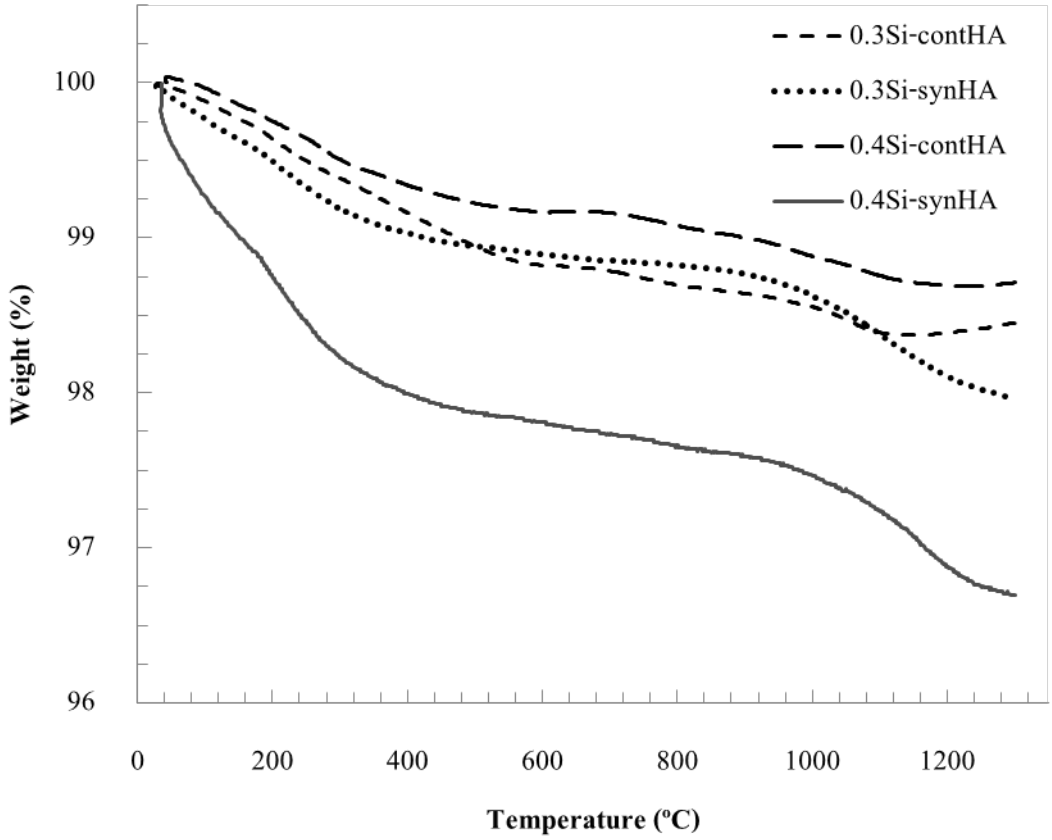

Figure 3.8 TGA curves for 0.3Si–contHA, 0.3Si–synHA, 0.4Si–contHA, and 0.4Si–synHA in the temperature range between 25 and 1350 °C

Table 3.3 Thermal behavior of the specified Si–nHA powders derived from TGA curves

Sample	Temperature (°C)					
	Weight (%) of materials			Weight loss (%)		
	T_{500}	T_{1000}	T_{1300}	T_{500}	T_{1000}	T_{1300}
0.3Si–contHA	98.95	98.55	98.45	1.05	1.45	1.55
0.4Si–contHA	99.22	98.88	98.71	0.78	1.12	1.29
0.3Si–synHA	98.94	98.63	97.96	1.06	1.37	2.04
0.4Si–synHA	97.87	97.46	96.69	2.13	2.54	3.31

3.2.6 Zeta potential (ζ)

The zeta potential (ζ) study was performed to characterize surface charges of the as-synthesized Si–nHA powders and those after immersed in PBS for 14 days at three different pH levels (pH 6, 7 and 8). The results were shown and summarized in Figure 3.9 and Table 3.4. All of the materials had negatively charged surfaces with ζ ranging between -7 and -12 mV. The highest and lowest values were found for the 0.4Si–contHA samples at pH 6 and the apatite-induced 0.4Si–synHA materials at pH 8, respectively. The less negatively charged surface was determined for the as-synthesized 0.3Si–contHA powders. The ζ values of the 0.3Si–synHA powders were not varied by increasing the medium pH. After apatite was induced to form on the surfaces, most of the materials exhibited more negatively charged at pH 6 with the exception of 0.3Si–contHA. The 0.4Si–synHA showed positive ζ value at pH 7, but having negative ζ value at pH 8.

Table 3.4 The zeta potenial ζ (mV) of the as-synthesized materials and those of after immersed in PBS for 14 day at pH 6, 7 and 8

Material	ζ (mV)					
	pH 6		pH 7		pH 8	
	0 day	14 days	0 day	14 days	0 day	14 days
0.3Si–contHA	-9.47±0.98	-8.73±0.94	-8.24±1.00	-9.40±1.24	-7.43±2.00	-8.94±1.24
0.3Si–synHA	-7.66±1.09	-10.53±0.35	-8.05±1.46	-10.02±1.65	-7.55±0.85	-7.89±1.65
0.4Si–contHA	-6.77±0.43	-11.29±2.44	-7.09±0.80	-8.30±0.321	-8.91±0.77	-7.61±0.32
0.4Si–synHA	-8.19±1.46	-11.70±0.20	-7.57±0.17	-7.13±1.23	-9.19±0.57	-12.27±1.23

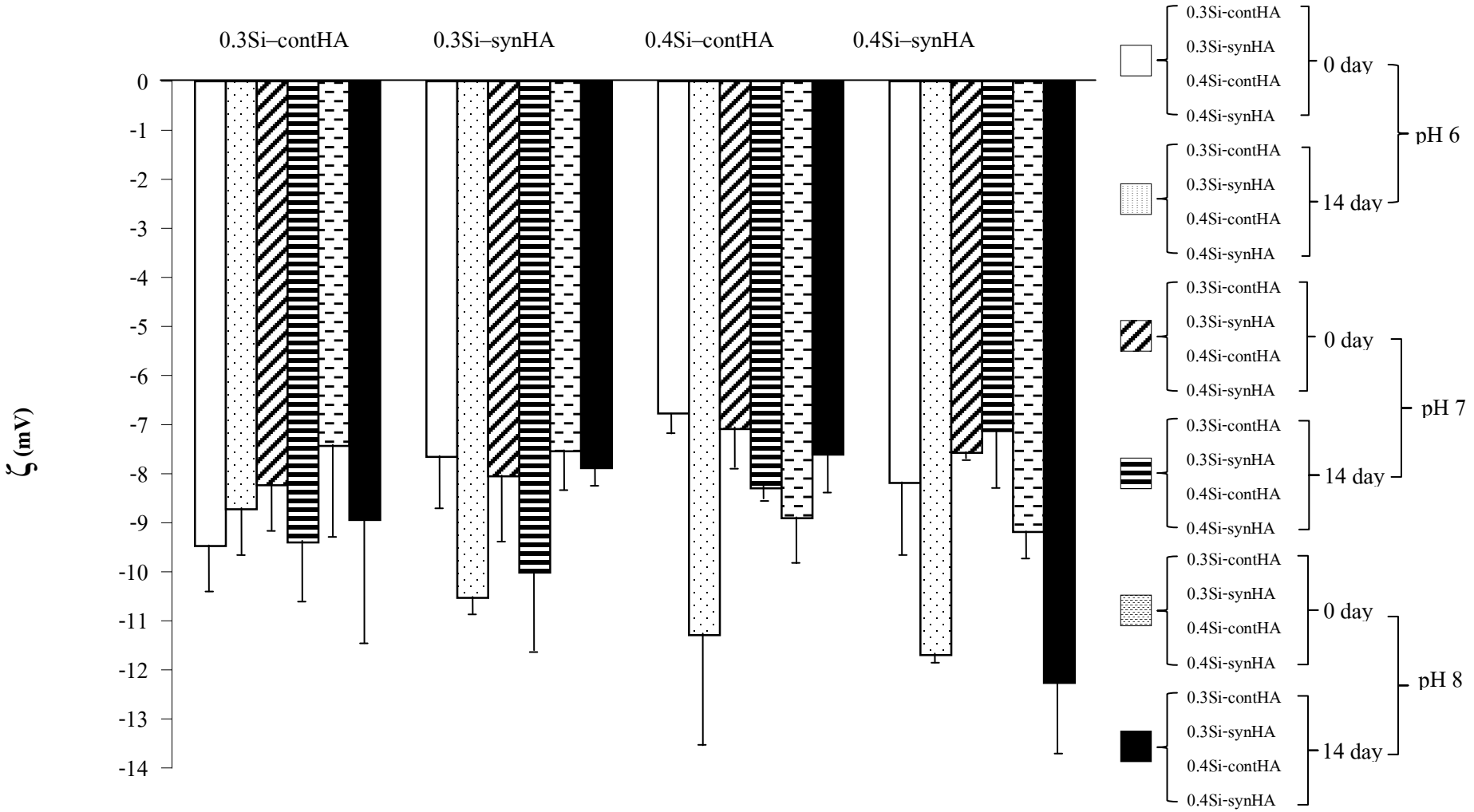

Figure 3.9 The ζ (mV) of the as-synthesized particles and those of after immersed in PBS for 14 day at pH 6, 7 and 8

3.3 Part III: Preparation of drug-free scaffolds

3.3.1 Fabrication of scaffolds

Four types of the apatite induced materials, including 0.3Si–contHA, 0.3Si–synHA, 0.4Si–contHA and 0.4Si–synHA were used in fabricating scaffolds. The ceramic powders were molded into 3D structure by titillated with chitosan to form smooth paste and treated with TPP, which used as a cross-linker. After freeze-drying, all of the fabricated scaffolds presented similar morphologies, by exhibiting numerous macro/micro pores with interconnected porous network. The pores were uniformly distributed throughout the 3D structures as indicated in Figure 3.10.

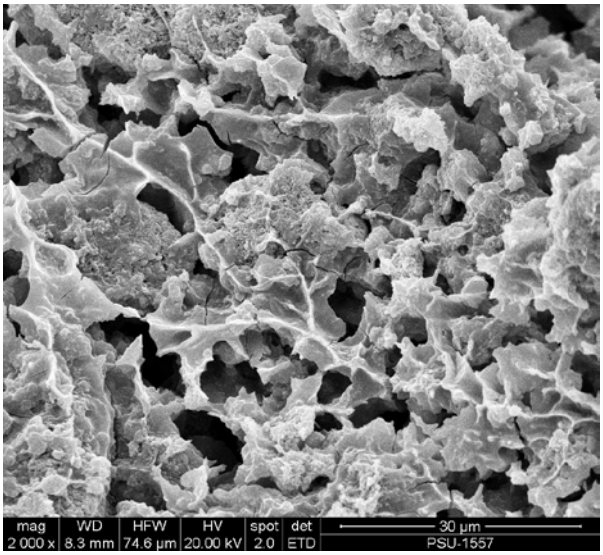

Figure 3.10 SEM image indicating porous structure of the scaffolds

3.3.2 Evaluation of drug-free scaffolds *in vitro*

3.3.2.1 The release of Ca^{2+} and PO_4^{3-} ions

The release of Ca^{2+} and PO_4^{3-} from the fabricated scaffolds within 30 days of the immersion in PBS at 37 °C was determined by the colorimetric assay method. In Figure 3.11, Ca^{2+} and PO_4^{3-} rapidly released into the medium within the first 15 days, the concentrations of which were about 220 µg/mL and 140 µg/mL, respectively. The release reached the plateau concentrations at these levels. The pattern of Ca^{2+} and PO_4^{3-} releases were similar, although of different concentrations. Additionally, the released concentrations of either Ca^{2+} or PO_4^{3-} among the test scaffolds were not significantly different.

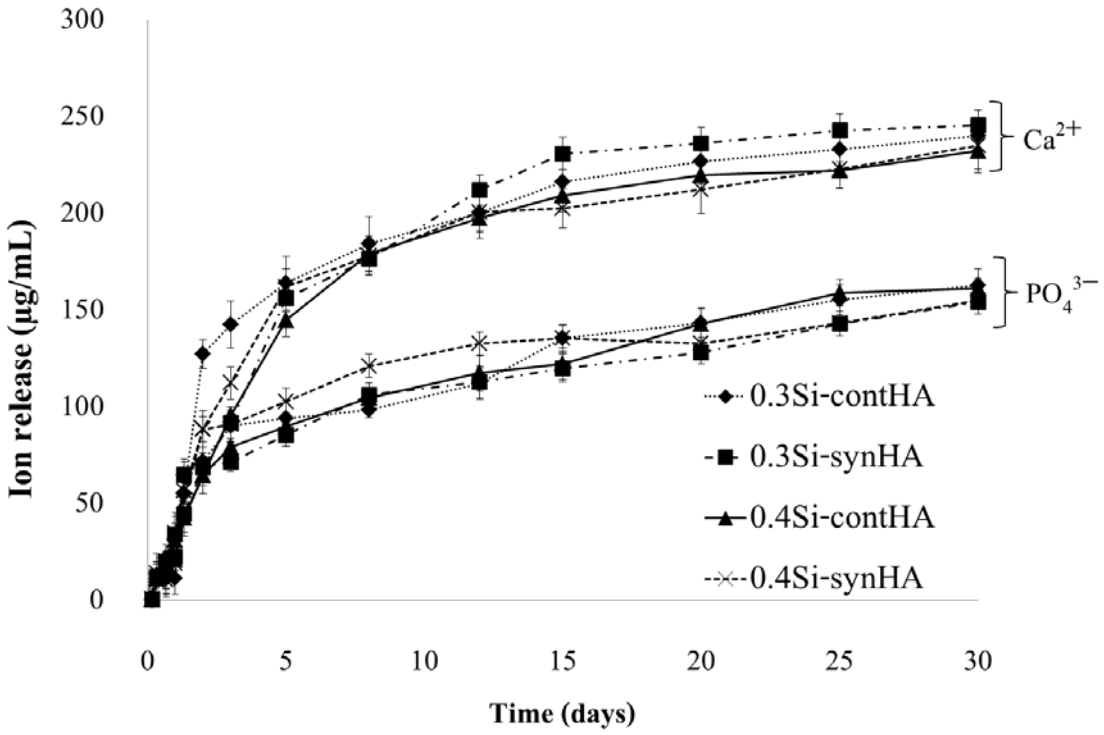

Figure 3.11 The concentrations of Ca^{2+} and PO_4^{3-} released from four different types of the scaffolds within 30 days in PBS at 37 °C (n=3)

3.3.2.2 Scaffold degradation

The scaffolds fabricated from 0.3Si–contHA, 0.3Si–synHA, 0.4Si–contHA, and 0.4Si–synHA powders were determined for *in vitro* degradation in PBS at 37 ºC for 30 days. The results were displayed in Figure 3.12. After 5 days of the immersion, there were no different in degradation rate among the samples. The degradation of the 0.3Si–contHA scaffolds was as high as 30% after 30 days, whereas that of the 0.4Si–synHA was only 20%. As arranged in an increasing order of the degradation, the order was that 0.4Si–synHA < 0.4Si–contHA < 0.3Si–synHA < 0.3Si–contHA.

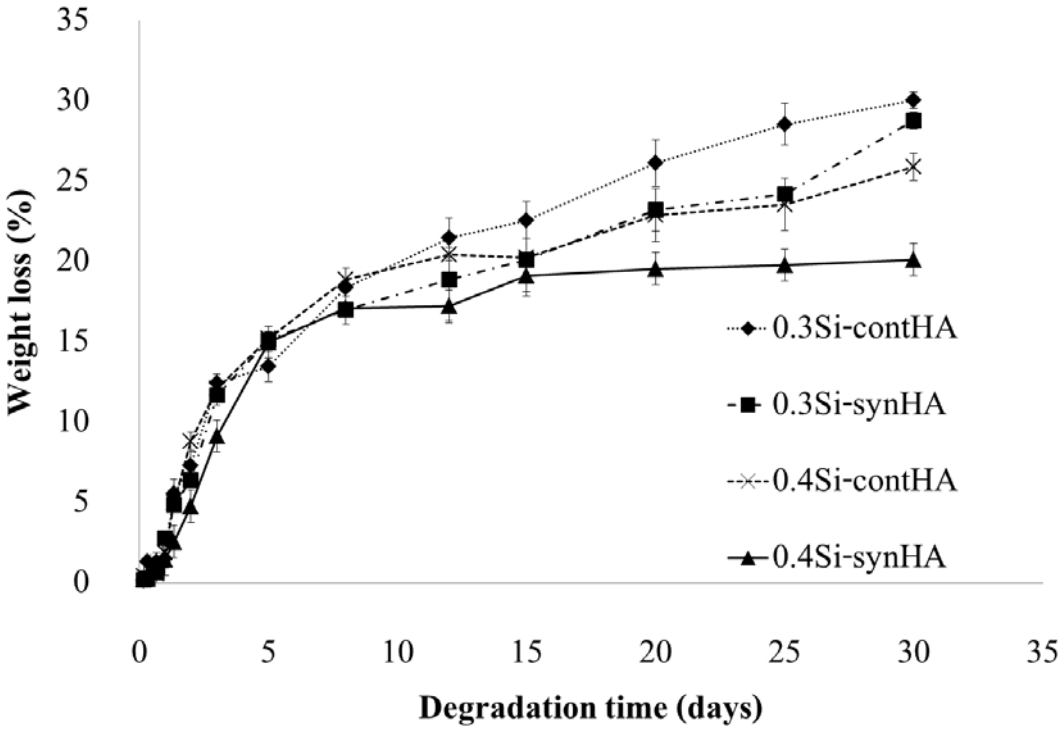

Figure 3.12 The percentage weight loss of the scaffolds prepared from 0.3Si–contHA, 0.3Si–synHA, 0.3Si–contHA, 0.3Si–synHA materials after immersed in PBS at 37 °C for 30 days

3.3.2.3 Protein adsorption on the fabricated scaffolds

The ability of proteins to be adsorbed on the scaffolds was determined by incubating them in serum-supplemented DMEM for 1 and 3 days. This was followed by semi-quantitative characterization of the adsorbed protein by using SEM. The SEM micrographs of its corresponding control (scaffolds containing the bioactive 0.4Si–contHA) and those of the un-adsorbed surfaces were also taken into consideration. As shown in Figure 3.13, the nano-topographical features of the unbound 0.4Si–synHA and 0.4Si–contHA surfaces were significantly different. At 1 day of the immersion, the area in that proteins were adsorbed on the 0.4Si–synHA surface (Figure 3.13d) was more extensive than that of the 0.4Si–contHA substrate (Figure 3.13c). Within the adsorption loci, however, the protein sheets previously covering the later material seemed to be thicker than those spreading on the former surface. After 3 days of the adsorption, structural rearrangement of protein fibrils on the 0.4Si–contHA ceramic were detected (Figure 3.13e), whereas those deposited on the 0.4Si–synHA substance were stabilized (Figure 3.13f).

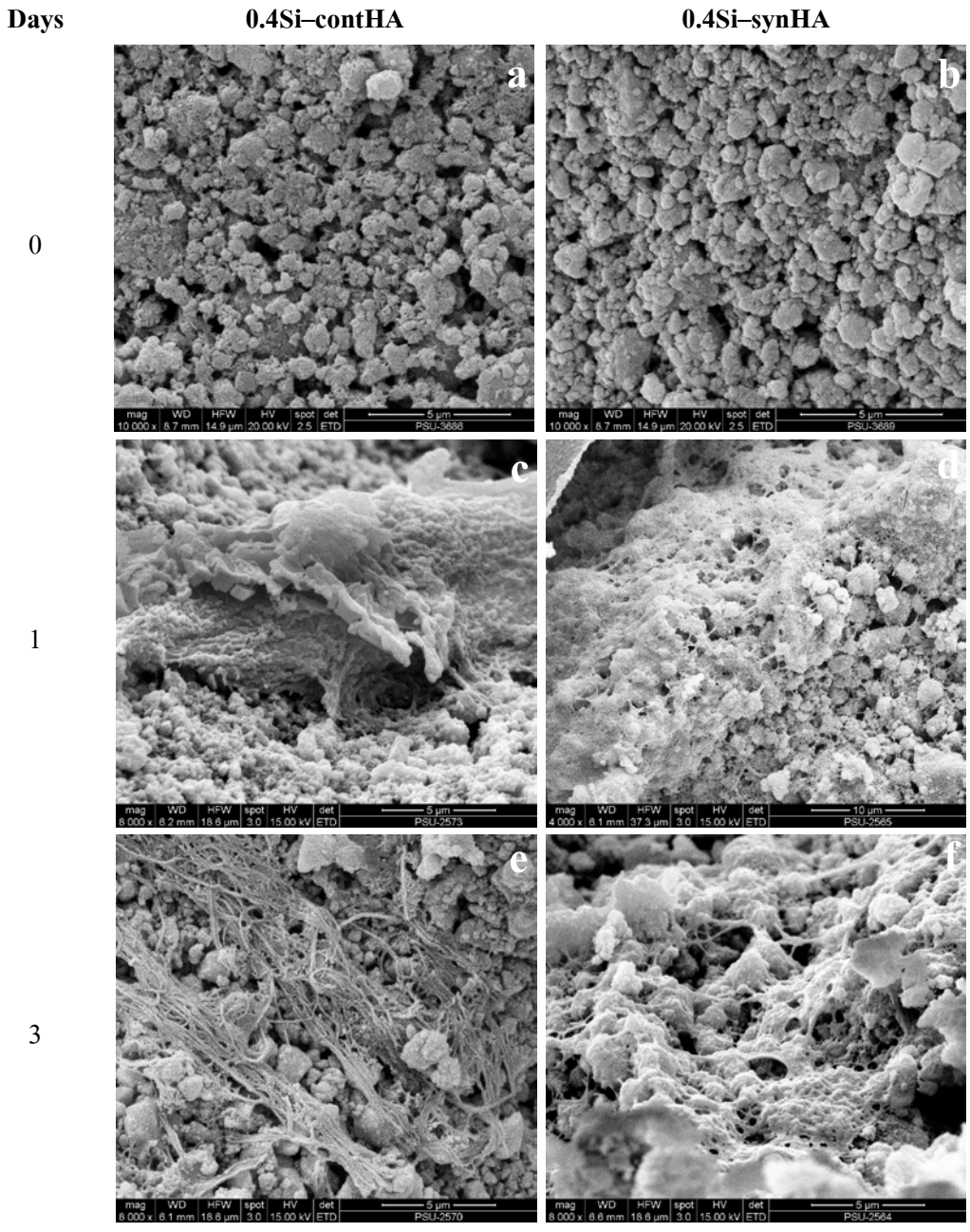

Figure 3.13 SEM micrographs of proteins adsorbed on scaffold surfaces after soaking in serum supplemented DMEM for 1 and 3 days: The scaffolds were fabricated from the bioactive 0.4Si–contHA and 0.4Si–synHA particles**.**

3.4 Part IV: Loading of VCM and rhBMP2

3.4.1 Loading of VCM

The scaffolds containing 0.3Si–contHA, 0.3Si–synHA, 0.4Si–contHA, or 0.4Si–synHA powders were performed for loading of VCM. VCM was successfully loaded into the scaffolds by soaking them in the drugs solutions at different concentrations ranging between 5 and 100 mg/mL. More than 90% of the drug was incorporated in the scaffolds, regardless of the used materials for scaffolds fabrication (Table 3.5).

Table 3.5 Entrapment Efficiency (%EE) of VCM in scaffolds containing different types of the ceramic materials

Sample	The initial VCM concentration (mg/mL)			
	100	20	10	5
	% EE			
0.3Si–contHA	99.49±0.07	97.49±0.06	95.07±0.13	90.59±0.07
0.3Si–synHA	99.48±0.15	97.53±0.04	95.10±0.09	90.73±0.08
0.4Si–contHA	99.48±0.06	97.51±0.10	95.09±0.11	90.47±0.14
0.4Si–synHA	99.49±0.05	97.44±0.02	95.15±0.04	90.82±0.05

3.4.1.1 *In vitro* VCM release

The release profiles of VCM from the scaffolds in PBS at 37 °C were demonstrated in Figure 3.14. Two different concentrations of VCM (e.g., 100 mg/mL and 5 mg/mL) were used for loading into the scaffolds (labeled as high or low drug loading, respectively), and studying of drug release. The high drug-loaded scaffolds showed abrupt release within a short period after incubation and reached plateau thereafter, typically followed the first-order release kinetic where the drug release rate was proportional to the amounts of drug remaining in the carriers. In contrast, VCM in the low drug-loaded scaffolds was released with a more constant flow out of the carriers, near zero order kinetic profile. Notably, the amounts of VCM released from the former structures were approximately eight times higher than that released from the latter samples, although the initial load was 20 times higher. Thus, the high drug-loaded scaffolds still contained greater amounts of the entrapped VCM after release. The percentage of drug release was obtained by normalizing the apparent released amount to the initial load. At 4 hours of incubation, the percentage of the drug released from the low drug-loaded scaffolds was approximately twice as high as that released from the scaffolds of high drug loading. Between 75% and 80% of the entrapped drug was released from the low drug-loaded scaffolds within 12 days. In contrast, only 20–30% of the drug was released from the high drug–loaded samples. In addition, the entrapped VCM was released in a controlled manner over a 12–day period.

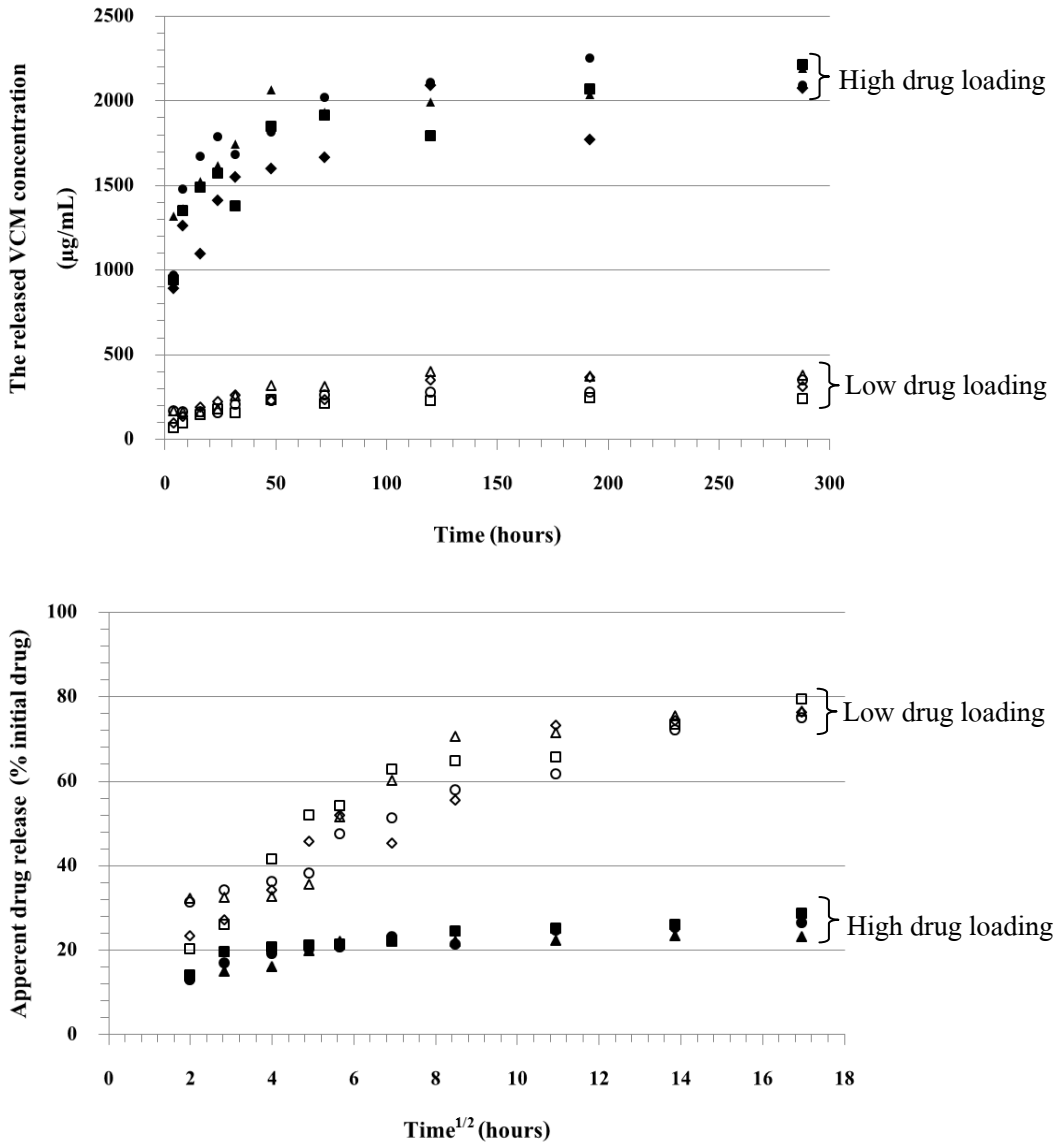

Figure 3.14 (a) The apparent amounts of VCM released from scaffolds fabricated by using either 0.3Si–synHA (○), 0.4Si–synHA (◇), 0.3Si–contHA (□), or 0.4Si–contHA (△) as a drug carrier with an initially high or low drug loading; all error bars were overlaid by the markers width (n = 3). (b) The plot of the percentage drug release as a function of time$^{1/2}$ (hours); the release study was performed on scaffolds fabricated by using either 0.3Si–synHA (○), 0.4Si–synHA (◇), 0.3Si–contHA (□), or 0.4Si–contHA (△) as a drug carrier with initially high or low drug loading; all error bars were overlaid by the markers width (n = 3).

3.4.1.2 Antimicrobial activity of VCM-loaded scaffolds

Broth dilution assay was used to determine antimicrobial activity of VCM-loaded scaffolds. The loading processes did not interfere the antimicrobial activity. VCM in the scaffolds was gradually released into the soaking medium at concentrations sufficient to inhibit the growth of *S. aureus* for at least 12 days. The half maximal effective concentration (EC_{50}), which is the concentration of the drug showing inhibition of the test bacterium by 50%, was determined to be in the range of 1.2–2 μg/mL. The percentage inhibition of the solutions released from VCM-loaded scaffolds was calculated to be in the range of 79.90–85.33 %.

3.4.1.3 Cytotoxicity of VCM-loaded Scaffolds

Cytotoxicity was performed by MTT assay method. Before the assay, rat osteoblast-like cells (ROBs), obtained from Miss Paweena Wongwitwichot at Prince of Songkla University, were cultured in Dulbecco's modified Eagle's medium-F12 (DMEM/F12) containing 6% FBS, 100 units penicillin G sodium, 100 mg streptomycin sulfate, 2% amphotericin B, and 2% L-glutamine. After confluence, the cells were harvested, counted and resuspended to a density of 1×10^5 cells/mL. A 100 μL cell suspension was seeded onto a well of 96-well plate, and incubated to allow cell attachment. A diluted extract (25% or 50% dilution) prepared from the VCM release solution was added to replace the culture medium. Fresh culture medium was used as the blank control. The plate was incubated further for 24 hours and evaluated for the cell viability using MTT assay. The MTT solution was added to each well after the medium was withdrawn and incubated for 4 hours. At the end of the incubation, the dimethylsulfoxide (DMSO) was added to each well to dissolve the purple formazan crystals. The optical densities of the formazan solutions were measured at a wavelength of 570 nm. The results of cell viability after exposure to various diluted extracts (25% and 50% dilution) were calculated and shown in Figure 3.15. The numbers of the cells was comparable when the cells were treated with the samples of different dilutions. Furthermore, the number of viable cells challenged by the

extracts was significantly higher than that of the control ($p < 0.05$). In addition, the difference in viable cell numbers was not statistically significant when using the extracts with similar dilutions ($p > 0.05$).

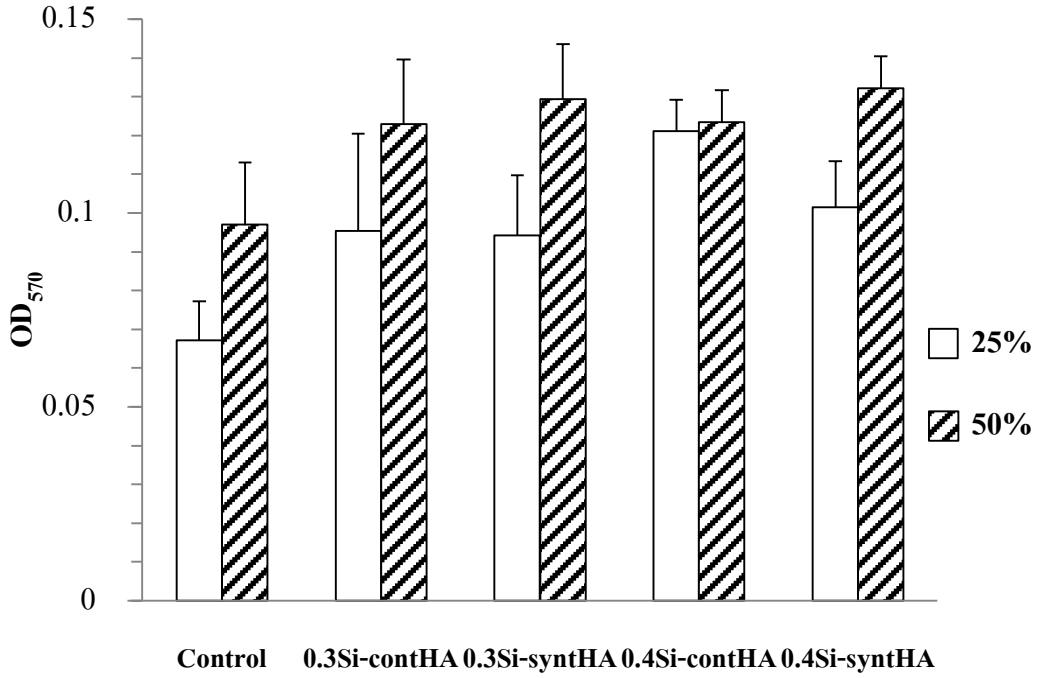

Figure 3.15 The viability of osteoblast-like cells cultured with different concentrations of the solutions extracted from VCM-loaded scaffolds consisting of 0.3Si–contHA, 0.3Si–synHA 0.4Si–contHA, or 0.4Si–synHA (n = 3)

3.4.2 Loading of rhBMP2

Before loading of rhBMP2, surfaces of the scaffolds were modified by coating with heparin. Heparin is an anionic glycosaminoglycan. It was chosen on the basic of its inherent capacity to bind to various growth factors via electrostatic interactions. The specific interaction between the negatively charged sulfate groups of heparin and the proteins' positively amino acid residues was considered to be essential for storage, release and protection of the rhBMP2 from heat, pH and enzymatic degradation. The covalent bonds between heparin molecules and the terminal amine (NH_2)-unreacted groups of chitosan in the scaffolds were introduced by using the carbodiimide chemistry. Firstly, the MES buffer was prepared by dissolving EDC and NHS in water. The MES buffer was used for preparing the heparin solution and activating the scaffolds. Then, the crosslinks were formed after the activated scaffolds were immersed in the heparin solution and subjected for characterization.

3.4.2.1 Stability of the bound heparin: characterized by toluidine blue staining

The presence of heparin on the scaffold surfaces was detected by toluidine blue staining method which is based on the complexation between heparin and toluidine that strongly binds to heparin. The heparinized scaffold was stained with toluidine blue to determine heparin on the scaffold. The distribution of the bound heparin was observed, according to the extent of the color intensity presented, as shown in Figure 3.16. The heparin immobilization was uniformly covered most of the surface and filled pores of the scaffolds. Because of highly porous, the immobilization reaction occurred on both the outer surfaces and the inner structure. The blue-color intensity was in corresponding with heparin binding capacity. By using 1% w/v heparin, the heparinized scaffolds elicited much denser blue staining than those obtained from 0.5% w/v heparin. However, clear difference in the color intensity was not revealed by using heparin at the concentrations of 1 and 2% w/v. Consequently, the result

indicated the limited numbers of the remaining reactive amine groups on the scaffolds. Furthermore, there was no blue staining of the scaffolds without heparin immobilization.

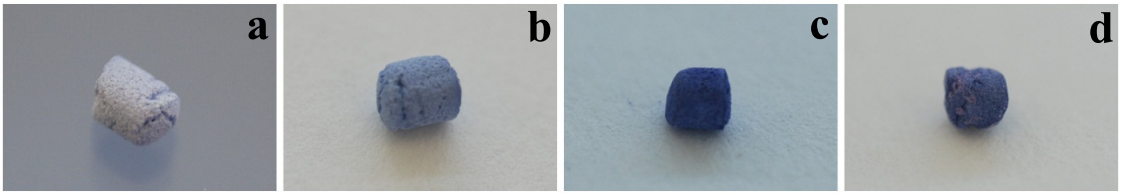

Figure 3.16 The photographs of toluidine blue staining for scaffolds with different degrees of heparin immobilization: the left-hand figure (a) was the representative scaffold without heparin immobilization; the two middle figures (b and c) were the scaffolds obtained by using 0.5 and 1.0% w/v heparin, respectively; and the right-hand figure (d) was the scaffold reacted with 2.0% w/v heparin

3.4.2.1.1 Stability and blood compatibility

The stability of heparinized scaffolds (being stored at 4 °C for 4 weeks) was determined from the clotting appearance by using PRP assay. The results were summarized in Table 3.6. Under physiological condition in PBS, the leaching of heparin from all cross-linked surfaces did not exist because there was clotted PRP. The heparin molecules were still immobilized on the surfaces upon storage. It was clear that the chemical immobilization process allowed heparin to be tightly bound on the scaffolds and remained stable for extended periods of at least 4 weeks. SEM images of the platelet adhesion test were shown in Figure 3.17. Many platelets with a few filopodia adhered on the non-heparinized surfaces of 0.4Si–contHA and 0.4Si–synHA (Figure 3.17a and b). For the 0.4Si–contHA scaffolds that were immobilized with 0.5% w/v heparin, the adhesion of platelets was still evident (Figure 3.17c). A significant suppression of platelet adhesion was exhibited by using higher heparin concentrations (Figure 3.17e and g). Furthermore, very rare platelets were adhered on the 0.4Si–synHA scaffolds even the immobilization reaction was carried out at 0.5% w/v heparin (Figure 3.17d). Therefore, the 1% w/v heparin was optimal for both materials to be employed in the conjugation process. Because of eliciting hemo-compatibility, the heparinized scaffolds were less likely to initiate thrombosis. Shrinkage, disintegration and fast degradation of the modified scaffolds were not observed within a period of 4 weeks in aqueous solutions (data not shown).

Table 3.6 Clotting appearances of blood by incubating with the rinsed solutions of the heparinized scaffolds

Heparin	**Type of the material used for preparing scaffold**				
(%)	**Control**[a]	0.3Si–contHA	0.3Si–synHA	0.4Si–contHA	0.4Si–synHA
0.5	–	+	+	+	+
1	–	+	+	+	+
2	–	+	+	+	+

a: heparin solution was used instead of the rinsed solutions obtained from the soaking the heparinized scaffolds in PBS. Symbols: – no clotting; + clotting

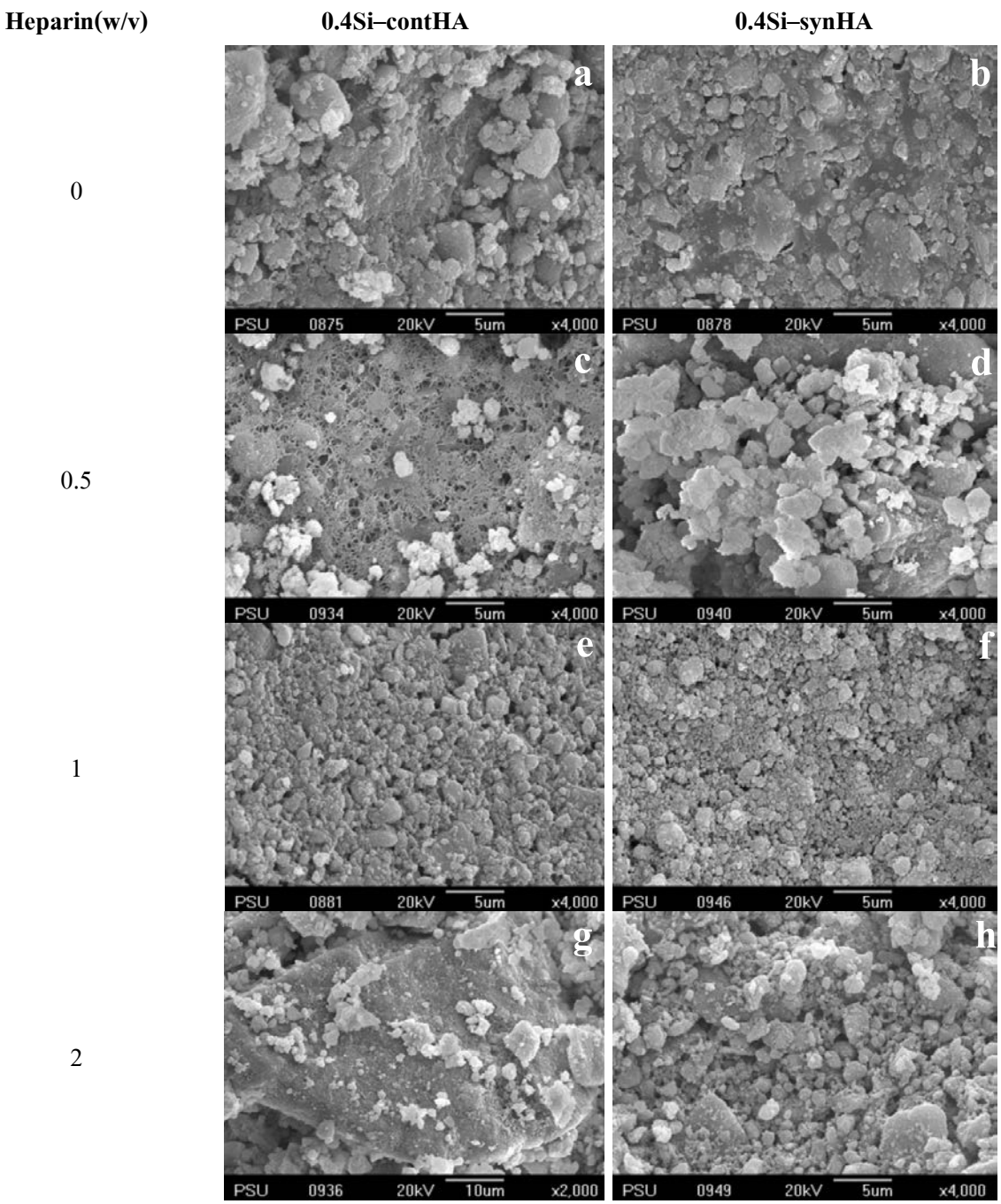

Figure 3.17 SEM images of platelets adhered on the scaffold consisting of 0.4Si–contHA or 0.4Si–synHA, previously heparinized by using 0 (a and b), 0.5 (c and d), 1.0 (e and f), and 2.0 (g and h) % w/v heparin, respectively

3.4.2.2 Loading of rhBMP2 onto the heparinized scaffolds

Different concentrations of rhBMP2 (5 and 10 μg/mL) were separately applied onto scaffolds before which heparin at either 0.5 or 1 % w/v was immobilized. Using this system, the long-term delivery of a small amount of rhBMP2 was expected.

3.4.2.3 *In vivo* evaluation of rhBMP2 loaded scaffolds

The subcutaneous transplantation of rhBMP2-loaded scaffolds was carried out in rats to estimate their efficacy of inducing ectopic bone formation, compared to those of non-heparin or non-rhBMP2 loading. The implanted animals showed no complications in wound healing and remained healthy during the 4 week follow up. The results of hematoxylin/eosin (HE) and alizarin red S (ARS) staining for histological sections were illustrated in Figure 3.18. By investigating inside into the HE stained sections, the attachment to all samples of macrophages was not evident. Positive staining of alizarin red S was represented by dark red regions, indicating the presence of mineral composition. In the pockets resided by scaffolds where both heparin and rhBMP2 were unloaded (Gr.1 samples), they were simply closed with fibrous tissues. According to rhBMP2 deficient samples, heparin induced only a negligible amount of bone formation in Gr.2, whereas the effect was apparent to be higher in Gr.5. By comparing the immobilized heparin between 0.5 and 1.0% w/v, its consequence was not different for the scaffolds immobilized by 10 μg/mL rhBMP2 (Gr.4 and 7). Furthermore, the newly formed bone was mainly found as a shell around the implants or along the implant fractures. Interestingly, the inner-portion sections of Gr.6 implants showed the most evidence of bone formation after 4 weeks. As dark red mineral lines were observed throughout the implants, the result indicated that osteogenesis started simultaneously at multiple sites.

Group No.	Heparin (% w/v)	rhBMP2 (μg/mL)
1	0	0
2	0.5	0
3	0.5	5
4	0.5	10
5	1	0
6	1	5
7	1	10

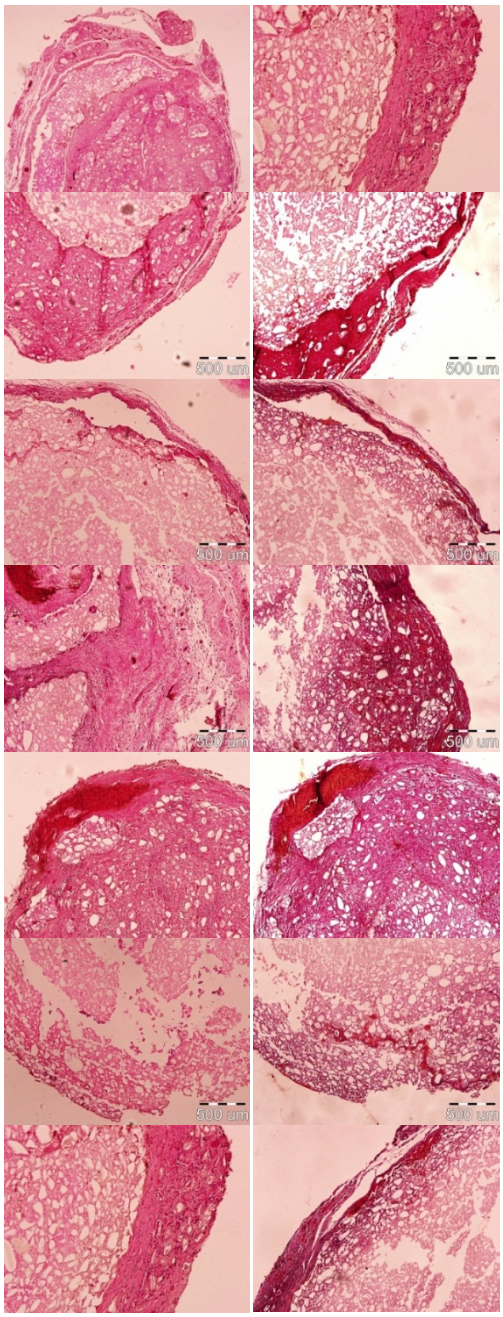

Figure 3.18 The hematoxylin/eosin (HE) and alizarin red S (ARS) staining of scaffold sections after subcutaneously implanted in rats for 4 weeks: Heparin at a concentration of either 0, 0.5, or 1.0% w/v was immobilized on the scaffold, followed by the rhBMP2 immobilization at a concentration of either 0, 5 or 10 μg/mL. The scale bar indicated 500 μm.

3.5 Part V: *In vivo* evaluation of VCM/rhBMP2 loading scaffolds

3.5.1 Implant design and fabrication

The scaffolds were designed in three groups (see 2.6.1). VCM and rhBMP2 at the respective concentrations of 100 mg/mL and 5 μg/mL were separately loaded onto a half of each scaffold by applying the previously established method (see 2.5). The prepared implants were stored at 4 ºC until use.

3.5.2 Osteomyelitis induction in rats

MRSA strain BAA 1680 was used for osteomyelitis induction. The bacterial cell pellet was prepared by using tryptone soy broth (TSB) until a Mcfarland standard of 0.5 was obtained. The bacterial suspension was diluted to the density of 10^5 CFU/mL. The ethics committee for animal studies of Prince of Songkla University had previously approved the animal experiment. Twenty healthy male Wistar rats weighing about 250–280 g were anesthetized intramuscularly with the mixture containing xylazine and zoletil. Their right hind legs were shaven and disinfected. A 100-μL bacterial suspension was loaded into the medullary cavity of tibia by injecting at epiphysis, followed by drilling the needle (gauge 23) through cortical and spongy bone until accessing the cavity. The animals were kept in individual cages and followed up for clinical signs of infection. A few days following bacterial inoculation, minor redness and swelling with an elevated skin temperature were identified at and around the injected sites. The body weight of the animals returned to basal level after 2 weeks, followed by further weight gain. All the animals survived 4-weeks post-inoculation and showed mild to moderate signs of infection. Signs of systemic illness were not detected. When left untreated for another 8 weeks, the X-rays of the proximal tibias showed shadows of soft tissue swelling. The bone matrices of proximal epi–/metaphysic regions were uneven, and some areas were sclerotic or had low density (Figure 3.19a). No fistulae were observed. The bacterial culture confirmed that all tissue

specimens were contaminated by *S. aureus* as inoculated. The outcomes provided evidence that the rat osteomyelitis model had been successfully established in this study.

3.5.3 Implantation

A 10-mm segment of infected tibia was surgically removed and immediately radiographed by using X-ray (Figure 3.19b). There were no animals left untreated after the segment removal. Instead, the bone spaces were individually replaced by the scaffolds of V–, B–, or VB–group. After 8 weeks of implantation, bridging between the implants and the remaining original bones was clearly observed, indicated by the increased radiograph density along the implants radius (Figure 3.19c-e). In addition, the residual implants of V–group (Figure 3.19c) were determined to be smaller than those of B– and VB–group (Figure 3.19d and e).

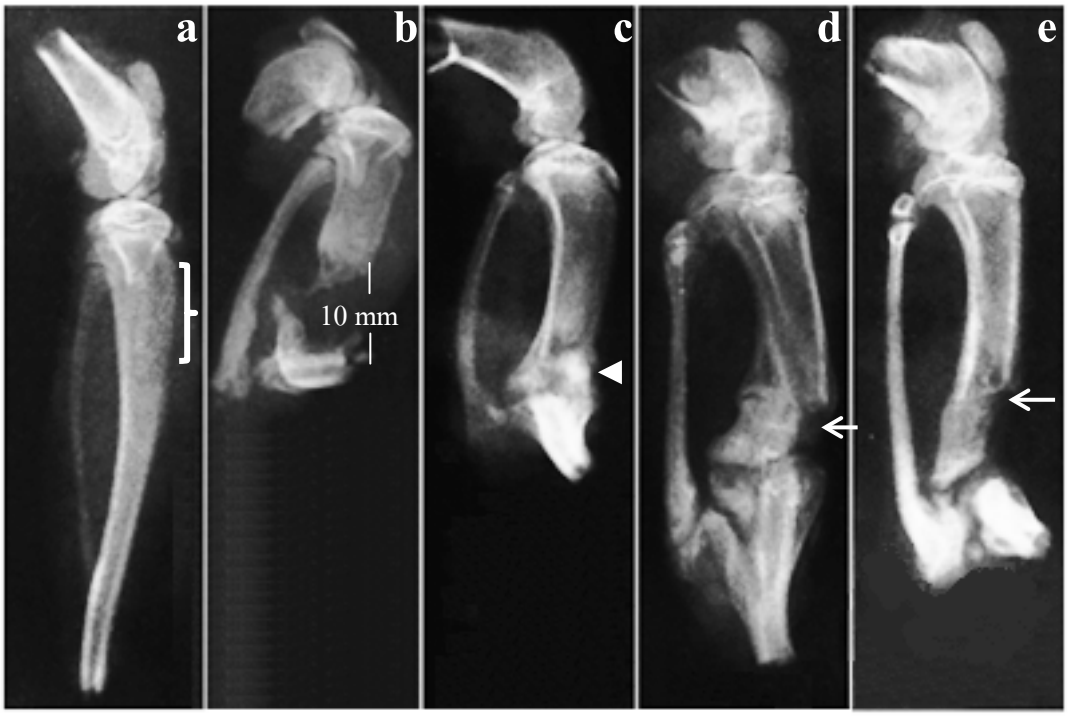

Figure 3.19 The representative radiographs of (a), bone destruction at proximal epi–/metaphysic region of tibia ( ), assigned for osteomyelitis appearance; (b), the occurring bone space immediately after a 10-mm segment was removed; (c), the residual implants of V–group after 8 weeks post-implantation (arrow head); (d and e), bridging between the implants and the remaining original bones of B– and VB–group, respectively, after 8 weeks post-implantation (arrows).

3.5.4 Histological analysis

The implants were surrounded by thin layers of fibrous tissue with discontinuation in some places (Figure 3.20d). New bone formation was highly determined for the specimens of B- and VB-groups. The amount of new bone for the samples of B–group was comparable to those of VB-group, but this was significantly greater than those of V–group. Other tibial structures were relatively normal. Vasculature was observed in the center of the implants of B– and VB–groups (Figure 3.20insert). According to bacterial culture test, the implant-surrounding tissues were still contaminated by the inoculated *S. aureus*. The bacterial counts were of 10 and 10^4 CFU/g of tissue for VCM-containing specimens and those lacking the antibiotic, respectively. Thus, bacterial colonization was reduced by the implants containing VCM, although the specimens of VB-group were examined to have less bacterial contamination than those of V–group ($p = 0.039$). The animals in these two groups showed no clinical signs of infection, whereas the signs were detectable in a half number of the animals (50%) in B-group ($p = 0.028$).

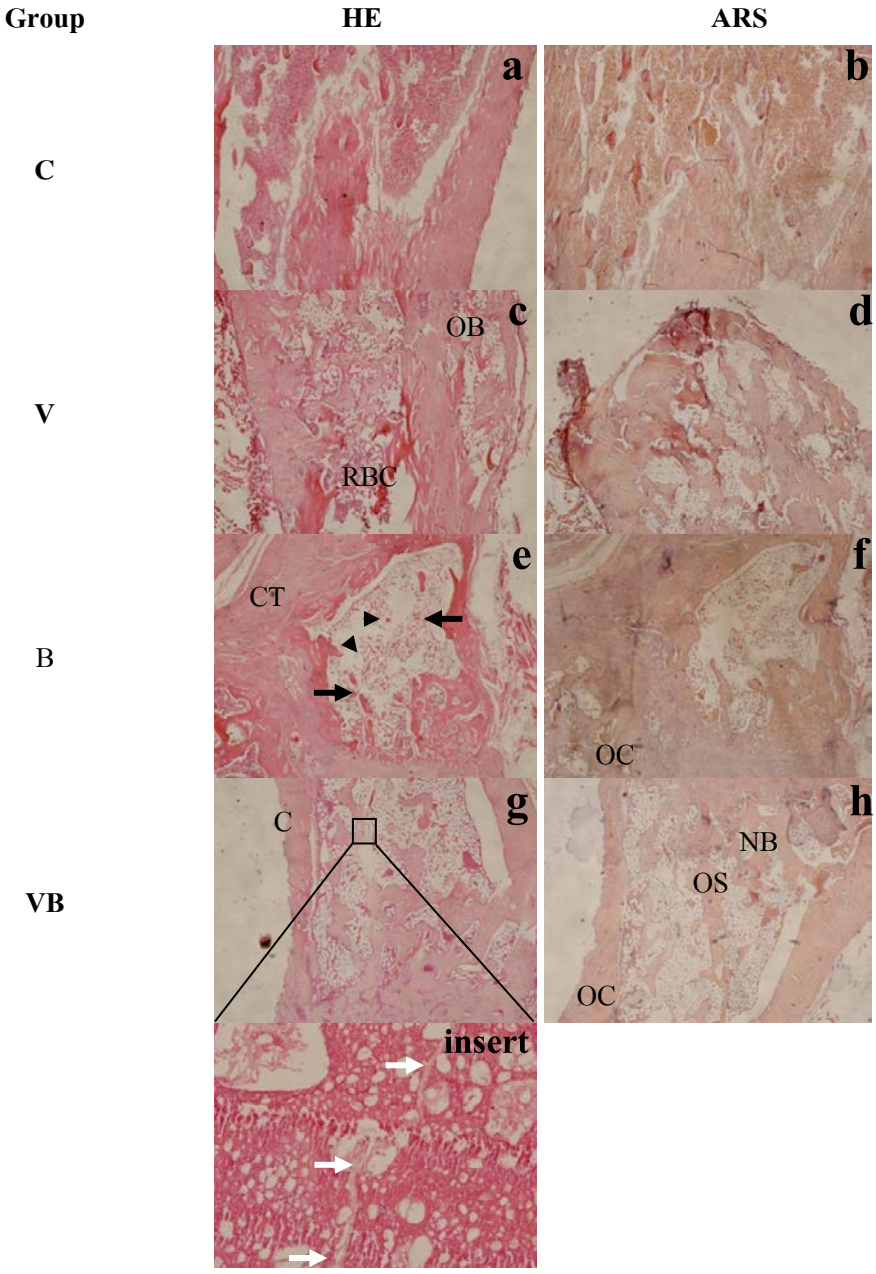

Figure 3.20 Sections along the bone defects for the specimens of V–, B–, and VB–groups after 8 weeks post-implantation. The sections were stained by hematoxylin/eosin (HE) or alizarin red S (ARS), and compared to those of the untreated controls. Areas of calcified tissues are indicated in brown or red-brown upon alizarin red S staining. Black arrows and arrow heads in Figure.3.20e represent foreign-body giant cells and neutrophils, respectively. White arrows in an insert frame indicate vascularization. Symbols: RBC, red blood cells; CT, connective tissue; NB, new bone; OB, osteoblasts; OC, osteocytes; C, osteoclasts; OS, osteoid

CHAPTER 4

DISCUSSIONS

The skeleton defect causing osteomyelitis (OM) remains a challenging problem in orthopedic surgery. It may be insufficiently treated by oral or systemic administration due to the scant of blood vessel in the mineralized tissues. This limits the ability of drug able to reach the defect bone and may result in a poor drug circulation to cells of the inner bone. Recent researches in drug delivery have led to significant progress in the development of local drug delivery system to the inner bone, although the current standard for OM treatment requires a combination of adequate surgical debridement and antibiotics therapy. Surgery is used to remove diseased bone and tissue or to drain pus, which often leaves an empty space in the bone. Placement of PMMA beads containing gentamicin at the defected site following a thorough debridement has been recommended for curing [203]. However, the stepwise procedures have proven to be inferior, due to the need of secondary surgery to remove the beads before implantation of bone graft. Indeed, the abilities in the controlling infection and promoting bone formation simultaneously are a key for successful regeneration of non–sterile bone defects. Consequently, this is the rationale why we combined an antibiotic and a bone growth factor into a single bone graft device that would be useful in effectively controlling infection and promoting bone regeneration simultaneously. This thesis focused on the development of Si–nHA materials at nano–sized ranges for fabrication of scaffolds containing VCM and rhBMP2, the preparation and characterization, *in vitro* and *in vivo* of the developed materials, and evaluation on efficacy of a single graft device containing VCM and rhBMP2 in controlling infection and promoting new bone formation *in vivo*.

4.1. Part I: Preparation of Si–nHA powders

The Si–nHA particles were prepared by using the wet chemical precipitation method modified from Swain 2009 [189]. $Ca(NO_3)_2$ and $(NH_4)_2HPO_4$ were used as starting materials at a fixed Ca/P ratio of 10:6. Trace amount of $CaSiO_3$ was incorporated to insert silicon into the stoichiometry of HA lattices. SiO_4^{4-} ions were obtained from $CaSiO_3$ hydrolyzed by H_2O to produce $H_2SiO_4^{2-}$. The decomposition of $H_2SiO_4^{2-}$ resulted in the SiO_4^{4-}. The ion substitutions of PO_4^{3-} ions by the SiO_4^{4-} species in the HA lattice could occur to produce $Ca_{10}(PO_4)_{6-x}(SiO_4)_x(OH)_{2-x}\square_x$ where "□" is the vacancy of OH^- groups which compensate charges in the Si−nHA molecules [98]. The synthetic condition could be strictly controlled. After calcinated at 1250 ºC, the final products at nanometric scale were obtained. These products were investigated in comparison with the control products, prepared by using the commercial HA instead of $Ca(NO_3)_2$ and $(NH_4)_2HPO_4$ for the first precipitation reaction (see 2.2.1).

4.2. Part II: Physical characterizations

The evidence of Si substitution into HA framework by using our developed method was observed. There was the replacement of PO_4^{3-} tetrahedral groups by SiO_4^{4-} tetrahedral species in the HA crystal as confirmed by FTIR analysis (Figure 3.5 and Figure 3.6). The intensity at 3570 cm^{-1} of Si–substituted samples significantly decreased by the incorporation of trace amount of silicon, compared with that of the HA. Due to the extra negative charge of SiO_4^{4-} ions, some OH^- ions were lost to compensate charge balance within the Si–nHA molecule [204, 205], according to the equation proposed by Gibson *et al.* [98]. The lattice of Si–substituted HA could be illustrated in Figure 4.1.

$$10Ca^{2+} + (6-x)PO_4^{3-} + xSiO_4^{4-} + (2-x)OH^- \longrightarrow Ca_{10}(PO_4)_{6-x}(SiO_4)_x(OH)_{2-x}\square_x$$

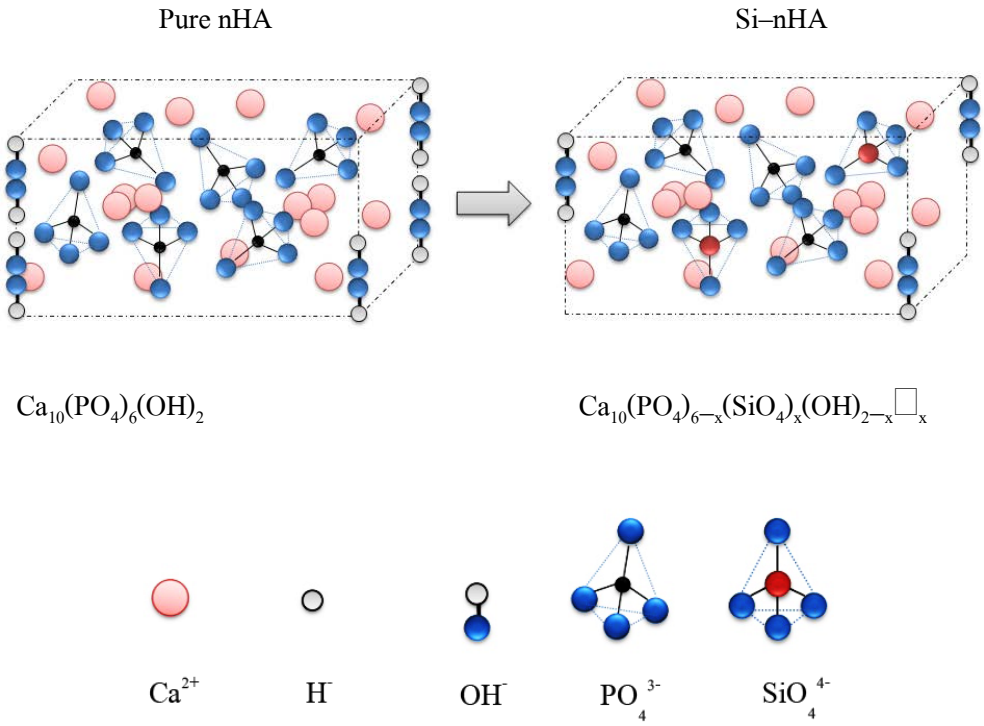

Figure 4.1 Schematic drawing in structural lattices of pure nHA and of Si–nHA [206]

According to XRD analysis (Figure 3.3), the Si–nHA products revealed as amorphous phases, compare to the control HA sample (not containing Si). It was pointed out that the Si atoms took part of HA particle [204]. Additionally, the broadening of XRD effectively indicated the decrease of crystallite sizes. This result was in agreement with previous study [110]. Furthermore, the Si–nHA was proven to possess HA as the major phase. SEM images showed that the Si–nHA products were of fine particles, similarly to that obtained by using the commercialized HA (Figure 3.1). The results of FTIR analysis revealed that all of the synthesized products mainly composed of calcium and phosphate, although slightly differing in chemical stoichiometry. The chemical compositions as verified by XRF analysis revealed that their actual values of Ca/P ratio were much higher than those of the theoretical ratio. The high ranges of Ca/P ratio for Si–nHA products were useful as they were substantially free of carbonate ions. The materials had relatively high water solubility and were able to release silicon into solution (Figure 3.5 and 3.6) [207]. These were expected to be caused by the larger SiO_4^{4-} groups compared to the PO_4^{3-} species, leading to the distortion of the PO_4^{3-} tetrahedron in the HA lattice [208].

After calcification at 1250 ºC, the occurrence of other secondary phases, including α–TCP and β–TCP phases was observed (Figure 3.3). This finding suggested the conversion of HA into β–TCP and α–TCP that possibly occurred at temperatures around 1200 ºC [209]. Indeed, a small amount of HA still remained and was not transformed to the others (Figure 3.3). The α–TCP was not reconverted to the more stable β–TCP due to a large dwelling at temperatures slightly below 1125 ºC (Figure 3.3) [210]. This was in agreement with the previous study [211], indicating that the amount of Si-substituted HA has decreased to a relatively constant level in the first hour when fired at 1200 ºC with the corresponding increase in the formation of α–TCP. Furthermore, the formed α–TCP has been stabilized by the presence of Si [212]. The constraint occurred by SiO_4^{4-} substitution also limited the Si–nHA phase content and the number of moles of α–TCP to be created [96]. At high levels of silicon doping, the crystalline phases might be saturated with the excess silicon, leading to the undoped α–TCP phase formed coexisting with the residual calcium silicate in an amorphous phase. On the contrary, silica-deficient compositions may be transformed to β–TCP, as identified by Sayer *et al*. [213] using thermodynamic model. It has revealed that the fixing composition at (1.5%) 0.33 mole of Si to each mole of HA has been the optimal ratio in producing the saturated amount of silicon substituted α–TCP [214, 215]. Therefore, the phase transition phenomenon and the presence of impurities including calcium silicate might result in obtaining mixed phase composites and the deviation from the usual stoichiometric Ca/P ratios [216]. The differences in polymorphic microstructures have proven to create materials with distinct chemical and biological properties, especially biodegradability, that has been significantly advantage for new bone growth [217]. The solubility of α–TCP, β–TCP, and HA was relatively suggested as α–TCP > β–TCP >> HA, relating to the ability to be resorbed by the body [218, 219]. Of interest was that a greater dissolution and a faster resorption rate were revealed by the Si–CaP composites rather than CaP rich materials [220]. The replacement of Si caused structural defects, which being compensated by charge deficition. This also caused the high dissolution.

Biomaterials such as bioactive glass have found to have the ability to form bonds with bone after implantation into bodies. Active bone-like apatite layer starts to form at the material-bone interface and acts as an intermediate that can bond to bone [221]. The formation of

the apatite has been dependent on various parameters, including concentrations of phosphate/carbonate, ionic strength and pH of the surrounding solution, and the kinetics of nucleation and crystal growth processes [222-227]. Phosphate buffer saline (PBS) is a physiological solution commonly used to imitate the extracellular fluid, although lacking $Mg^{2+,}$ Ca^{2+}, and HCO^{3-} [228]. PBS was used in this study to induce the apatite nucleation on the surface of the synthesized materials. The inductive effect of PBS was restricted in comparison with SBF [228]. This would be advantageous of producing supersaturated Ca^{2+} and PO_4^{3-} ion concentrations, thereby increasing the deposition rate of highly resorbable phases of Si–nHA [229]. The formation of mat-like apatite layers on the samples containing Si was present over the surfaces after 14 days of soaking (Figure 3.7b-e). The apatite morphology was corresponded to bone-like apatite generated on bioactive specimens when resided in physiological environments [230]. The produced materials were recognized to be bioactive, since apatite layers were formed on these surfaces after incubation in PBS [231]. Changes in the mixed-phase occurred via the dissolution of α–TCP, although not directly related to the decrease in α–TCP characterized peaks (Figure 3.3). Instead, HA in the apatite was contemplated as nucleation sites to uptake Ca^{2+} and PO_4^{3-} ions dissolved from α–TCP, which then precipitated through the precursor phase of OCP or DCPD [232, 233]. The release of Ca^{2+} ions was associated with the decrease of Ca/P ratio and resulted in an increase of the solution pH. Then the apatite nuclei were newly formed, leading to the growth of apatite layers [234, 235], as schematically shown in Figure 4.2.

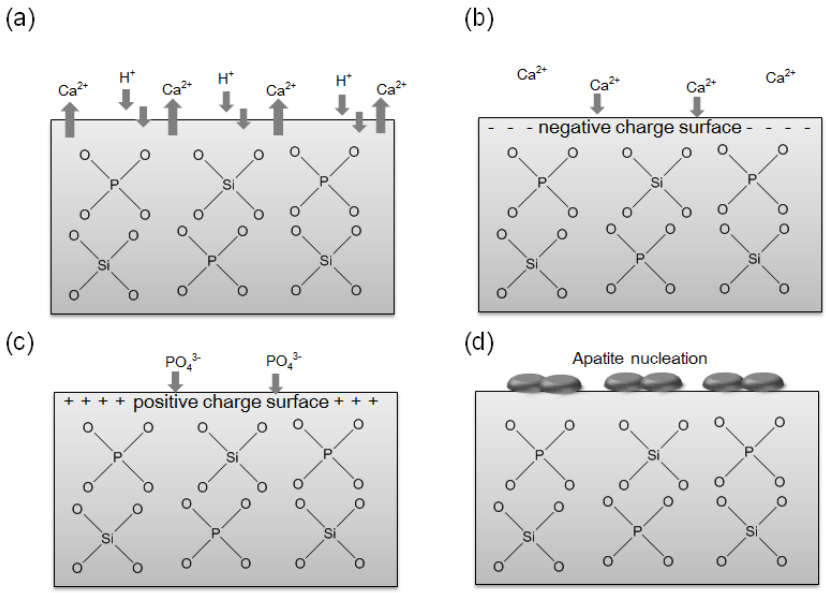

Figure 4.2 Schematic drawing for the mechanisms of apatite formation on Si–nHA in sequence from (a) to (d) [236]

The dense apatite layer could be developed on Si–nHA samples (Figure 3.7). Their resorption behaviors were expected to be higher than those deposited on the control surface. In the presence of carbonate ions, carbonate-substituted HA could be formed, leading to form bioactive and osteoconductive material that strongly bonds to bone.

4.3. Part III: Fabrication and characterization of drug-free scaffolds

Drug-free scaffolds were fabricated by molding into 3D architecture and stabilized by TPP-chitosan crosslinking. The negatively charged group of $P_3O_{10}^{5-}$ in TPP interact with the positively charged group of NH_3^+ in chitosan, resulting in matrix networks. The crosslinks were reversible, while sufficent to stabilize the scaffold construct, as shown in Figure 4.3. These crosslinks are promising for pharmaceutical application, due to no potential cytotoxicity [237]. The scaffolds were found to be highly porous with opened and interconnected pores distributing over the structure (Figure 3.10).

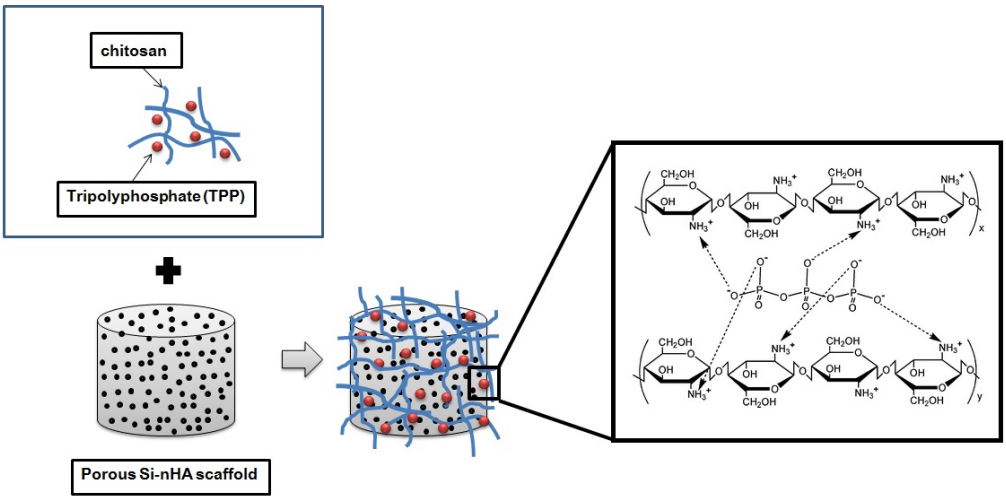

Figure 4.3 Schematic representation for the fabrication of drug–free scaffolds

In general, controls of degradation for implantable materials are necessary to match the rate of new tissue regeneration [238]. The degradation of Si–nHA scaffolds was observed by the release of Ca^{2+} and PO_4^{3-} in the incubation medium (Figure 3.12), estimating that 20–30 % of the scaffolds were degraded per month.

The behavior of protein adsorption was performed to know bioactive levels of the produced materials. Protein adhesion has been suggested as one important event of four major steps, i.e., protein adsorption, cell-substratum contact, cell-substratum attachment, and cell adhesion/spreading that precede cell proliferation [239-245]. Modification of the surface as such

will promote biological responses between biomaterial and living tissues after implantation in the body. Rapid protein adsorption on any surfaces of biomaterials means that the body positively responds to the biomaterials. In addition, the differences in quantities, densities, conformations, and orientations of the adsorbed proteins have been described to depend on chemical and physical characteristics of the surface that involve intermolecular forces, van der Waals forces, hydrophobic, or electrostatic interactions [246-248]. These differences may have profound effects on cellular attachment [249]. In Figure 3.13, there was no protein adsorption on the inactive surfaces regardless of the material types. There were sheets of proteins spreading over the bioactive surfaces. Protein fibrils were revealed to cover small parts of the Si–contHA scaffold by prolonged incubation (Figure 3.13e). The sheets of protein adsorption on the Si–synHA scaffolds were more stable than the control. The result could be explained by that higher concentrations of Ca^{2+} were released from the former material, generating surface charge property that was no longer suitable for protein attachment [250, 251]. Like other hydrophilic surfaces, the adsorption of proteins on Si–synHA and Si–contHA substrates was presumed to occur at loci where charge interactions provided the necessary driving force [252]. In aqueous solutions, however, surface charges have been shielded by hydrating water [253], modulated by pH, and counter balanced by small ions [254]. These will complicate the binding situation of proteins, and then granted them to be more or less susceptible to structural changes [255]. In consistence with the previous study [256], the maximum adsorption on the Si–synHA surface occurred at nearly physiological pH at which the net charge was minimized. The detection of structural rearrangement for proteins adsorbed on the Si–contHA surface was suggested to result in increased contact between the proteins and the surface [257]. Such change was also related to the reversibility of adsorption or desorption of the bound proteins, thereby generating the driving force for adsorption to otherwise prohibitive surfaces by the more compact protein fibrils [258]. In contrast, many non-covalent bonds were likely to form on the Si−synHA surface by highly hydrated and flexible molecules of proteins for which protein spreading would follow [259]. Certainly, the conformational unchanged macromolecules are the prior condition being suggested for material biocompatibility [260]. The influence of nanoscale surface topography on protein adsorption and cellular response has been reported [261]. However, the impact on cell adhesion was not great in the absence of serum, because the number of cells adhered to both rough and planar surfaces were similar [262].

This finding highlighted the important role of adsorbed proteins that had on the modulation of cellular interactions. Moreover, it has been noted that the initially bound proteins may exchange for others with time unless irreversibly adsorbed [263, 264]. Indeed, these dynamic interactions are complex due to the combination of attractive and repulsive forces caused by local changes in surface properties, which may lead to spatial changes in selectivity, quantity and conformation of the adsorbed proteins [265-267]. Thus, surface characteristics are mainly responsible in the interplays between biological systems and artificial interfaces. Consequently, several perspectives such as surface chemistry, charge and morphology must be considered in designing biomaterials to improve the characteristics of adsorbed proteins and modulate biological performance. In accordance, by using our method recently developed, the surfaces of Si–synHA were successfully manipulated for improving the quantity and functionality of adsorbed proteins, compared to that of the Si–contHA counterpart. Due to their superior biocompatible and biological properties, the Si–synHA scaffolds were used for loading of therapeutic molecules and investigated further.

4.4. Part IV: Drug loading and loading efficiency

4.4.1. VCM loading

The effectiveness of antibiotic delivery systems for local treatment of OM is strongly dependent on the drug release profile [268-270]. In this study, the release profile of VCM from the scaffolds of either 0.3Si–contHA, 0.3Si–synHA, 0.4Si–contHA, or 0.4Si–synHA was similar and could be separated into two phases: an initially burst release phase (first 4 hours) followed by a sustained release phase. The drug released rapidly at the initial stage which could suppress the infection. The subsequent delayed phase of the release was to ensure protection from recolonization by residual bacteria. The release behavior of VCM was possibly based on three phenomena: diffusion of the absorbed VCM on the scaffold surface, diffusion via interconnected channels in the scaffolds, and liberation due to the degradation of the scaffolds [271].

The antimicrobial activity and cellular toxicity of the eluents from VCM-loaded scaffolds were performed *in vitro* by up to 24 hours. The eluted VCM concentrations exceeded the MIC for MRSA, but was lower than toxic level (20 mg/L) [272]. The scaffolds were not toxic to osteoblast like cells, ensuring their effectiveness on bone regeneration [50, 52], and had good biocompatibility. In term of the entrapment efficiency (%EE), it was calculated to be more than 90 %. The release of the entrapped drug was approximately 75–80% within 12 days, indicating the sustained release. The release concentration of VCM was more than 20 times the ED_{50} of *S. aureus*, effectively to eliminate the bacterial biofilms. The release mechanism could not be explained by Highuchi model [273, 274], as water uptake by the carrier system was also responsible for the drug delivery. The eluent did not interfere the proliferation of osteoblast-like cells, regarding that this carrier system will be suitable for treatment of bone infections.

4.4.2. rhBMP2 loading

OM is often associated with bone loss. Thus the ability to promote bone formation after curing infection is desirable [275]. Bone morphogenetic protein-2 (BMP2) is one of the most potent inducers of osteogenesis. In this study, the drug-free scaffold was conjugated with heparin using carbodiimide chemistry. The conjugated scaffold (also called heparinized scaffold) was immersed in rhBMP2 solution for the objective of the growth factor loading.

The blood compatibility of the heparinized scaffolds was determined by using PRP assay, which based on clot formation after contact with PRP. The results (Figure 3.17/Table 3.6) showed that the scaffold could prevent blood clot, implying the stability of heparin that being conjugated on the scaffold.

The efficacy on inducing ectopic bone formation for the rhBMP2-loaded scaffold was determined *in vivo*. No inflammatory cells such as macrophages were evident at the implanted sites, indicating biocompatible implants (Figure 3.18) (not shown). In using of heparin at 0.5 and 1.0% w/v, followed by rhBMP2 immobilization at 10μg/mL, the newly formed bone was detected as a shell around the implants or along the implant fractures (Figure 3.18 Gr.4). Interestingly, the inner sections of the 1% heparin and 5-μg/mL rhBMP2 containing implants showed extensive bone formation after 4 weeks (Figure 3.18 Gr.6). Mineralization was thoroughly observed on the implants, indicating that osteogenesis started simultaneously at multiple sites. Although lacking osteogenic cells, the calcium deposition and bone formation could be detected for the scaffolds loaded with a small amount of rhBMP2 (5-μg/mL) (Figure 3.18).

4.5. Part V: Evaluation of VCM/rhBMP2−loaded scaffolds *in vivo*

Simultaneous loading of VCM and rhBMP2 into a single graft composing of Si−nHA particles was carried out. This was followed by the evaluation of its efficiency on creating favorable microenvironments for bone regeneration using rat OM model.

Eighty percents of rats were infected by *S. aureus* BAA 1680 when inoculated at 10^4 CFU. The infection rate was comparable to previous studies using rabbit models [276, 277]. Truely, the great advantage of using rat model is the size of specimens harvested that allows histological survey of the entire affected bone. It also allows numerous investigations of infectious bone and the healing process. All the animals survived 4-weeks post-inoculation and showed mild to moderate signs of infectious severity limited to the tibia. The initial weight loss seemed to be due to anesthesia, surgical trauma, or associated physical stress. Typical radiographic signs of OM were detectable when bone mineral density dropped to at least 35% of that of normal adjacent bone (Figure. 3.19a). This was in agreement with previous studies [278, 279].

The scaffolds of V-group, B-group, or VB-group (Table 2.5) were separately implanted in the infected tibias (n = 4). The improvement in wound healing 8 weeks post-implantation was evaluated. There was a decrease of infection when the antibiotic was included in the scaffolds. This might be due to the higher burst effect that played an active role in eradicating the pathogen in the contaminated wound at early stages, followed by sustained release of the antibiotic at its effective dose to ensure protection of the implanted grafts from colonization by residual bacteria [192, 280]. A small number of neutrophils were found along the scaffold boundaries (Figure 3.20e), suggesting mild foreign body reaction. A higher count of neutrophils was determined for the implants containing rhBMP2 alone, indicating the greater degree of inflammation (Figure 3.20e). There was robust mineralized bone formation adjacent to the implants in VB-group, compared with other groups. This ensures the need for bacterial decontamination before the processes of bone repair can start. Much smaller dose of the antibiotic was required, compared to the cited guidelines [281]. The ample numbers of osteoblasts were

found lining the layers of connective tissue within which the cells proliferated and actively produced osteoid. The conversion of dense connective tissue into mineralized surface was clearly observed by alizarin red S staining (Figure 3.20b, d, e and h). There were osteoclasts in the mineralized layers, suggesting an active remodeling of newly formed bones. In estimation, the concentration of rhBMP2 at the implanted sites was sufficient for stimulating bone regeneration processes. Besides, the inducible effect of rhBMP2 was not suppressed by the presence of VCM because new bones were accelerated to form by using the implants of VB-group (Figure 3.20g and h). Bone healing was mostly completed after 8 weeks of implantation, although a very low dose of rhBMP2 (5 μg) was loaded onto the graft. This dosage level was in a similar range to those being used in other matrix based carriers [282-284]. Thus, the results confirmed the efficacy of the developed delivery system in curing infectious bones.

CHAPTER 5

CONCLUSION

By thoroughly performing the research to serve the expected aims, there are points that can be made conclusions as follow.

1) The nano-sized particles of silicon-substituted hydroxyapatite (called Si–nHA) were successfully produced by using our newly developed chemical reactions. Trace amount of Si (from SiO_4^{4-}) was incorporated *in situ* in the HA lattices at the positions previously occupied by PO_4^{3-} species.

2) The synthesized material was bioactive as large amounts of bone-like apatite were formed after soaking for 14 days in a physiological solution (PBS), and revealed higher water solubility than its parent compound.

3) The highly negative charged surface of the material was appropriate for proteins in any cell culture media to be adsorbed. This phenomenon is prerequisite also for osteoblast attachment, proliferation, differentiation and mineralization, leading to forming new bone.

4) A 3D-structure (also called a scaffold) composing of the material was properly constructed. The construction method was new, simple and reproducible. The scaffold integrity was stabilized by trisodium polyphosphate–chitosan crosslinking and stable by at least 1 month in PBS. The fabricated scaffolds were highly porous with opened and interconnected pores of nano- (<100 nm) and micro- (>100 nm) sized ranges distributing over the structure.

5) The scaffold had high loading efficiency for vancomycin (VCM), which was calculated to be more than 90%. The release of VCM was sustained by not less than 12 days, and approximately 75–80% of the entrapped drug was released. The released concentration was high, sufficient to kill *Staphylococcus aureus* growing as biofilms.

6) The drug release mechanism could not be explained by Highuchi model, as drug diffusion by water up-taking to the carrier system was also responsible for its delivery.

7) The proliferation of osteoblast-like cells was not inhibited by the solution eluted form VCM-loaded scaffold.

8) Heparin was successfully conjugated with chitosan on the scaffold by using carbodiimide reaction, resulting in a heparinized scaffold. The bound heparins uniformly distributed over the scaffold and were sufficiently stable upon storage or by incubation in PBS for at least 1 month.

9) rhBMP2 was immobilized on the conjugated scaffold by ionically interacting with the bound heparin molecule. The rhBMP2-loaded scaffold was biocompatible. Ectopic bone formation could be detected after 4 weeks of subcutaneous implantation in rats, indicating that the protein bioactivity was well preserved upon fabrication and be protected from enzymatic digestion *in vivo*.

10) Rat osteomyelitis model was successfully established by inoculating *S. aureus* BAA 1680 of ~10^4 CFU at epiphysis of the tibial bone. Eighty percent of the animal was found to develop osteomyelitis (OM).

11) Three groups of scaffolds loading with VCM only (called V-group), rhBMP2 only (called B-group), as well as VCM and rhBMP2 (called VB-group) were prepared by applying the described methods as developed individually. These VCM/rhBMP2 (+/— or —/+ or +/+) loaded scaffolds were surgically implanted by replacing the infected bones. After 8 weeks, the decrease of *S. aureus* BAA 1680 in tissues surrounding the implanted site was determined for the samples of V- and VB-groups. In contrast, new bone formation was investigated for the implants of B- and VB-groups. This ensures the need for bacterial eradication before bone repair process can be started up. A higher number of neutrophils were observed for the implants of B-group, suggesting the higher degree of tissue inflammation.

12) The concentrations of rhBMP2 released from the implants were sufficient to induce bone regeneration, and the release was not interfered by the presence of VCM.

13) Osteoblasts were found lining the layers of connective tissue around and in the scaffolds of VB groups, indicating the growth and proliferation of the cells.

14) Osteoclasts could be observed in the new bone tissue. This suggested an active remodeling of the newly formed bone.

All of the results confirmed the efficiency of the presently developed delivery system for treatment of bone diseases that might be useful in clinical practice in the near future.

REFERENCES

1. Martini FH, Nath JL, Bartholomew EF. Fundamentals of anatomy & physiology: Benjamin Cummings; 2011.
2. Meyers MA, Chen PY, Lin AYM, Seki Y. Biological materials: structure and mechanical properties. Prog Mater Sci. 2008;53(1):1-206.
3. Weiner S, Wagner HD. The material bone: structure-mechanical function relations. Annu Rev Mater Sci. 1998;28(1):271-98.
4. McGann A. "The skeletal system." A look inside the human body. 2001; Available from: http://dc263.4shared.com/doc/lbz-olPb/preview.html.
5. García EG. Double experimental procedure for model-specific finite element analysis of the human femur and trabecular bone 2013.
6. Ross M, Pawlina W. Histology: a text and atlas. 6th ed Baltimore; 2011.
7. Meyer U, Meyer T, Wiesmann HP. Bone and cartilage engineering: Springer; 2006.
8. Rho JY, Kuhn-Spearing L, Zioupos P. Mechanical properties and the hierarchical structure of bone. Med Eng Phys. 1998;20(2):92-102.
9. Adams K, Couch L, Cierny G, Calhoun J, Mader JT. *In vitro* and i*n vivo* evaluation of antibiotic diffusion from antibiotic-impregnated polymethylmethacrylate beads. Clin Orthop Relat Res. 1992;278:244-52.
10. Burger EH, Klein-Nulend J. Mechanotransduction in bone—role of the lacuno-canalicular network. FASEB J. 1999;13(9001):S101-S12.
11. Yeni YN, Vashishth D, Fyhrie DP. Estimation of bone matrix apparent stiffness variation caused by osteocyte lacunar size and density. J Biomech Eng. 2001;123(1):10-7.
12. Power J, Loveridge N, Rushton N, Parker M, Reeve J. Osteocyte density in aging subjects is enhanced in bone adjacent to remodeling haversian systems. Bone. 2002;30(6):859-65.
13. Palmer LC, Newcomb CJ, Kaltz SR, Spoerke ED, Stupp SI. Biomimetic systems for hydroxyapatite mineralization inspired by bone and enamel. Chem Rev. 2008;108(11):4754-83.
14. Park JB. Biomaterials science and engineering: Springer; 1984.

15. Gunderson SL, Schiavone RC. International encyclopedia of composites. New York: VCH; 1991.
16. Olszta MJ, Cheng X, Jee SS, Kumar R, Kim YY, Kaufman MJ, et al. Bone structure and formation: a new perspective. Mater Sci Eng R Rep. 2007;58(3):77-116.
17. Shi D. Introduction to biomaterials: World Scientific; 2006.
18. Clarke B. Normal bone anatomy and physiology. Clin J Am Soc Nephrol. 2008;3(Supplement 3):S131-S9.
19. Dorozhkin SV. Nanosized and nanocrystalline calcium orthophosphates. Acta Biomater. 2010;6(3):715-34.
20. Barkaoui A, Hambli R. Finite element 3D modeling of mechanical behavior of mineralized collagen microfibrils. J Appl Biomater Biomech. 2011;9(3):199-205.
21. Multiscale investigation of human bone. 2014; Available from: http://www.ccast.ndsu.edu/news/post/428.
22. Elaine M. Human anatomy & physiology: Benjamin Cummings; 2004.
23. Mescher AL. Junqueira's basic histology: text & atlas: Mcgraw-hill medical New York; 2010.
24. Geiger M, Li RH, Friess W. Collagen sponges for bone regeneration with rhBMP-2. Adv Drug Deliv Rev. 2003;55(12):1613-29.
25. Hollinger JO, Kleinschmidt JC. The critical size defect as an experimental model to test bone repair materials. J Craniofac Surg. 1990;1(1):60-8.
26. Mundell RD, Mooney MP, Siegel MI, Losken A. Osseous guided tissue regeneration using a collagen barrier membrane. J Oral Maxillofac Surg. 1993;51(9):1004-12.
27. Mooney MP, Mundell RD, Stetzer K, Ochs MW, Milch EA, Buckley MJ, et al. The effects of guided tissue regeneration and fixation technique on osseous wound healing in rabbit zygomatic arch osteotomies. J Craniofac Surg. 1996;7(1):46-53.
28. Stetzer K, Cooper G, Gassner R, Kapucu R, Mundell R, Mooney MP. Effects of fixation type and guided tissue regeneration on maxillary osteotomy healing in rabbits. J Oral Maxillofac Surg. 2002;60(4):427-36.
29. Schmitz JP, Hollinger JO. The critical size defect as an experimental model for craniomandibulofacial nonunions. Clin Orthop Relat Res. 1986;205:299-308.

30. Chen FM, Zhang J, Zhang M, An Y, Chen F, Wu ZF. A review on endogenous regenerative technology in periodontal regenerative medicine. Biomaterials. 2010;31(31):7892-927.

31. Drosse I, Volkmer E, Capanna R, Biase PD, Mutschler W, Schieker M. Tissue engineering for bone defect healing: an update on a multi-component approach. Injury. 2008;39:S9-S20.

32. Albrektsson T, Johansson C. Osteoinduction, osteoconduction and osseointegration. Eur Spine J. 2001;10(2):S96-S101.

33. Laurencin CT, Khan Y, Ma PX, Elisseeff J. Polymer/calcium phosphate scaffolds for bone tissue engineering. Taylor and Francis Group: Boca Raton, FL, US; 2006. p. 253-63.

34. Muschler GF, Nakamoto C, Griffith LG. Engineering principles of clinical cell-based tissue engineering. J Bone Joint Surg Am. 2004;86(7):1541-58.

35. Mooney MP, Siegel MI. Animal models for bone tissue engineering of critical-sized defects (CSDs), bone pathologies, and orthopedic disease states. In: Fundamentals of bone tissue engineering 2005. p. 217-44.

36. Mavrogenis AF, Dimitriou R, Parvizi J, Babis GC. Biology of implant osseointegration. J Musculoskelet Neuronal Interact. 2009;9(2):61-71.

37. Lew DP, Waldvogel FA. Osteomyelitis. N Engl J Med. 1997;336(14):999-1007.

38. Lew DP, Waldvogel FA. Osteomyelitis. Lancet. 2004;364(9431):369-79.

39. Concia E, Prandini N, Massari L, Ghisellini F, Consoli V, Menichetti F, et al. Osteomyelitis: clinical update for practical guidelines. Nucl Med Commun. 2006;27(8):645-60.

40. Arduino MJ. 2001; Available from: http://phil.cdc.gov/phil/details.asp.

41. Gordon RJ, Lowy FD. Pathogenesis of methicillin-resistant *Staphylococcus aureus* infection. Clin Infect Dis. 2008;46(Supplement 5):S350-S9.

42. Ouedraogo M, Semdé R, Somé IT, Traore/Ouedraogo R, Guissou IP, Henschel V, et al. Monoolein-water liquid crystalline gels of gentamicin as bioresorbable implants for the local treatment of chronic osteomyelitis: *in vitro* characterization. Drug Dev Ind Pharm. 2008;34(7):753-60.